國立交通大學

電子工程學系 電子研究所碩士班

碩 士 論 文

萃取接觸阻抗係數方法之比較研究——CBKR結構與改良式TLM結構

A Comparison Study of the Specific Contact Resistivity Extraction Methods: CBKR Method and Modified TLM Method

研究生：曾炫滋

指導教授：崔秉鉞 教授

中華民國一 O 一年十二月

萃取接觸阻抗係數方法之比較研究——CBKR結構與改良式TLM結構

A Comparison Study of the Specific Contact Resistivity Extraction Methods: CBKR Method and Modified TLM Method

研究生：曾炫滋　　　　Student : Hsuan-Tzu Tseng

指導教授：崔秉鉞　　　　Advisor : Bing-Yue Tsui

國立交通大學
電子工程學系 電子研究所
碩士論文

A thesis
Submitted to Department of Electronics Engineering & Institute of Electronics
College of Electrical Engineering and Computer Science
National Chiao Tung University
in Partial Fulfillment of the Requirement
for the Degree of Master
in
Electronic Engineering
2012
Hsinchu, Taiwan, Republic of China

中華民國一Ｏ一年十二月

萃取接觸阻抗係數方法之比較研究——CBKR 結構與改良式TLM結構

研究生：曾炫滋　　　　　　　　　　　　　　　　指導教授：崔秉鉞

國立交通大學電子工程系 電子研究所碩士班

摘要

為提升積體電路之性能，金氧半場效電晶體的尺寸不斷微縮，金屬與源極和汲極之接觸面積也隨之縮小，在相同接觸電阻係數下會導致較大的接觸電阻，甚至可能限制藉微縮達成的性能提升。因此，如何降低接觸電阻係數成為首要之務。而低接觸電阻係數的萃取亦是研究接觸電阻的一大課題。目前廣為使用的Cross-Bridge Kelvin Resistor (CBKR)結構其萃取誤差小，但仍會受製程限制造成的寄生效應影響。Transmission line method (TLM)結構的製作方式簡單，但易受製程變異影響也將造成萃取誤差。本論文提出一改良之TLM結構(Modified TLM, mTLM)並與CBKR結構相較，從模擬及實作探討此兩方法的準確度與極限。

過去已有文獻發表接觸電阻係數測量結構的二維模擬結果，近年亦有三維模擬結構提出。文獻中藉由模擬提出接觸電阻係數萃取之數值分析解，藉以修正萃取時測試結構造成的誤差。然分析解採用之模型通常經過簡化，且仍為一相當複雜之關係式。因其需進行大量計算且只適用於特定狀況，對於真實情況下的接觸電阻係數萃取僅能提供參考。因此，本論文使用三維數值模擬元件之電性以進行接觸電阻係數之萃取。對CBKR結構而言，討論可能影響萃取結果之參數，其中包含符合當今製程技術的測試結構尺寸。首先，縮小接觸窗可提升萃取之精確度；其次，製程容忍度(δ)對萃取的相關性變低，此結論不同於二維模擬之結果。另外，本模擬也將元件製作時可能遇到的問題列入考量。光學近接效應(optical

proximity effect)導致接觸窗的邊角圓化(corner rounding)，造成萃取誤差增加。下沉式接觸結構使等效接觸面積增加，並改變電流分布，因而低估接觸電阻係數。至於mTLM結構，利用數值模擬設計結構尺寸後，同樣討論各參數對於萃取結果的影響。因mTLM結構對製程變異甚為敏感，本論文從統計觀點研究其與載子濃度分布變異及元件區側壁傾斜角度變異之相關性。結果發現mTLM結構對載子濃度分布變異有高度相關，而元件區側壁傾斜角度變異之相關性則較輕微。另外，同樣對mTLM考慮下沉式接觸結構，發現在接觸電阻係數較高時，接觸窗下沉會造成接觸電阻係數的高估；而在低接觸電阻係數時則有低估的情形。

第二部分以實驗數據對照模擬結果。為能明確定義出元件區，元件之間採用淺溝渠隔離技術(STI)，在同一製作流程下完成CBKR和mTLM兩種測試結構。CBKR萃取方式簡單，但寄生電阻的影響將導致無法避免之萃取誤差；mTLM萃取過程相對複雜，但透過大量數據平均值趨近期望值之概念，可將其對製程變異的敏感度降低，進而提升萃取的精確度。

本論文從模擬和實驗兩方面討論CBKR和mTLM兩種萃取接觸電阻係數之方法。當CBKR隨著元件微縮而有較小之接觸窗，理論上可得較精確的萃取結果，但寄生項的存在限制了萃取之精確度；而本論文提出之mTLM結構，使用STI技術完成元件製作，利用平均化將其對製程變異敏感度降低之後，對於精確萃取接觸電阻係數應具潛力。但若考慮下沉式接觸結構，其造成的影響複雜，對CBKR和mTLM兩種結構都將產生無法預測之誤差。因此，透過本研究可看出接觸電阻係數之萃取無論CBKR或mTLM兩種方法都遭遇困難，新穎結構與萃取方法仍為迫切需求。

A Comparison Study of the Specific Contact Resistivity Extraction Methods: CBKR Method and Modified TLM Method

Student: Hsuan-Tzu Tseng Advisor: Bing-Yue Tsui

Department of Electronics Engineering

Institute of Electronics

National Chiao Tung University

Abstract

To enhance the performance of Integrated circuits (IC), the MOSFETs have been scaled down continuously, and contact areas between metal and source/drain have shrunk consequently. Then, with a fixed specific contact resistivity (ρ_c), the contact resistance increases and would suppress the performance improvement caused by scaling. Therefore, how to reduce the ρ_c is the first task, and how to extract such a low ρ_c is also challenging. The Cross-Bridge Kelvin Resistor (CBKR) is a common used test structure, which has a lower extracted error according to two-dimensional (2-D) analysis while the error still exists due to the parasitic effect caused by process limitation. The transmission line method (TLM) is easy to be fabricated but sensitive to the process variation. In this thesis, a modified TLM (mTLM) procedure is proposed and compared with the CBKR method by both simulation and experiment.

2-D simulations on the CBKR method have been widely studied, and three-dimensional (3-D) simulations have also been reported in recent years. Some

analytic solutions were proposed to correct the extracted error. Nevertheless, as analytic methods are used, the models are usually developed after some simplifications, though still in a complex form. Thus, for a real case, analytic methods can only provide a rough estimation, since they have to perform complex calculation but only are suitable for particular conditions. In this thesis, 3-D simulation of device characteristics is performed to evaluate the accuracy of the ρ_c extraction by the CBKR and mTLM methods.

For the CBKR method, several parameters are considered. The dimensions of the test structures are close to the design rule of the current IC technology. First, reducing the contact area will enhance the extraction accuracy. Second, the process tolerance (δ) has less influence on the extraction, which is different from the fact presented in 2-D simulation. Moreover, issues occurring in fabrication are also taken into account. The corner-rounding contact resulting from the optical proximity effect increases the extraction error. The recessed contact structure underestimates the ρ_c because of the increase of the effective contact area and the change of the current distribution. As for the mTLM method, the dimensions of the mTLM structure are designed and optimized by simulation at first. Because the mTLM structure is sensitive to the process variation, this thesis studies the dependence on the variation of the dopant concentration and the variation of tapered sidewall angles of the active region according to the statistic. It is observed that there is a strong dependence on the variation of the dopant concentration, while a relative slight dependence on the variation of tapered sidewall angles of the active region. In addition, as the recessed contact is considered, the ρ_c is overestimated with higher ρ_c but underestimated with lower ρ_c.

The second part shows the experimental data compared with the simulation. In order to define the active region explicitly, shallow trench isolation (STI) is utilized.

The CBKR and the mTLM structures are realized in an identical process flow. The CBKR method is easier to extract the ρ_c, but the parasitic resistance is about to result in inevitable extracted error. The mTLM method is complicated; however, its sensitivity to the process variation could reduce and the extracted accuracy could be enhanced, by means of averaging sufficient data according to the fact that the average of sufficient data is closed to the expected value which is the true ρ_c.

This thesis discusses the CBKR and mTLM methods to extract the ρ_c by simulation and experiment. The CBKR structure with a smaller contact area due to the devices scale down would obtain more accurate results in theory, while the parasitic resistance would still limit the accuracy. On the other hand, the mTLM structure proposed in this thesis is realized by using the STI process. Its sensitivity to the process variation could be diminished by averaging data. Therefore, the TLM method could be more accurate and is promising for ρ_c extraction. However, if the recessed contact structure is considered, due to its complex influence on the ρ_c extraction, an incalculable error would be caused for the CBKR and mTLM methods. Therefore, according to this thesis, it would be observed that the ρ_c extraction encounters great challenge for both CBKR and mTLM methods. Novel test structure and extraction procedure are still critical issue.

致謝

研究所的日子，無論學業、研究或者生活都學到許多，在此向曾幫助過我的人們獻上由衷感謝。

首先最感謝的是指導教授 崔秉鉞老師，在老師悉心指導下，無論實驗分析數據及呈現，或是做學問的態度，都讓我獲益良多。而在待人處事上，老師正直而不失圓融的性格更讓我習得許多寶貴的經驗。

實驗方面感謝交大奈米中心與國家奈米元件實驗室提供製程機台與實驗環境。特別感謝 NDL 的林家毅先生提供 STI 相關製程的協助，以及彭馨誼小姐在磷酸濕蝕刻的幫忙。

感謝實驗室的大家，尤其感謝振銘學長在實驗與生活上的幫忙及關心。感謝培宇學長在模擬的協助與建議，感謝嶸健學長與元宏學長幫忙 TEM 試片製作，也感謝定業學長實驗與修課時的幫助，以及璽允學長在實驗室帳務交接時的幫忙。謝謝子瑜在我研究上給我的支持，謝謝高銘鴻、茂元在實驗及量測上的幫忙，也謝謝克勤、孫銘鴻的相互勉勵。謝謝哲儒平時的熱心，謝謝崇德常常提供新點子，也謝謝雪君、翰奇、泰源和國丞帶給實驗室熱絡的氣氛。

感謝我的朋友們，研究之餘陪我聊天、給我加油打氣，最後感謝我的父母與弟弟給我的支持，謝謝你們。

Contents

Abstract (Chinese) i

Abstract (English) iii

Acknowldegdments vi

List of Figures ix

Chapter 1 Introduction 1

1-1 Overview 1

1-2 Properties of Metal/Semiconductor Contacts 3

1-2-1 The Schottky Model of Metal/Semiconductor Contacts 3

1-2-2 Conduction Mechanisms for Metal/Semiconductor Contacts 4

1-3 Specific Contact Resistivity (ρ_c) 5

1-4 Measurement of Contact Resistance and Specific Contact Resistivity 7

1-4-1 The Transmission Line Model (TLM) 7

1-4-2 The Cross-Bridge Kelvin Resistor (CBKR) 10

1-5 Motivation 11

1-6 Thesis Organization 13

Chapter 2 Simulation Configurations, Results and Discussion 22

2-1 Overview 22

2-2 Device Structures and the Measurement Description of the CBKR Method 22

2-3 Device Structures and the Extraction Procedure of the Modified Transmission-Line Model (mTLM) Method 23

2-3-1 Device Structures of the mTLM Method 23

2-3-2 Extraction Procedure of the mTLM Method 24

2-4 Setting of Contact Resistivity (ρ_c) 25

2-5 Simulation Results 25
2-5-1 Three-Dimensional Simulation of the CBKR Structure 27
2-5-2 Issues of the CBKR Structure 29
2-5-2-1 Considering the Circular Contact..29
2-5-2-2 Considering the Recessed Contact...30
2-5-3 Three-Dimensional Simulation of the Self-Aligned mTLM Structure 31
2-5-4 Issues of the mTLM Structure..33
2-5-4-1 Considering the Variation of Doping Concentration in Semiconductors 33
2-5-4-2 Considering the Variation of Tapered Sidewall Angle of the Diffusion Region 34
2-5-4-3 Considering the Recessed Contact...36
Chapter 3 Experiments and Discussion..54
3-1 Overview...54
3-2 Experimental Settings of the CBKR Method and the mTLM Method........54
3-3 Process Flow 55
3-4 Results and Discussion 59
3-4-1 CBKR Method...59
3-4-2 mTLM Method...60
3-4-3 Comparison and Discussion 63
Chapter 4 Summary and Future Work...78
4-1 Summary..78
4-2 Future Work 81
References..83
Author's Biography 90

List of Figures

Chapter 1

Fig. 1-1 Components of the resistance associated with the source/drain junctions of a MOS transistor [4]. 14

Fig. 1-2 Relative contribution from each component of the resistance to series resistance for different technology nodes [6]. 14

Fig. 1-3 Electron energy band diagrams of the metal/semiconductor contact according to the Schottky model, (a) before contact (b) after contact. 15

Fig. 1-4 Electron energy band diagram of n-type semiconductor with surface states. This diagram shows the Fermi-level pinning 15

Fig. 1-5 Conduction mechanisms for metal/semiconductor contacts, (a) thermionic emission (b) thermionic-field emission (c) field emission. 16

Fig. 1-6 Image force barrier lowering (IFBL). The peak of the barrier lowers down as the IFBL is considered [16]. 16

Fig. 1-7 The concept of 1-D transmission line model (TLM). 17

Fig. 1-8 Different measured positions of the voltages for the front resistance (R_f) and the end resistance (R_e), respectively. 17

Fig. 1-9 The transmission line tap resistor (TLTR). 18

Fig. 1-10 Extraction of the front resistance (R_f) from the R_{total}-L_d plot. 18

Fig. 1-11 The contact end resistance (CER). 19

Fig. 1-12 The cross-bridge Kelvin resistor (CBKR). 19

Fig. 1-13 The ρ_{ce} as a function of the ρ_c using the self-aligned CBKR structure in 3-D simulation. As the 3-D effect is considered, i.e., $\rho_b \cdot t \neq 0$, even though a self-aligned CBKR structure is utilized, the parasitic resistance cannot be

ignored. The ρ_b is the resistivity of the semiconductor active layer, and t is the thickness of the semiconductor active layer [26]. 20
Fig. 1-14 TEM image of the cross section of the bird's beak due to the lateral diffusion of LOCOS [29]. 20
Fig. 1-15 TEM image of the cross section of tapered sidewall of STI [30]. 21

Chapter 2

Fig. 2-1 The general 3-D simulated structures of the CBKR method. 39
Fig. 2-2 Definition of parameters for CBKR method (a) with a square contact, and (b) with a circular contact. The metal layer is not drawn here. 39
Fig. 2-3 The general 3-D simulated structure and definition of parameters of the mTLM method. 40
Fig. 2-4 Design guideline of the L_c of the mTLM extraction procedure. The $\coth(L_c/L_T)$ approaches 1 as $L_c >> L_T$. 40
Fig. 2-5 Simulated current distribution of the CBKR structure as $\delta = 0$ using the CBKR structure. 41
Fig. 2-6 (a) Relative error versus the actual ρ_c with various A_c values as $\delta = 0$ using the CBKR structure. (b) Parasitic resistance versus the contact size with various ρ_c values as $\delta = 0$ using the CBKR structure. 41
Fig. 2-7 (a) Relative error versus the actual ρ_c with various δ values as $A_c = 50\times50$ nm^2 using the CBKR structure. (b) Parasitic resistance versus the actual ρ_c with various δ values using the CBKR structure. 42
Fig. 2-8 (a) Comparison of the relative error between the square contacts and the circular contacts using the CBKR structure. The cases that $\delta = 0$ and $\delta = 50$ nm are both exhibited. (b) Comparison of the parasitic resistance between the square contacts and the circular contacts using the CBKR structure. The

cases that $\delta = 0$ and $\delta = 50$ nm are both exhibited. 43

Fig. 2-9 Cross-section diagram of total S/D resistance with the recessed silicide taken in account. The contact resistance includes two parallel components: the resistance underneath the silicide and the resistance at the side of the recessed contact [67]. 44

Fig. 2-10 Relative error versus the recession depth with various ρ_c as $A_c = 50 \times 50$ nm^2 using the CBKR structure. 45

Fig. 2-11 Relative error versus the recession depth with various ρ_c as $A_c = 1 \times 1$ μm^2 using the CBKR structure. 45

Fig. 2-12 Extraction procedure of the ρ_c using the mTLM structure with $W_c = 1$ μm and $L_c = 2$ μm as $\rho_c = 1 \times 10^{-7}$ Ω-cm^2. (a) The R_f is obtained from the y-intercept of the R_{total}-L_d plot. (b) The ρ_c is extracted from the slope of the R_f-$1/W_c$ plot. 46

Fig. 2-13 Relative error versus the actual ρ_c with different L_c using the mTLM procedure...47

Fig. 2-14 (a) Comparison of the relative error between the CBKR and mTLM methods. Fig. 2-14(b) Comparison of the accuracy between the CBKR and mTLM methods. 47

Fig. 2-15 Distribution of the R_{total} values for each diffusion length (L_d) as the variation of doping concentration in semiconductors is considered. For each L_d, 100 test structures are used with the doping concentrations of top surface set 1×10^{20} cm^{-3} $\pm$ 5% in Gaussian distribution. 48

Fig. 2-16 (a) R_f extrapolated from the intercept of R_{total}-L_d plot involving 100 extraction results. The R_f varies in a wide range, and $R_f < 0$ may even occur. Fig. 2-16(b) Distribution of the R_s involving 100 extraction results from the slope of the R_{total}-L_d plot as the variation of doping concentration is

considered. (c) Distribution of the Rf involving 100 extraction results from the y-intercept of the R_{total}-L_d plot as the variation of doping concentration is considered. For certain cases, $R_f < 0$ occurs, which is impossible to happen in reality. 49

Fig. 2-16(d) Distribution of the ρ_{ce} involving 100 extraction results from the mTLM method as the variation of doping concentration is considered. The inset shows the data in the range from 0 to 2×10^{-8} Ω-cm^2 in detail. 50

Fig. 2-17 Distribution of the R_{total} values for each diffusion length (L_d) as the variation of tapered sidewall angles of the diffusion region is considered. For each L_d, 100 test structures are used with sidewall angles set 88 ± 2° in Gaussian distribution. 51

Fig. 2-18 (a) Distribution of the R_s involving 100 extraction results from the slope of the R_{total}-L_d plot as the variation of tapered sidewall angles is considered. (b) Distribution of the R_f involving 100 extraction results from the slope of the R_{total}-L_d plot as the variation of tapered sidewall angles is considered. (c) Distribution of the ρce involving 100 extraction results from the mTLM method as the variation of tapered sidewall angles is considered. 51

Fig. 2-19 (a) Relative error versus the recession depth with different ρ_c values using the mTLM structures. (b) The difference between the ρce and ρ_c versus the recession depth with different ρ_c values using the mTLM structures. The inset shows the results as ρ_c from 1×10^{-6} to 1×10^{-9} Ω-cm^2 in detail............53

Chapter 3

Fig. 3-1(a) Schematic layout of test structures. (b) Schematic cross-section of test structures. Left: the mTLM method. Right: the CBKR method. 65

Fig. 3-2 Process flow of test structures. (a) Pad oxide growth and nitride deposition.

(b) Trench etching. (c) PECVD TEOS oxide deposition for trench filling. (d) CMP process. (e) Post-field oxidation process to finish STI. (f) BF_2^+ implantation and dopant activation. (g) Passivation oxide deposition and contact hole patterning. (h) NiSi silicidation. (i) Al pad patterning and Al sintering..66

Fig. 3-3 (a) SEM image of the edge between STI and active region after CMP process. (b) OM image of the top view of the active region and dummy patterns after CMP process. The magnification is 1000x. (c) OM image of the top view of the mTLM structure after silicidation process. The magnification is 1000x. (d) OM image of the top view of the final mTLM structure. The magnification is 250x. (e) OM image of the top view of the final CBKR structure. The magnification is 250x. 69

Fig. 3-4 (a) The ρ_{ce} versus the A_c using the CBKR method with δ = 50 nm. The lowest extractable ρ_{ce} value is marked for each test structure with different A_c. (b) The ρce versus the A_c using the CBKR method with δ = 0.1 μm. The lowest extractable ρ_{ce} value is marked for each test structure with different A_c. (c) The ρ_{ce} versus the A_c using the CBKR method with δ = 0.3 μm. The lowest extractable ρ_{ce} value is marked for each test structure with different A_c. 72

Fig. 3-5 Illustration of two different forced current directions used in the CBKR extraction...73

Fig. 3-6 Illustration of the R_f extrapolation from different groups of devices using the mTLM method with W_c = 1 μm and L_c = 2 μm...74

Fig. 3-7(a) R_f extrapolation after averaging R_{total} values for each L_d using the mTLM method with W_c = 1 μm and L_c = 2 μm. R_f extrapolation after averaging R_{total} values for each L_d using the mTLM method with W_c = 1.5 μm and L_c

= 2 μm. (b) R_f extrapolation after averaging R_{total} values for each L_d using the mTLM method with W_c = 1.5 μm and L_c = 2 μm. R_f extrapolation after averaging R_{total} values for each L_d using the mTLM method with W_c = 1.5 μm and L_c = 2 μm. (c) R_f extrapolation after averaging Rtotal values for each L_d using the mTLM method with W_c = 2 μm and L_c = 2 μm. 74

Fig. 3-8 (a) The $\rho_{ce} = 2.9\times10^{-7}$ Ω-cm^2 is extracted using the mTLM method with L_c = 2 μm. The $\rho_{ce} = 9.8\times10^{-7}$ Ω-cm^2 is extracted using the mTLM method with L_c = 1 μm....................76

Fig. 3-8(b) The $\rho_{ce} = 9.8\times10^{-7}$ Ω-cm^2 is extracted using the mTLM method with L_c = 1 μm. 76

Fig. 3-9 TEM images of NiSi/Si contact. Some unexpected voids between the NiSi layer were observed, and thus the actual A_c should be smaller than the designed size. 77

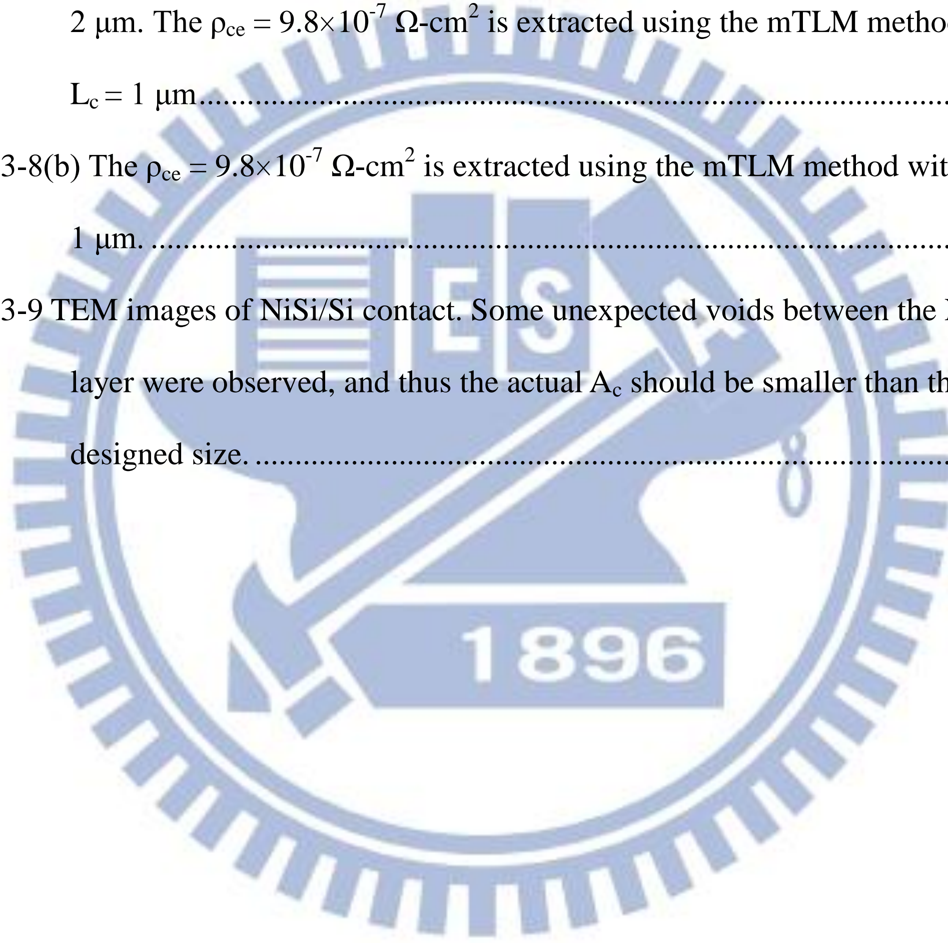

Chapter 1
Introduction

1-1 Overview

Due to the requirement of higher device performance, scaling down is necessary to obtain larger driving current of transistors. However, there are some issues associated with continued CMOS scaling, such as gate dielectric leakage, parasitic capacitance, and parasitic series resistance [1-5]. The use of alternative high-κ gate dielectric materials would reduce gate leakage [6], and the reduction of the source/drain extension junction depth could decrease capacitive coupling of the drain to the channel. As for the parasitic series resistance, it is still a challenge and needed to be improved. As illustrated in Fig.1-1, the parasitic series resistance has been modeled by dividing into four components: source/drain extension (SDE) to gate overlap resistance R_{ov}; SDE resistance R_{ext}; deep S/D resistance R_{dp}; and silicide-diffusion contact resistance R_c [7]. Among these components, the R_c varies as a reciprocal to the scaling factor [8], and indeed it is predicted to dominate the total parasitic resistance of the device for future technology scaling, as shown in Fig.1-2 [9-12]. Therefore, the R_c should be emphasized on and will be investigated in subsequent contents.

In order to characterize the contact resistance, contacts should be considered first. The metal/semiconductor contact is mainly concerned because it is most common. It was discovered by Braun in 1874, and the first acceptable theory was developed by Schottky in the 1930s, which is frequently referred as Schottky model [13]. According to the basis of semiconductor device physics, conduction mechanisms for

metal/semiconductor contacts will be discussed briefly in section 1-2.

Considering the influence of the contact resistance to advanced devices, for multiple-gate transistors (MuGFET), it has been shown that the contact resistance between the S/D silicide and Si-fin dominates the S/D parasitic series resistance behavior of the narrow fin devices [14]. SiGe S/D, NiPt germanosilicide, and NiAl-alloy have been proposed to alleviate the concerns of the S/D parasitic series resistance in p-channel transistors [15-17]. For ultra-thin-body (UTB) SOI MOSFETs, the thin Si layer is the major cause of the increase of the parasitic series resistance. Thus the contact resistance plays a minor role in the parasitic series resistance and could be reduced by the silicidation of the source/drain to compensate for the increased parasitic resistance [4,18,19]. To reach a low parasitic S/D contact resistance, the Schottky-barrier (SB) MOSFET devices would be attractive. By replacing the S/D impurity doping with metal-like silicides typically, the SB MOSFET provides an elegant solution to reach a low parasitic S/D contact resistance, although for the SB CMOS circuits there are requirements that a silicide for NMOS having a low barrier to electrons on N-type silicon and another silicide for PMOS having a low barrier to holes on P-type silicon [20].

Owing to the significance of the contact resistance to devices, an appropriate parameter should be introduced to describe the contact characteristics. Then, the specific contact resistivity (ρ_c), which is independent of contact size (A_c), is introduced. Ideally the current drive in a MOSFET is limited by the channel resistance, while in practice all components of the parasitic series resistance illustrated in Fig.1-1 have great influence and would suppress the device performance. The requirement that the summation of these other resistances should be less than 10% of the channel resistance for normal design procedures determines the demand of the ρ_c, which should be decrease to 1×10^{-8} Ω-cm^2, according to the International Technology

Roadmap of Semiconductor (ITRS) [21].

For such a low value, how to accurately extract ρ_c should be carefully considered. Typical measurement methods are described in section 1-4. Because the extracted specific contact resistivity (ρ_{ce}) becomes erroneous, a new extraction procedure using modified transmission line model (mTLM) is developed and compared with the common used cross-bridge Kelvin resistor (CBKR) method in this thesis. Finally, the outline of this thesis is given.

1-2 Properties of Metal/Semiconductor Contacts

1-2-1 The Schottky Model of Metal/Semiconductor Contacts

The energy band diagrams of a metal/semiconductor contact according to the Schottky model is shown in Fig.1-3. When a metal contacts with a semiconductor, intimate contact between the two materials are assumed. There are some parameters to be introduced. The metal work function (Φ_M) is the energy difference between the Fermi level and the vacuum level of the metal; the semiconductor work function (Φ_S) is defined similarly; the relationship between a work function and its correlated potential is $\phi_M = \frac{\Phi_M}{q}$; the electron affinity (χ_s) is the potential difference between the bottom of the conduction band and the vacuum level at the semiconductor surface.

For the case that an n-type semiconductor meets a metal with higher work function, electrons pass from the semiconductor into the metal. The resulting potential difference is the built-in potential (V_{bi}), which is the difference between Φ_M and Φ_S. The barrier height (ϕ_B) after contact is given by $\phi_B = \phi_M - \chi$. V_{bi} and ϕ_B are shown in Fig.1-3.

According to the equation above-mentioned, barrier height (ϕ_B) is strongly dependent on the metal work function (Φ_M). In practice, however, only in

predominantly ionic semiconductors the strong dependence can be observed. Bardeen first explained the insensitivity of barrier height to the metal work function in covalently bonded semiconductors. It is indicated that the localized surface states determine the barrier height. Dangling bonds increase localized energy states at the surface of the semiconductor with energy levels lying in the energy gap. These surface states distribute continuously in the band gap and are characterized by a neutral level (ϕ_0), as shown in Fig.1-4. The surface states modify the charge in the depletion region and thus influence the barrier height. If there is a higher density of surface states at the semiconductor surface, charge exchange happens mostly between the metal and the surface states, rather than between the metal and the semiconductor. As a result, the barrier height in Fig.1-4 becomes independent of the metal work function, which is called the Fermi-level pinning [22].

1-2-2 Conduction Mechanisms for Metal/Semiconductor Contacts

The conduction mechanisms for a metal/semiconductor contact are illustrated in Fig.1-5(a), (b), and (c) [13,23]. Thermionic emission dominates when the barrier width is so wide that electrons can only jump over the barrier by thermal excitation. This occurs for lightly-doped semiconductors. The current density dominated by thermionic emission is given by

$$J = A^{*}T^{2}exp\left(\frac{-q\phi_B}{kT}\right)\left(exp\left(\frac{qV}{kT}\right)-1\right),$$

(Eq. 1-1)

where A* is the Richardson's constant, k is the Boltzmann constant, and T is the absolute temperature.

Field emission means carrier tunneling directly because the barrier is sufficiently narrow. This mechanism takes place when the semiconductor is high-doped. The

tunneling current can be described by

$$J \propto exp\left(\frac{-q\phi_B}{E_{00}}\right),$$

(Eq. 1-2)

where E_{00} is the characteristic energy, which is defined by

$$E_{00} = \frac{q\hbar}{2}\sqrt{\frac{N}{m^{*}\varepsilon_s}},$$

where ħ is the Plank constant, N is the dopant concentration, m* is the tunneling effective mass, and ε_s is the permittivity of a semiconductor. The image force barrier lowering (IFBL) is also an effect depending on the doping concentration. When an electron in the semiconductor is at a distance x from the metal, there exists an electric field perpendicular to the metal surface. A hypothetical positive image charge q located at a distance (-x) inside the metal is assumed and therefore the electron has a negative potential energy

$$IFBL(x) = -\frac{q^2}{16\pi\epsilon_d x},$$

where ϵ_d represents the permittivity of the semiconductor. This potential energy should be considered to obtain the total energy of the electron. Fig.1-6 shows that the peak of the barrier is reduced consequently, and it is dependent on the electric field at the contact. The larger the electric field at the contact, the larger the barrier lowering by image force.

Thermionic-field emission basically combines thermionic emission with field emission, and it dominates the current density when the semiconductor is in the medium doped concentration.

1-3 Specific Contact Resistivity (ρ_c)

As a result of the Schottky barrier, there is a resistance existing when carriers

pass through the interface. The contact resistance is characterized by two quantities: the contact resistance, R_c (Ω), and the specific contact resistivity, ρ_c (Ω-cm^2). The definition of the ρ_c is the reciprocal of the derivative of current density to the voltage at zero bias, as shown in the following expression:

$$\rho_c = \left(\frac{\partial J}{\partial V}\right)_{V=0}^{-1}$$

(Eq. 1-3)

The ρ_c is not a measurable parameter but can be calculated from the corresponding R_c as

$$\rho_c = R_c A$$

(Eq. 1-4)

, where A (cm^2) is the effective contact area. The ρ_c is a useful parameter to evaluate ohmic contacts because of its independence of contact area. Therefore, the ρ_c can be utilized simply to compare qualities of contacts with different contact sizes.

For semiconductors with lower doping concentrations, the current density of a metal-semiconductor contact is dominated by thermionic emission, given as in Eq. 1-1. Therefore, the corresponding ρ_c is derived as

$$\rho_c(TE) = \frac{k}{qA^*T} exp\left(\frac{q\phi_B}{kT}\right)$$

(Eq. 1-5)

On the other hand, for semiconductor with higher doping concentrations, tunneling process dominates the current density. The tunneling current is given as Eq. 1-2. Consequently,

$$\rho_c(FE) \propto exp\left(\frac{q\phi_B}{E_{00}}\right) = exp\left[\frac{2\sqrt{\varepsilon_s m^*}}{\hbar}\left(\frac{\phi_B}{\sqrt{N_d}}\right)\right]$$

(Eq.1-6)

Briefly, according these above equations, the ρ_c(TE) is sensitive to temperature for a

given barrier height, while the ρ_c(FE) is sensitive to the doping density under the contact [13].

1-4 Measurement of Contact Resistance and Specific Contact Resistivity

In order to obtain the ρ_c correctly, accurate model of contact resistance is essential. In general, 3-dimensional (3-D) model is comprehensible. The contact system can be described sufficiently by the Poisson and the two carrier continuity equations. However, it is difficult for computation and generalization in the 3-D analysis. Then, some simplifications and boundary conditions are made and 2-D model, or even 1-D model, was achieved [24].

For the last thirty years, several test structures for ρ_c extraction have been proposed. The two-terminal contact resistance method is the earliest and simplest method. However, it only provides the information of contact process quality but neither contact resistance nor the ρ_c value [13]. The transmission line model (TLM) is a common method to extract contact parameters and then determine the ρ_c. Based on the TLM, the front resistance (R_f) and the end resistance (R_e) can be obtained depending on measuring the voltage from different positions of the contact [25-27]. The cross-bridge Kelvin resistor (CBKR) is the most widely employed method because it can measure the ρ_c directly [25,28,29]. The vertical CBKR test structure was proposed to minimize the lateral current crowding which is the difficulty that the typical CBKR encountered [30].

In the following subsections, the concepts of the TLM and the CBKR method are presented in detail.

1-4-1 The Transmission Line Model (TLM)

The transmission line model (TLM) of the metal/semiconductor contact is introduced by Shockley and further refined by Berger [31]. The 1-D TLM is illustrated in Fig.1-7. The semiconductor is assumed with a distributed sheet resistance (R_s) and no thickness. On the other hand, the metal is assumed with a negligible sheet resistance. By solving the Poisson and the continuity equation simplified in the 1-D model, current density is obtained from the TLM as follows:

$$I(x) = I_1 exp(-x/l_t),$$

(Eq. 1-7)

where $l_t = \sqrt{\rho_c/R_s}$ is the characteristic length at which 63% of the current has transferred into the metal, and I_1 is the initial current injecting at the leading edge of the contact. It is noted that this model is valid when the contact length (L_c) is long, i.e., $L_c \gg l_t$.

The operation of test structures based on the TLM approach is that a current I is injected into the contact from the diffusion to the metal, and the voltage between the two layers is measured by two other terminals. Different measured positions of the voltage are for the front resistance (R_f) and the end resistance (R_e), respectively, as shown in Fig.1-8.

The transmission line tap resistor (TLTR), as illustrated in Fig.1-9, is a convenient structure to measure the front resistance (R_f). In Fig.1-8, the R_f is defined as the ratio of the voltage drop (V_f) across the interfacial layer at the front edge of the contact to the total current through the contact [24,25]. At the front edge, the current density is the highest. The total resistance (R_{total}) between the two metal terminals consists of the diffusion resistance between the two contacts and the R_f of both contacts:

$$R_{total} = R_s \times \frac{L_d}{W_d} + 2R_f,$$

(Eq. 1-8)

where R_s, L_d, and W_d are the sheet resistance, the length, and the width of the diffusion region, respectively. By means of varying L_d, the R_f can be obtained, as shown in Fig.1-10. In the 1-D model, the R_f is solved in the following form:

$$R_f = \frac{V_f}{I} = \frac{\sqrt{R_s \rho_c}}{W_c} coth(L_c/L_T)$$

(Eq. 1-9)

$$\text{and } L_T = \sqrt{\frac{\rho_c}{R_s}},$$

(Eq. 1-10)

where L_c is the contact length, W_c is the contact width, and L_T is the transfer length. Hence the ρ_c can be extracted from the R_f.

The end resistance (R_e) is defined as the ratio of the voltage drop (V_f) across the interfacial layer at the rear edge of the contact to the total current through the contact [24,25]. At the rare edge, the current density is the lowest. Similar to the R_f,

$$R_e = \frac{V_e}{I} = \frac{\sqrt{R_s \rho_c}}{W_c} \operatorname{csch}(L_c/L_T).$$

(Eq. 1-11)

The contact end resistance method (CER) is illustrated in Fig.1-11.

The great advantage of the TLM structure is its simplicity to be fabricated [32-34]. The 1-D analysis is based on the assumption that contact width and diffusion width are equal, i.e., W_c=W_d [35]. However, the condition is not in practice, and the lateral current flows in the diffusion region around the contact, which results in errors when extracting the ρ_c employing the typical TLM [29,36]. Circular TLM(CTLM) can avoid the extracted inaccuracy stemming from the lateral current [13,37,38]. Besides, the 2-D analysis has been studied [24,35,39]. If the thickness of the diffusion region is considered, the 3-D model is necessary.

Furthermore, the extraction of the TLM method tends to be affected by the

fabrication process, i.e., the ρ_{ce} not only varies with the contact size but also depends on the R_s of the doped semiconductor layer [39]. Analytical model has been developed for the experimental uncertainty from the fundamental TLM expressions [34,40,41].

1-4-2 The Cross-Bridge Kelvin Resistor (CBKR)

The cross-bridge Kelvin resistor (CBKR) is a widely used method to extract the ρ_c because it measures the ρ_c directly and simply [13,25,34,42]. Fig.1-12 shows a general four-terminal CBKR structure with definitions of its geometry parameters. A current (I) is forced into one diffusion arm, through the contact, and then flows out the test structure from a metal arm. The voltage drop (V_k) of the interfacial region between diffusion and metal is measured as V_2-V_1 by using other two voltage sensing arms [25,28,31]. Then, the measured Kelvin resistance (R_k) is the ratio of the voltage drop across the contact (V_k) to the current flowing through the contact, i.e.,

$$R_k = \frac{V_k}{I}.$$

(Eq. 1-12)

Then the ρ_c is extracted from the measured Kelvin resistance,

$$\rho_{ce} = R_k A.$$

(Eq. 1-13)

As the ρ_c is large, it is valid according to the 1-D analysis [43] that the R_c equals the R_k but current injecting into the overlap region (δ) between the contact edge and the diffusion edge is not explained explicitly. For the ρ_c becomes smaller, the 1-D model cannot describe the data correctly [24,43-45]. Therefore, the 2-D analysis is needed for extracting the ρ_c more accurately. Corrections for the extraction error have been studied extensively by numerical simulations [24,44-46] and analytical modeling [36,43,47]. In the 2-D model [43], R_{geom}, involving the current flow around the

contact in the overlap region, is introduced into one of the components of measured R_k,

$$R_k = R_c + R_{geom},$$

(Eq. 1-14)

where $R_{geom} = \frac{4R_s\delta^2}{3W_xW_y}\left[1 + \frac{\delta}{2(W_x-\delta)}\right]$ and R_s is the sheet resistance of the underlying layer. Thus, R_k is dependent of R_s in the 2-D analysis and will affect the extraction of the ρ_c. As the thickness of the semiconductor layer (*l*) is considered, 3-D analysis is required [48,49]. In the 3-D analysis [49], the voltage drop at the metal-semiconductor interface is compared to that at the semiconductor, and the ratio will influence the determination of the ρ_c.

Universal error correction curves were provided in a number of previous works, in order to correct the systematic error in the CBKR [50]. Universal curves have been given by 2-D [24,51-53] and 3-D model [49]. In addition, random measurement error on the ρ_c extraction has been considered [50], and evaluation of the A_c has been also studied [54,55].

1-5 Motivation

Although there have been reports that successfully obtained the ρ_{ce} even in the range of 10^{-10} Ω-cm^2 of metal to metal or metal to silicide contact [56,57], the low ρ_c extraction between silicide and silicon below 10^{-8} Ω-cm^2 regime is still considered to be difficult [29,44,49,50]. To investigate completely, a 3-D simulation of the CBKR structure is necessary to be performed, and the parameters should be reconsidered as well, including the case that the A_c reduces to achieve the design considerations of nowadays as the ρ_c approaches to 10^{-8} Ω-cm^2.

Due to the accuracy limitation of the typical CBKR structure [29,44,49], some

other test structures, such as the modified CBKR structure [58], the Scott TLM structure [33,60], and the end resistance method [59], have been studied. However, since the Scott TLM structure would suffer from an inaccurate estimation of current distribution [61] while the end resistance would be too low to be measured [24], the ρ_c extraction should be still carefully considered. In this thesis, a modified extraction procedure using the transmission line model (mTLM) is proposed and studied by 3-D simulation.

It is expected that the extraction results of the fabricated test structures are consistent with those of the simulation. However, some parameters will affect the ρ_c extraction during the fabrication, but they may not be easily analyzed in practice. It could be possible to infer their influences by the 3-D simulation results.

First, the sidewall tapered angles of the active region is needed to be discussed. As mentioned in section 1-4-1, W_d is larger than W_c in the TLM structure, which results in additional error [35]. To achieve the self-aligned TLM structure, a novel process flow is proposed using the shallow trench isolation (STI), instead of the local oxidation of silicon (LOCOS) since the LOCOS incurs the lateral diffusion, as shown in Fig.1-14 [62], and cannot define the W_c exactly. As the STI structure is utilized, the problem of lateral diffusion could be alleviated. Nevertheless, as shown in Fig.1-15, the sidewall would be not vertical entirely in practice [63], and thus could influence the ρ_c extraction.

Second, the doping concentration variation should be considered. In reality, some variations could occur in a fabrication process. Due to the sheet resistance is one of the essential parameters in the mTLM method [29], the variation of dopant concentration would degrade the accuracy of the ρ_c extraction.

Recession of the silicide is another problem of the ρ_c extraction. The silicon is consumed during the silicide formation, and the recessed silicide/silicon contact is

formed [42,57,64,65]. The sidewall of the recessed contact could be an additional current path [61,66,67], and hence the influence of the recessed contact of the CBKR and mTLM methods is needed to be studied.

Briefly, this thesis will focus on the comparison between the CBKR and mTLM methods, considering those above-mentioned problems.

1-6 Thesis Organization

The first chapter is the introduction consisting of properties of metal/semiconductor contacts, definition of the ρ_c, and common ρ_c extraction methods. Besides, the mTLM method is also proposed. The second chapter presents the simulation configurations, results and discussion. Parameters are taken into considerations for the ρ_c extraction of both CBKR and mTLM methods, and the influences of the issues during the fabrication process are also discussed. The process flow, experimental results and discussion are shown in the third chapter. Both the CBKR and mTLM structures are fabricated in an identical process flow, and their ρ_c extractions are exhibited and compared with each other. During the extraction procedure there are some phenomena worthy to be discussed. The cross-section of the contact is also inspected by transmission electron microscopy (TEM) images. The last chapter is the summary and future works of this thesis.

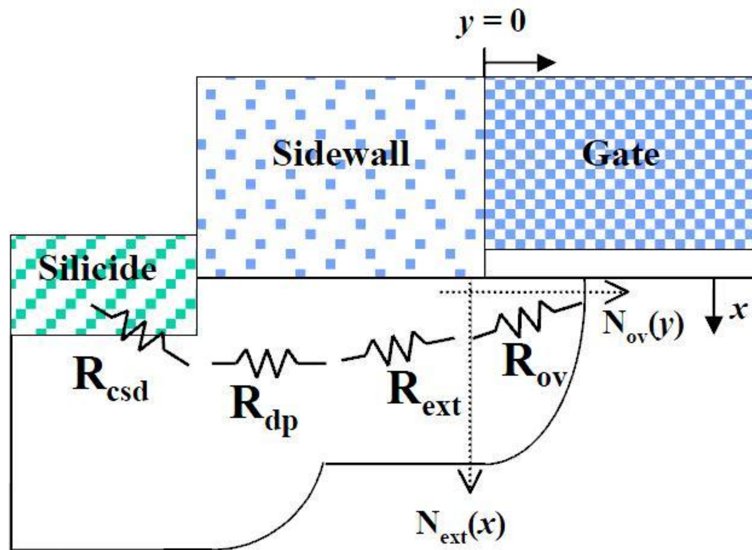

Fig. 1-1 Components of the resistance associated with the source/drain junctions of a MOS transistor [4].

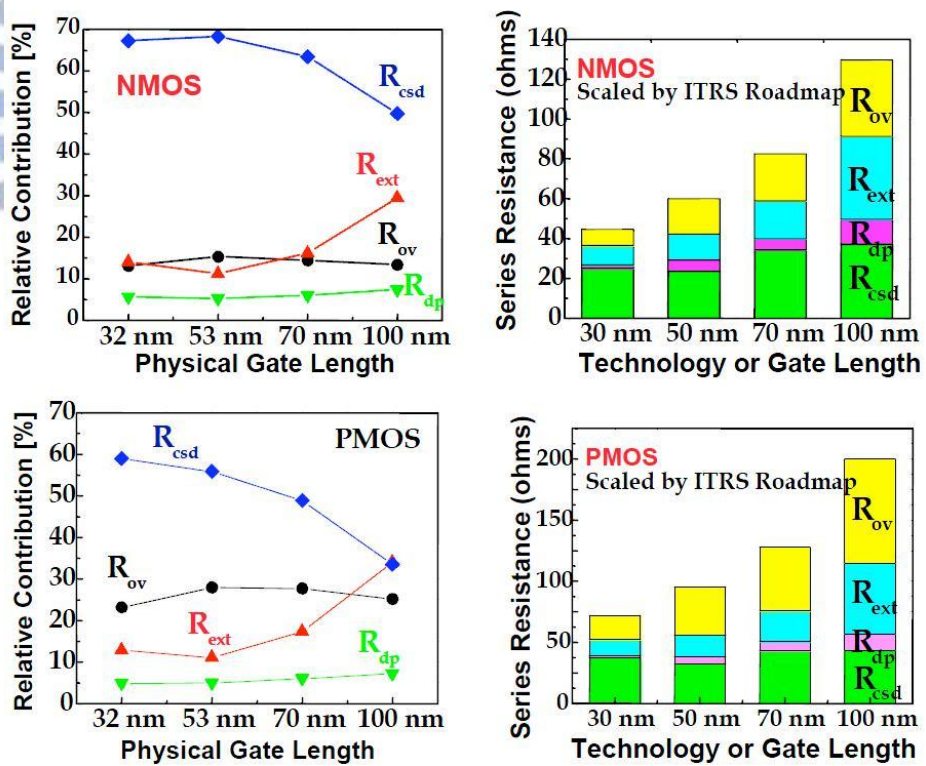

Fig. 1-2 Relative contribution from each component of the resistance to series resistance for different technology nodes [6].

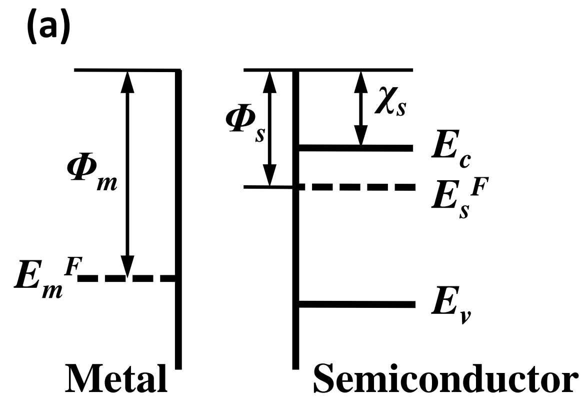

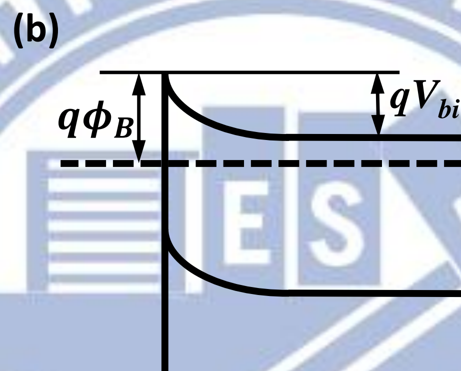

Fig. 1-3 Electron energy band diagrams of the metal/semiconductor contact according to the Schottky model, (a) before contact (b) after contact.

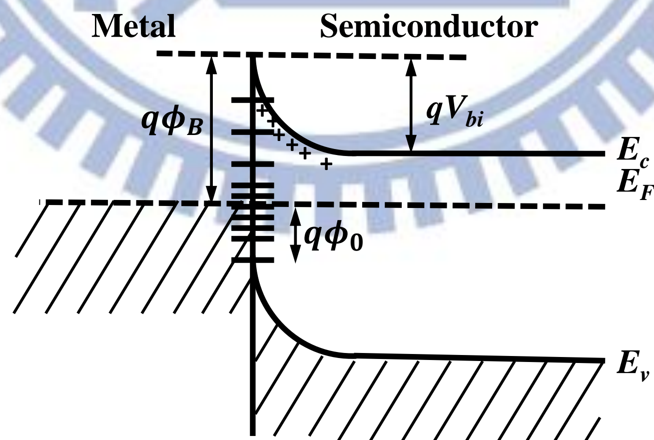

Fig. 1-4 Electron energy band diagram of n-type semiconductor with surface states. This diagram shows the Fermi-level pinning .

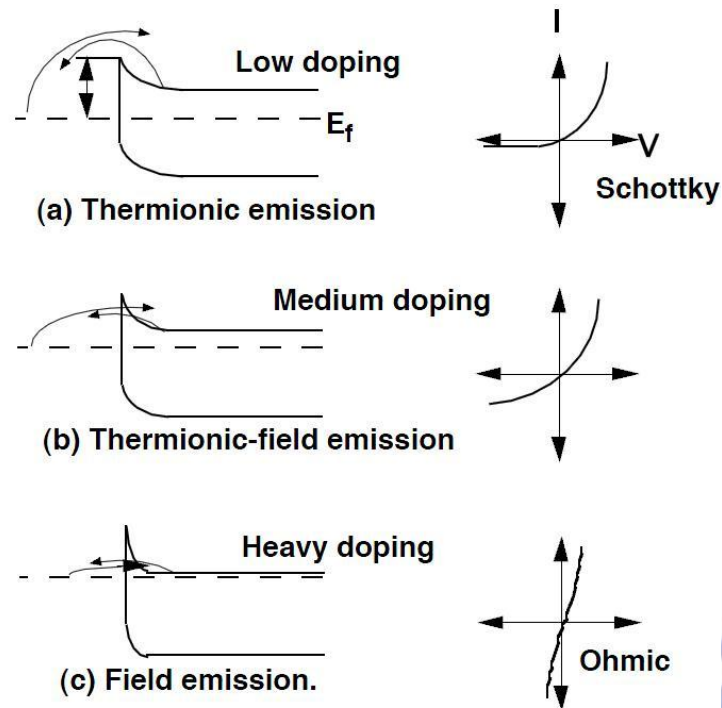

Fig. 1-5 Conduction mechanisms for metal/semiconductor contacts, (a) thermionic emission (b) thermionic-field emission (c) field emission.

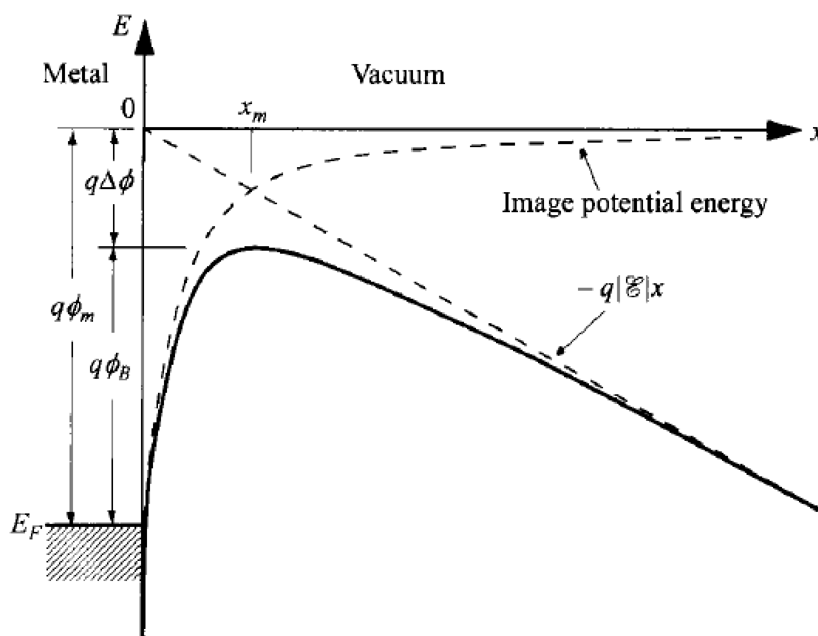

Fig. 1-6 Image force barrier lowering (IFBL). The peak of the barrier lowers down as the IFBL is considered [16].

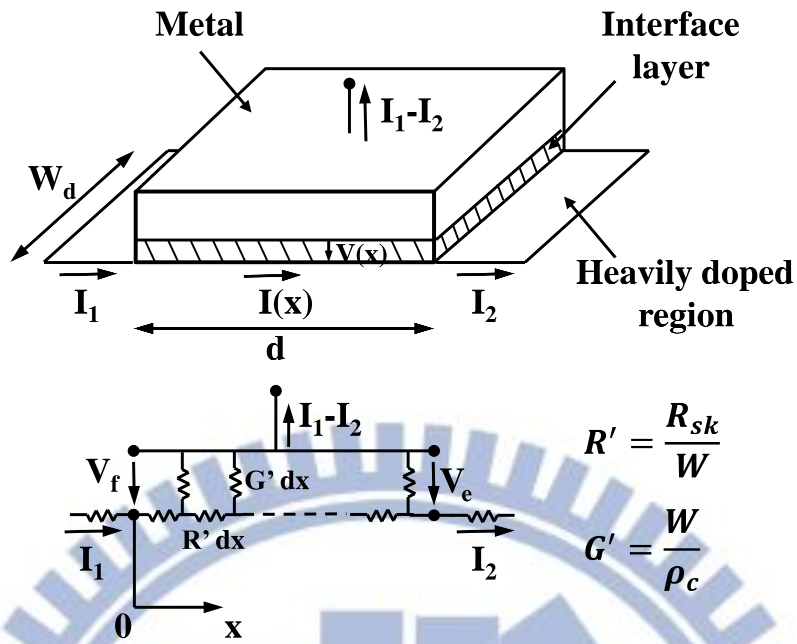

Fig. 1-7 The concept of 1-D transmission line model (TLM).

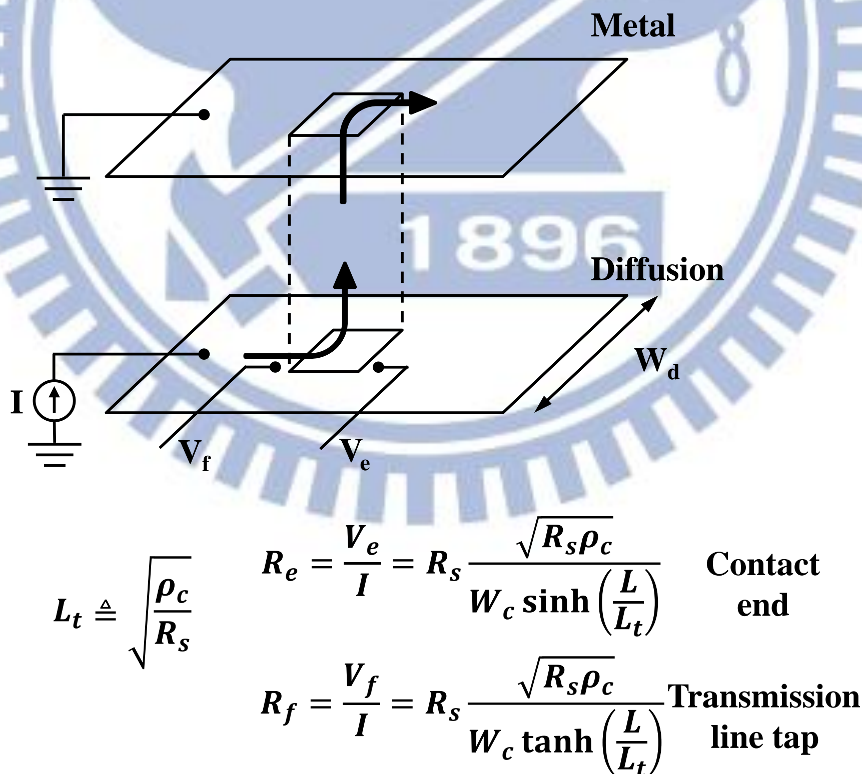

$$L_t \triangleq \sqrt{\frac{\rho_c}{R_s}}$$

$$R_e = \frac{V_e}{I} = R_s \frac{\sqrt{R_s \rho_c}}{W_c \sinh\left(\frac{L}{L_t}\right)} \quad \text{Contact end}$$

$$R_f = \frac{V_f}{I} = R_s \frac{\sqrt{R_s \rho_c}}{W_c \tanh\left(\frac{L}{L_t}\right)} \quad \text{Transmission line tap}$$

Fig. 1-8 Different measured positions of the voltages for the front resistance (R_f) and the end resistance (R_e), respectively.

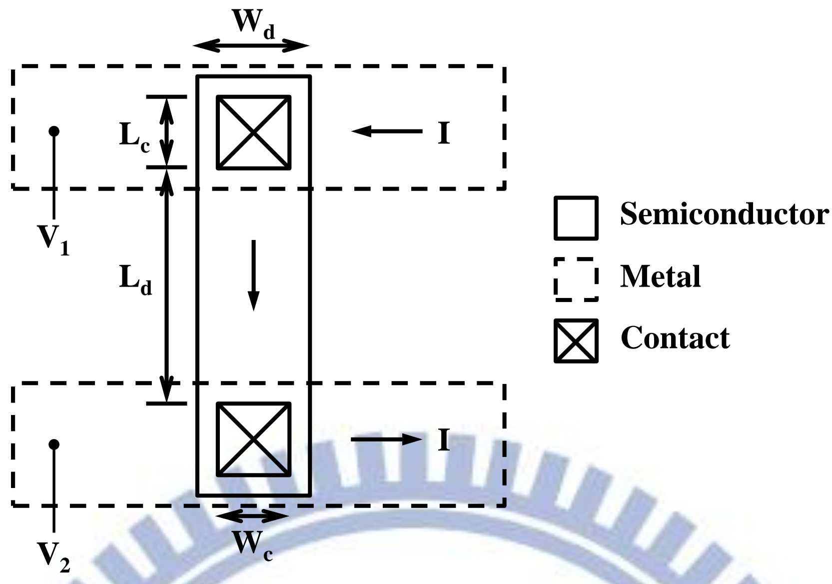

Fig. 1-9 The transmission line tap resistor (TLTR).

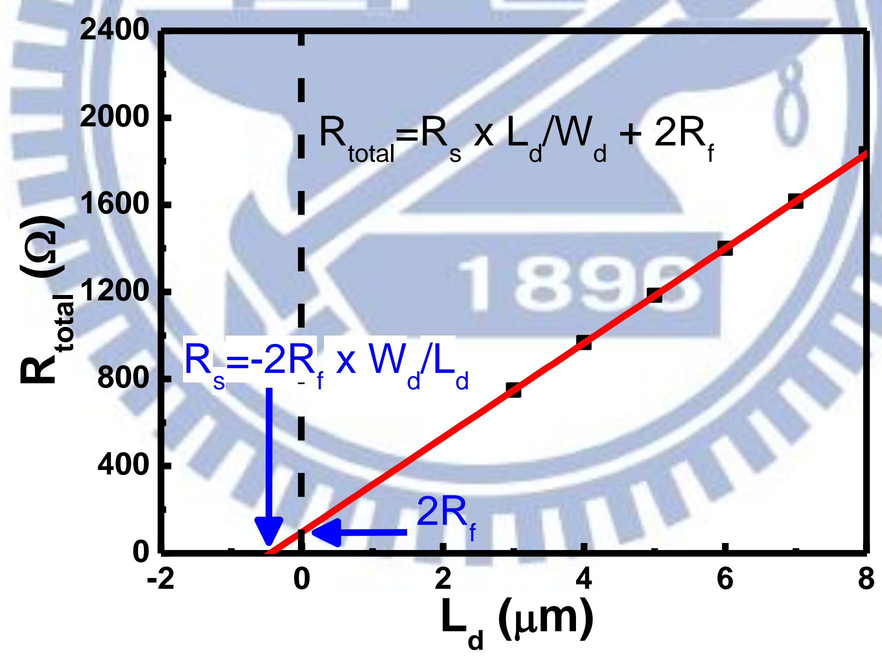

Fig. 1-10 Extraction of the front resistance (R_f) from the R_{total}-L_d plot.

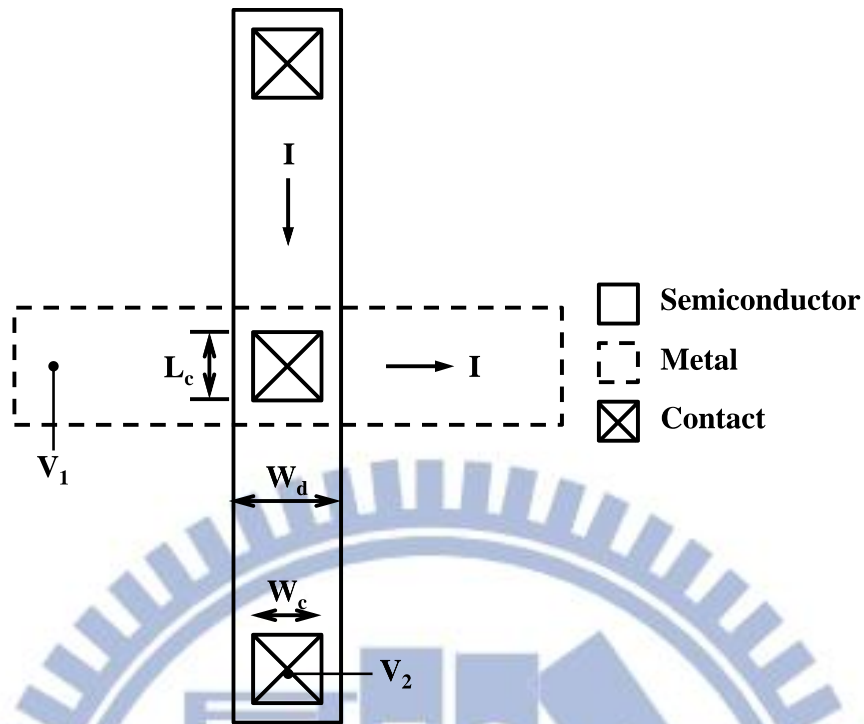

Fig. 1-11 The contact end resistance (CER).

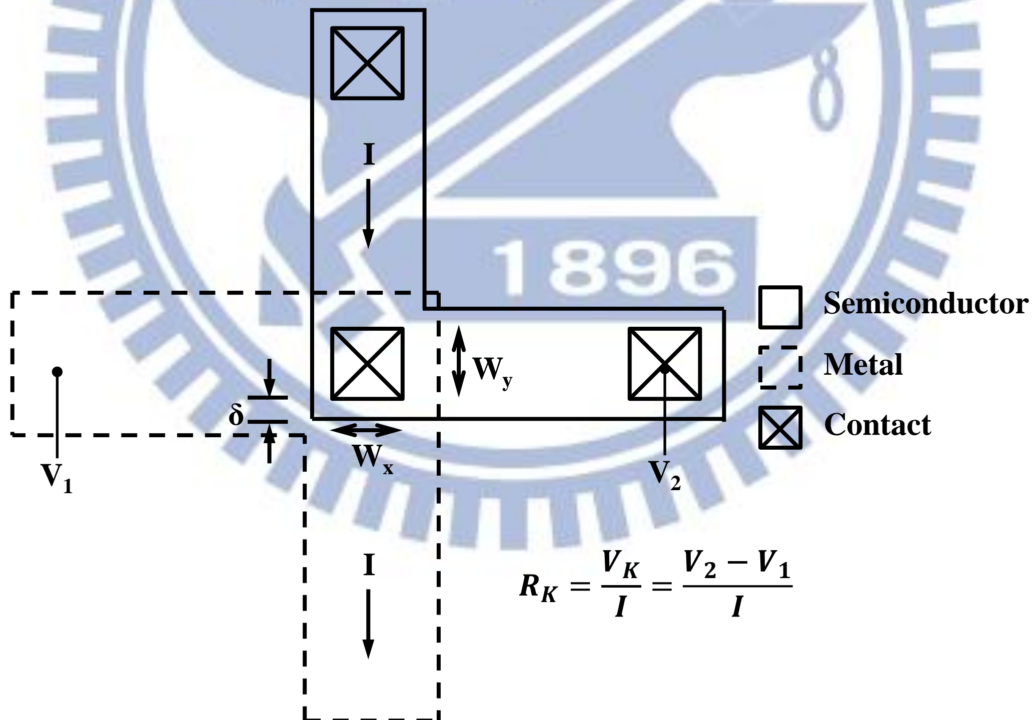

Fig. 1-12 The cross-bridge Kelvin resistor (CBKR).

1896

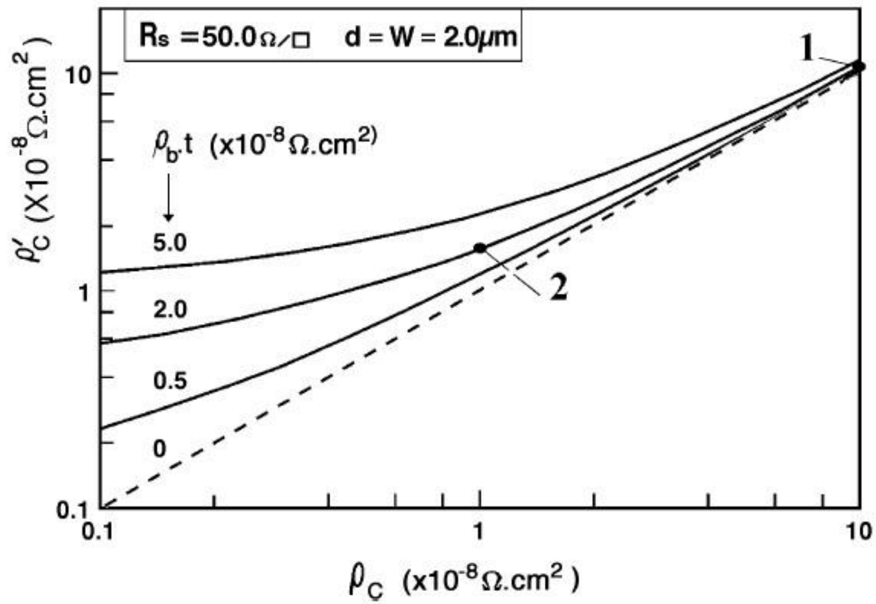

Fig. 1-13 The ρ_{ce} as a function of the ρ_c using the self-aligned CBKR structure in 3-D simulation. As the 3-D effect is considered, i.e., $\rho_b \cdot t \neq 0$, even though a self-aligned CBKR structure is utilized, the parasitic resistance cannot be ignored. The ρ_b is the resistivity of the semiconductor active layer, and t is the thickness of the semiconductor active layer [26].

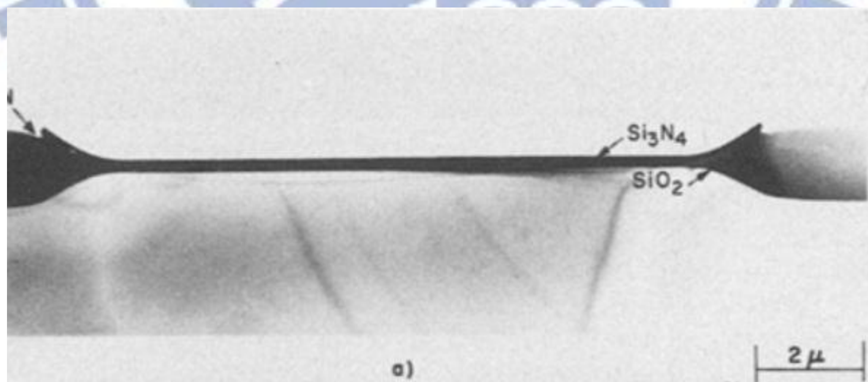

Fig. 1-14 TEM image of the cross section of the bird's beak due to the lateral diffusion of LOCOS [29].

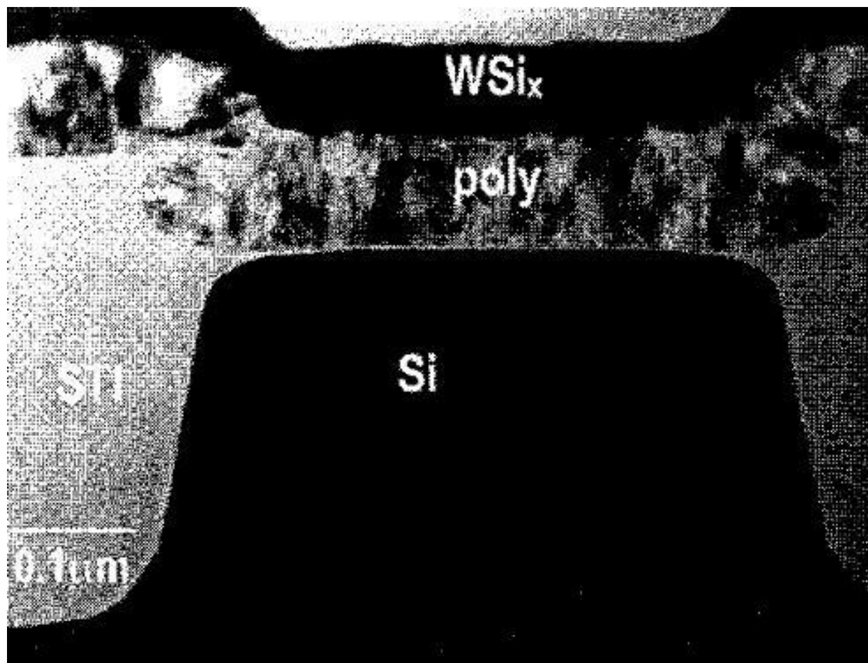

Fig. 1-15 TEM image of the cross section of tapered sidewall of STI [30].

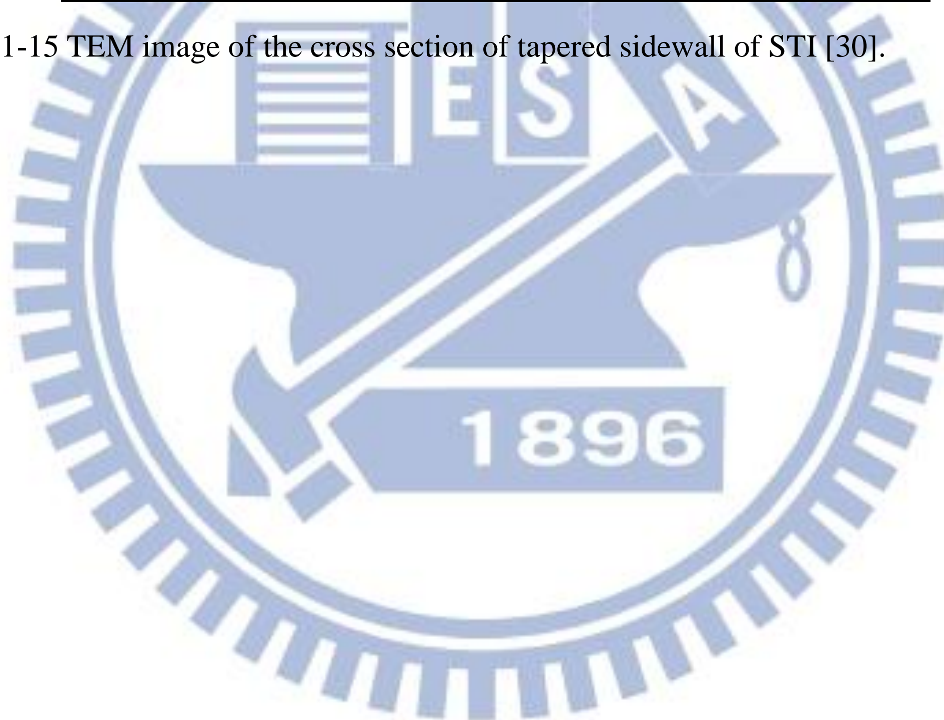

Chapter 2
Simulation Configurations, Results and Discussion

2-1 Overview

In this chapter, the device structure and the ρ_c extraction in simulation of the CBKR method are introduced at first in section 2-2, and next those of the mTLM method are mentioned in section 2-3. Then, in section 2-4, the simulation settings of the ρ_c extraction for this work is presented. Finally, the simulation results for both the CBKR and the mTLM method are shown and compared in section 2-5, which consists of the ideal and real conditions respectively.

2-2 Device Structures and the Measurement Description of the CBKR Method

Fig.2-1 illustrates the generalized structure of the CBKR method for simulation by using a Sentaurus simulator in this work. In Fig.2-2(a), the contact width (W_c) and the contact length (L_c) are the same for the square contact and the contact size (A_c) is defined as $W_c \times L_c$. For circular contact, the A_c is defined as $\pi \times (d/2)^2$, where d is the diameter of a circular contact as shown in Fig.2-2(b). The lengths of the current carrying arm and the voltage sensing arm are more than two times of the W_c to guarantee uniform current distribution as well as the accuracy of voltage sensing [29]. The process tolerances (δ) are assumed equal in x and y directions; besides, there is no misalignment considered in this work. The diffusion junction depth (x_j) is set as

100 nm. The diffusion region is arsenic doped with Gaussian doping profile and the corresponding sheet resistance R_s is 217.82 Ω/□. The metal thickness is set as 100 nm, and the sheet resistance is 0.245 Ω/□. The depth of contact interface (m_j) is defined as the depth of silicon consumption during silicidation and is measured from the Si surface.

The CBKR structures in this work include a wide range of contact sizes (A_c) for the square contact: 1×1 μm^2, 0.5×0.5 μm^2, 0.1×0.1 μm^2, 50×50 nm^2, 40×40 nm^2, 30×30 nm^2, 20×20 nm^2, and 10×10 nm^2. As the circular contact is considered, the A_c is determined by the diameter of the contact (d), and the d values are chosen to be the same as the W_c of square contacts. In addition, the process tolerances (δ) are considered with 0 nm, 10 nm, 20 nm, 30 nm, 40 nm, and 50 nm. When the recessed contact is considered, moreover, the depths of contact interface (m_j) are 10 nm, 20 nm, 30 nm, 40 nm, and 50 nm.

The measurement of the CBKR method has been explained in section 1-4-2, and Eq.1-12 and Eq.1-13 show the details of extraction procedure.

2-3 Device Structures and the Extraction Procedure of the Modified Transmission-Line Model (mTLM) Method

2-3-1 Device Structures of the mTLM Method

Fig.2-3 illustrates the generalized structure of the mTLM method for simulation by using a Sentaurus simulator in this work. The mTLM method is on the basis of the transmission-line model (TLM) [31]. It should be noted that the diffusion width (W_d) is in general larger than the contact width (W_c). However, in this thesis, that the W_d equals the W_c would be achieved by a novel process flow with shallow trench isolation (STI). Consequently, the process tolerances are not necessary to be

considered in the mTLM method. The contact length (L_c) is a critical factor in the mTLM method for simplification and will be explained in detail in section 2-3-2. Besides, the R_s and the thicknesses of the diffusion region and the metal arms are set to be the same as those of the CBKR method.

2-3-2 Extraction Procedure of the mTLM Method

In Fig.2-3, the total resistance (R_{total}) between any two contacts consists of the diffusion resistance between the two contacts and the front resistance (R_f) of both contacts, as mentioned in section 1-4-1:

$$R_{total} = R_s \times \frac{L_d}{W_d} + 2R_f,$$

(Eq. 1-8)

where R_s is the sheet resistance of the diffusion region. The R_f can be extracted from the y-intercept and the R_s can be extracted from the x-intercept of the R_{total}-L_d plot, as presented in Fig.1-8. The correlation between the R_f and the ρ_c has been derived as

$$R_f = \frac{V_f}{I} = \frac{\sqrt{R_s \rho_c}}{W_c} coth(L_c/L_T)$$

(Eq. 1-9)

and $L_T = \sqrt{\frac{\rho_c}{R_s}}$,

(Eq. 1-10)

where L_T is the transfer length.

As $L_c >> L_T$, the hyperbolic-cotangent term approaches 1 and then the R_f can be simplified to:

$$R_f = \frac{V_f}{I} = \frac{\sqrt{R_s \rho_c}}{W_c}$$

(Eq. 2-1)

The slope of the R_f-$1/W_c$ plot gives the ρ_c as the R_s is known. Fig.2-4 draws the

$\coth(L_c/L_T)$ as a function of L_c with ρ_c as parameter and the R_s is 200 Ω/□. It is observed that as ρ_c is lower than 1×10^{-7} Ω-cm^2, the error becomes less than 0.1% if L_c is longer than 1 μm. That is, the ρ_c can be extracted easily and accurately using micro-process instead of nano-process. In this chapter, three L_c and W_c values of 1 μm, 1.5 μm and 2 μm are considered. In addition, several L_d values are used to obtain the R_{total}-L_d plot.

2-4 Setting of Contact Resistivity (ρ_c)

In this simulation, the actual contact resistivity (ρ_c) is set by means of inserting an extreme thin layer between the diffusion layer and the metal layer. Using the following relationship between the ρ_c and the resistivity (ρ) of this inserting layer:

$$\frac{\rho_c}{A} = \rho \times \frac{L}{A} \ ,$$

(Eq. 2-2)

where A is the contact area and L is the thickness of the inserting layer. The actual ρ_c values can be simply decided by setting appropriate resistivity values of the inserting layer as its thickness is chosen, for example 1 nm in this simulation.

For the recessed contacts, there are additional interfaces between the metal and the diffusion layer necessary to be taken into account. Side interfaces are added for both the CBKR method and the mTLM method. Similarly, extreme thin layers are inserted to set the ρ_c at the side interfaces as well as at the recessed interface.

2-5 Simulation Results

In this section, the simulation results of the CBKR method are discussed in section 2-5-1 and 2-5-2. At first, the 3-D effect is considered for the self-aligned CBKR structure. When the 3-D CBKR test structures are used, different contact sizes

(A_c) would affect the extraction accuracy. Next, the process tolerance (δ) is included to describe the extraction of the CBKR method more completely. Thus, in section 2-5-1, the A_c and the δ dependence are shown. On the other hand, however, in reality the CBKR method may suffer from some issues during the fabrication process. The contact shape would be closer to a circle due to the optical proximity effect especially when the contact size becomes smaller. Also, during the silicide formation, the recessed contact would be formed, causing the change of the extraction results and the current distribution as well. Section 2-5-2 will concentrate on these two situations, attempting to comprehend the extraction using the CBKR method in reality by analysis of simulation results.

The second part of this section discusses the mTLM method by simulation in section 2-5-3 and 2-5-4. In section 2-5-3, the simulation results of the optimum mTLM structures are shown at first, and then compared with the self-aligned CBKR method to figure out the intrinsic extraction error for each method. Then, it should be necessary to include some problems happening in reality too. Unlike the direct ρ_c extraction of the CBKR method, the mTLM method would be more sensitive to the variation of fabrication process because of the needs of several test structures with different L_d for its extraction procedure. The R_s is determined by the distribution of the doping concentration in the diffusion region. In addition, the current distribution would be affected by the sidewall angles of the STI structure as the STI process is utilized. In section 2-5-4, these two issues are analyzed by the statistic, observing the consequence if the mTLM method is used in reality. At last, the recession of the contact would be also a difficulty in the ρ_c extraction by the mTLM method and will be investigated in detail.

2-5-1 Three-Dimensional Simulation of the CBKR Structure

Traditional two-dimensional (2-D) model predicts that the extracted error depends on the process tolerance between contact hole and the diffusion region (δ), and the error becomes zero on self-aligned structure, i.e. $\delta = 0$ [29]. However, when a 3-D structure is considered, the parasitic resistance cannot be ignored even though a self-aligned CBKR structure is utilized. Fig.2-5 shows the simulated current distribution of the CBKR structure as $\delta = 0$. The thickness of the diffusion layer provides additional current path; hence the current crowding happens at both the underneath and the outside of the contact region and results in the parasitic resistance. This phenomenon is also shown in the literature [49]. In Fig.2-6(a), the relative error as a function of the actual ρ_c with various A_c is shown by simulating self-aligned CBKR structures. It seems that the smaller A_c could help the ρ_c extraction more accurate. To explain explicitly, the A_c dependence of the parasitic resistance should be discussed first, illustrated in Fig.2-6(b). It is observed that the parasitic component (R_p) increases as the contact size reduces, which is independent of the ρ_c value. Similar to the 2-D model, the measured resistance (R_k) also suffers from the R_p, which involves the current flow around the contact or under the contact since the depth of the diffusion region is taken into account for 3-D analysis. Hence, the R_p depends on the properties of the diffusion layer like the sheet resistance or the depth. To concentrate on the R_p, as the current flows through the diffusion layer, if the contact size is smaller, then the cross-sectional area where the current encountering would be smaller as well, and hence the parasitic resistance increases. Then, according to Eq.1-14, the ρ_c can be deduced from the following equation:

$$\rho_{ce} = R_k \times A_c = \rho_c + R_p \times A_c$$

(Eq. 2-3)

Since the amount of the R_p increasing is less than that of the A_c decreasing, the

parasitic term in Eq.2-3 diminishes with the decrease of the A_c, and therefore the ρ_c can be extracted more accurately as the A_c reduces.

Fig.2-7(a) shows the δ dependence of the CBKR method in the ρ_c extraction as the A_c reduces to 50×50 nm^2. Similarly, the parasitic resistances are illustrated in Fig.2-7(b) to realize the influence of the δ. In previous 2-D simulation results, the δ is regarded as a critical error source for the CBKR method [29]. The fact that the extraction error becomes higher as the δ increases is also mentioned in the literature. On the contrary, the influence of the δ is more complicated in the 3-D simulation. When the test structure is no longer self-aligned, i.e., $\delta \neq 0$, the R_p decreases at first, and then increases with the δ. The decrease of the R_p could be explained by the restriction against current crowding outside the contact at the voltage arm, due to the additional corner formed by the δ between the voltage arm and current arm of the diffusion region. Then, with the increase of the δ, more additional current paths are provided near the contact, which weakens the restriction from the corner formed by the δ and hence raises the R_p. In addition, it is noticed that for the structures with $\delta = 0$ and $\delta \neq 0$, $\delta = 10$ nm for example, the R_p difference between these structures is less for higher ρ_c than that for lower ρ_c. It should be mentioned first that the current could flow into the contact easier as ρ_c decreases, which reduces the current crowding effect near the contact region. This could be observed as the ρ_c is below 10^{-7} Ω-cm^2 in this simulation, and therefore the R_p diminished gradually. Then the δ dependence is considered. The δ restricts the current crowding outside the contact; however, it has a weak influence on the cases with a lower ρ_c, since the current tends to flow into the contact already, and consequently the decrease of the R_p is less. It should be noticed that although the R_p values are different for each ρ_c in Fig.2-7(b), there is a lightly effect on the ρ_{ce} due to the product with relative small A_c value based on Eq.2-3. Thus, in Fig.2-7(a), a less dependence on ρ_c extraction could be characterized.

2-5-2 Issues of the CBKR Structure

2-5-2-1 Considering the Circular Contact

Ideally the printed features should conform to the design patterns, i.e., for the general CBKR structures, contacts would be square-shaped. Nevertheless, due to the optical proximity effect, feature distortion occurs in the pattern transfer process, and problems like pitch effect, line-end shortening, and corner rounding are commonly observed [2]. Among the above-mentioned effects, corner rounding would change the actual contact sizes of the CBKR structures, and make an obvious difference to the extraction accuracy. In this subsection, the CBKR structures with the circular contacts, which can be seen as the worst case affected by corner rounding, are discussed.

The CBKR structures with the circular contacts have been studied in the literature [57], though only the 2-D model was considered. In this work, 3-D simulation is performed for the circular contacts with d=50 nm and the square contact with A_c=50×50 nm^2. The comparison of the relative error between square contacts and circular contacts using the CBKR structures with both $\delta = 0$ and $\delta = 50$ nm is shown in Fig.2-8(a), and the R_p values are shown in Fig.2-8(b). First of all, in the two figures, curves can be divided into two groups by different contact shapes, indicating that the contact shape plays a major role on the parasitic resistance instead of the δ. It seems that both of the circular contact and the δ provide paths for current flowing through, but essentially the two cases are different. Referring to the circular contact, the current prefers to flow through the middle of the current arm into the contact due to the relative shorter distance to the contact rather than the sides of the current arm. Then, near the contact region, the current would flow into a narrow path, enhancing the current crowding effect at the front end of the circular contact and nearby region. In contrast with additional nearby current path due to the δ, the circular contact directly changes the current distribution. Thus, the R_p caused by the circular contact is

remarkably larger than that by the δ, shown in Fig.2-8(b). Furthermore, the trend that the R_p decreases with the ρ_c for the circular contact is also observed. As the ρ_c is higher, current crowding effect near the contact is more serious for the circular contact, which leads to a significant difference between the results of the circular contact and of the square contact. By contrast, as the ρ_c decreases, because of the shortening of the transfer length, test structures with both the circular and the square contacts suffer from the current crowding effect too, and therefore the difference between the two kinds of contact shape reduces.

2-5-2-2 Considering the Recessed Contact

To analyze simply, only the elevated silicide/Si contacts, i.e., $m_j = 0$, are considered in previous subsections. However, in the real case, during the silicide formation, silicon is consumed and the recessed contact between silicide and silicon would be formed. It is generally believed that as the consumption of silicon increases during the silicide formation, the contact series resistance is susceptible to increase due to the decrease in active dopant concentration at the silicide/Si interface or increase in sheet resistance underneath silicide [68]. In addition, there is another current path at the side of recessed contact region which is being parallel with current flow at the contact under silicide layer, as illustrated in Fig.2-9 [67]. Briefly, as the recessed contact is taken into account, the current distribution would be different, and details are about to be described in this subsection.

Fig.2-10 and Fig.2-11 shows the relative error as a function of the recession depth with different ρ_c for $A_c = 50\times50\ nm^2$ and $1\times1\ \mu m^2$. It is observed that in both figures the ρ_{ce} becomes smaller as the recession depth increases, even lower than the actual ρ_c value. It could be explained by the enlarged effective A_c. As the recession is considered, the effective A_c would increase with the recession depth due to the

additional contact surfaces at the side of the recessed contact region. Evidently, the ρ_{ce} would decrease with the recessed depth.

In addition, the ρ_{ce} decreases faster for lower ρ_c is also noticeable in Fig.2-10 and Fig.2-11. It could be verified by the current transition from the diffusion layer to the silicide through the contact. Roughly there are two kinds of the current path: one is through the bottom contact, and the other is through the side contacts. For higher ρ_c value, the current tends to flow into the bottom contact instead of the side contacts, since the additional side current paths have larger effective resistances. Therefore, for higher ρ_c, the recession has less influence on the ρ_c extraction. On the other hand, for lower ρ_c, the additional side current paths would have lower effective resistances and consequently make an obvious difference to the ρ_c extraction. Thus, the ρ_{ce} decreases faster for lower ρ_c could be explained.

Last, as the recession is considered, the A_c dependence of the ρ_c extraction is analyzed. Comparing Fig.2-10 and Fig.2-11, it could be observed that as the A_c reduces, for all ρ_c values shown in Fig.2-10 with $A_c = 50\times50$ nm^2 the ρ_c extraction would be affected by the recessed contact more obviously, while in Fig.2-11 with $A_c = 1\times1$ μm^2 only lower ρ_c values would be affected. The reason could be that the additional side contacts have more influence on the ρ_c extraction for smaller $A_{c.}$ since the side contacts would be relatively compatible to the bottom contact. Hence, as the recession is considered the A_c dependence is more serious for smaller A_c.

2-5-3 Three-Dimensional Simulation of the Self-Aligned mTLM Structure

Fig.2-12 demonstrates the extraction procedure of the mTLM method with $W_c = 1$ μm and $L_c = 2$ μm as $\rho_c = 1\times10^{-7}$ Ω-cm^2 in this simulation. Fig.2-13 shows the relative error values as a function of ρ_c with L_c=1 μm, 1.5 μm and 2 μm using the

self-aligned mTLM method. It is noticed that the longer L_c results in lower error; in addition, as the ρ_c reduces from 1×10^{-7} toward 1×10^{-8} Ω-cm^2, the role of L_c becomes more significant. Since the R_s values extracted from the mTLM method are almost the same for all L_c, i.e., 217.17 ± 0.01 Ω/□, it can be inferred that the extraction error is caused by the R_f term in the total resistance. The L_c determines the R_f, and the ratio of the L_c and the L_T determines the extraction error according to Eq.1-9. Thus, the longer L_c results in lower error because the basic requirement of $L_c >> L_T$ can be better fulfilled. It can be also observed that as L_c = 2 μm, the extraction error is only 3 ± 1%. Also, the ρ_c value is related to the L_T, shown in Eq.1-10, and therefore the requirement of $L_c >> L_T$ would be reached easier as the ρ_c becomes lower, resulting in more accurate ρ_c extraction. Furthermore, the lower ρ_c value allows a smaller denominator of the ratio of the L_c and the L_T, which leads the L_c to have a greater impact on the extraction accuracy and consequently the longer L_c causes lower extraction error as the ρ_c in a lower range.

Last, in Fig.2-14(a), the relative error for the CBKR method and the self-aligned mTLM method with L_c = 2 μm is compared. As the ρ_c reduces to 2×10^{-8} Ω-cm^2, the error of the CBKR method increases even though the A_c is 50×50 nm^2 and the δ is 0 nm. In contrast, the error of the mTLM method reduces with the decrease of ρ_c until 2×10^{-9} Ω-cm^2, and the error is less than 20% at $\rho_c = 1\times10^{-9}$ Ω-cm^2. In order to discuss the above results, the difference between the ρ_{ce} and ρ_c as a function of the actual ρ_c for both CBKR and mTLM method is shown in Fig.2-14(b). The ρ_{ce}-ρ_c for the CBKR method is not sensitive to the ρ_c values since the parasitic resistance is almost independent of the actual ρ_c and has been mentioned in section 2-5-1. For the mTLM method, on the other hand, the ρ_{ce} value decreases with the ρ_c until 2×10^{-9} Ω-cm^2 in this simulation. It could be explained by the ratio of the L_c and L_T as well. Lower ρ_c enlarges the ratio of L_c/L_T, and hence improves the extraction accuracy. However,

lower ρ_c would suffer from other parasitic term because the corresponding R_f is so small that the parasitic term could be compatible to the R_f. For instance, the extrapolation would be a possible error source and especially dominates the R_f when R_f is only a few ohm as the ρ_c in the range of 10^{-9} Ω-cm^2. It is noticed that in essence the ρ_{ce} would be always larger than or approaching the ρ_c since the hyperbolic-cotangent term, which dominates the extraction accuracy in the mTLM method in Eq.1-9, is always larger than or approaching 1; nevertheless, if the error resulting from the extrapolation is considered, the ρ_c extraction would be deviated irregularly.

2-5-4 Issues of the mTLM Structure

2-5-4-1 Considering the Variation of Doping Concentration in Semiconductors

In the extraction procedure of the mTLM method, the sheet resistance (R_s) of the diffusion layer is regarded as a critical parameter. Since the R_s is determined by the doping concentration distribution of the diffusion region, if the variation of dosage of implantation is considered, the R_s would not be a constant value for all test structures used during the extraction procedure. The R_f extrapolated from Eq.1-8 may not correct, and then the ρ_{ce} may deviate from the actual ρ_c value. Therefore, for the mTLM method, the extraction error stems from the variation of fabrication process would be understandable.

To investigate the influence of variation of doping concentration in diffusion region explicitly, statistic including 100 extraction results is used to depict the reality more closely. First, for the extrapolation of R_f value from the R_{total}-L_d plot, 100 R_{total} values, corresponding respectively to different setting doping concentrations of the top surface of the diffusion region with 1×10^{20} cm^{-3} ± 5% in Gaussian distribution for each L_d, are obtained by using test structures with W_c = 1 μm and L_c = 2 μm and the

actual $\rho_c = 1\times10^{-8}$ Ω-cm^2. Fig.2-15 shows the distribution of the R_{total} for each L_d. Next, randomly choose R_{total} value for each L_d, extrapolate the R_f, and then extract the ρ_c according to the mTLM procedure. Repeat the above-mentioned process several times, like 100 times in this subsection, to make the results closer to the normal distribution in theory. Fig.2-16(a) illustrates the extrapolation of the R_{total}-L_d plot, and Fig.2-16(b) and (c) show the distribution of the extracted R_s and R_f, respectively. According to the statistic, the R_s is 218 Ω ± 5.5%, while the R_f is 11.8 Ω ± 370%. It could be observed in Fig.2-16(a) that after the extrapolation, the R_f could vary in a wide range, and in certain cases $R_f < 0$ may even occur, which is unreasonable in reality. The ρ_{ce} values, extracted from R_f values, are illustrated in Fig.2-16(d) ignoring the cases of $R_f < 0$. Comparing to the actual ρ_c value of 1×10^{-8} Ω-cm^2, a large range varying from 10^{-10} to 10^{-7} Ω-cm^2 of the ρ_{ce} is obtained. Inaccurate extrapolation is the major cause. In essence, the extrapolation method tends to contain errors; indeed, changes of the R_{total} value make the extrapolated results more diverse. In conclusion, it is indicated that when the mTLM method is utilized, the variation of doping concentration in diffusion region may lead to the incorrect extrapolation, and consequently deviate the extraction accuracy, which is a crucial difficulty for the mTLM method.

2-5-4-2 Considering the Variation of Tapered Sidewall Angle of the Diffusion Region

To define the active region clearly, the STI are chosen in this thesis and the vertical sidewalls of the diffusion region are expected for the mTLM structure. However, based on the trench etching process and the stress consideration, tapered sidewalls are preferred rather than vertical sidewalls. Compromised between the stress issue and the requirement for precisely defining the gate length, the appropriate angle

should be larger than 88.2° according to the ITRS [21]. In this subsection, diffusion region with tapered sidewalls is considered and the influence of the tapered sidewall slope on the extraction error of the mTLM method is verified.

Similar to the settings in previous subsection, to investigate the influence of the variation of the tapered sidewall angles of the diffusion region explicitly, statistic including 100 extraction results is used. The same, test structures with W_c = 1 μm and L_c = 2 μm and the actual $\rho_c = 1\times10^{-8}$ Ω-cm^2 are used in this part. The sidewall angles are set 88 ± 2° in the Gaussian distribution for all test structures. The extraction procedure here is identical to that in section 2-5-4-1, and the distribution of the R_{total} for each L_d is shown in Fig.2-17. Comparing with the results in Fig.2-15, the distribution of the R_{total} values for every L_d in Fig.2-17 is more concentrated rather than that in Fig.2-15, indicating that the variation of tapered sidewall angles could be less significant to the extraction accuracy than the doping concentration of the diffusion region. Then, the distributions of the R_s, the R_f, and the ρ_{ce} are demonstrated in Fig.2-18(a), (b), and (c), respectively. The R_s is 216.7 Ω ± 0.7%, while the R_f is 14.7 Ω ± 30% and the ρ_{ce} is 1×10^{-8} Ω-cm^2 ± 62%. In contrast with the results in Fig.2-16, the extraction accuracy would be affected slightly by the variation of the tapered sidewall angles indeed. It is noticed that both the doping concentration and the tapered sidewall angle vary the R_s basically. The variation of the doping concentration would change the R_s directly, while the settings of the variation of the tapered sidewall angle would change the R_s in a slighter amount. Accordingly, it is reasonable that in this work the variation of tapered sidewall angles plays a minor role on the error of the ρ_c extraction rather than the variation of doping concentration of the diffusion region.

2-5-4-3 Considering the Recessed Contact

Similarly to the CBKR method mentioned in section 2-5-2-2, as the recessed contact is considered, an additional contact surface arises at the side of the recessed contact and the current distribution of the mTLM structure would be changed. As the recession happens, the R_f becomes to be determined by the parallel connection of the current path at the side contact and at the planar contact. Also, the extraction results would be affected by different ρ_c values as well. In Fig.2-19(a), the relative error as a function of the recession depth with various ρ_c values is shown. In Fig.2-19(b), the difference between the ρ_{ce} and the ρ_c is also presented, which would help the following argument understandable. First of all, for higher ρ_c, the ρ_{ce} increases with the recession depth. In this case, the current tends to flow into the planar contact instead of the side contact which has a relative larger resistance with smaller cross-section and/or higher ρ_c. As the recession depth increases, the depth of the diffusion region decreases, raising the R_s under the contact and the ρ_{ce} consequently. On the contrary, for lower ρ_c, the side contact with a lower ρ_c value would be a preferable path for the current flowing into the contact, though the R_f is larger than that without the recessed contact due to the smaller cross-sectional area of the side contact. Then, as the recession depth increases, i.e., the side contact becomes dominant, the deeper the recession depth is, the more the current flows into silicide through the side contact with gradually larger cross-section, inferring that the ρ_{ce} would decrease with the deeper recession of the contact. Therefore, it could be concluded that all the ρ_{ce} values increase for shallow recession of the contact, 10 nm in this simulation for example; as the contact recesses deeper enough, the ρ_{ce} values increase more for higher ρ_c, while reduce for lower ρ_c.

Moreover, the above results are compared to those of the CBKR method in Fig.2-10, concluding that as the recession depth increases, the extraction results would

reduce gradually for the CBKR method, while increase at first and then reduce for the mTLM method.

Briefly, the CBKR structure provides an easier extraction method, and could obtain better extraction accuracy by reducing the A_c and choosing an appropriate δ. However, limitations caused by fabrication process would degrade its accuracy. Smaller A_c would suffer from the corner rounding more seriously and consequently would arise the extraction error. The recessed contact resulting from silicidation process would underestimate the ρ_c and result in a more complex situation. Because these errors originate from some unavoidable parameters, they would be unfortunately inevitable and therefore limit the accuracy.

As for the mTLM structure, it is easier to be fabricated, and it shows a better accuracy at low ρ_c regime according to the simulation results in this thesis. It is free from the δ owning to its self-aligned feature. The most difficult for the ρ_c extraction is the sensitivity to the process variation. The recessed contact changes the current distribution and has a more complicated influence for the mTLM method. The dopant concentration and the tapered sidewall angle of the active region would vary with the process and hence vary the ρ_{ce}. Fortunately, errors originating from the process variation could be eliminated by averaging lots of data. According to the law of large numbers in probability theory, the average of the results obtained from a large number of trials should be close to the expected value, and will tend to become closer as more trials are performed [69]. Therefore, the average of a large amount of the extracted results could avoid the dependence of the process variation and enhance the ρ_c extraction validity. This would enhance the applicability of the mTLM method. It is noticed that the extraction procedure is complicated by nature for the mTLM method, and if the large number of data is needed, it would be more complicated and time-consuming. Finally, in this simulation, it is observed that even though both

methods could improve their accuracy by some means, there are still error sources affecting the extracted results.

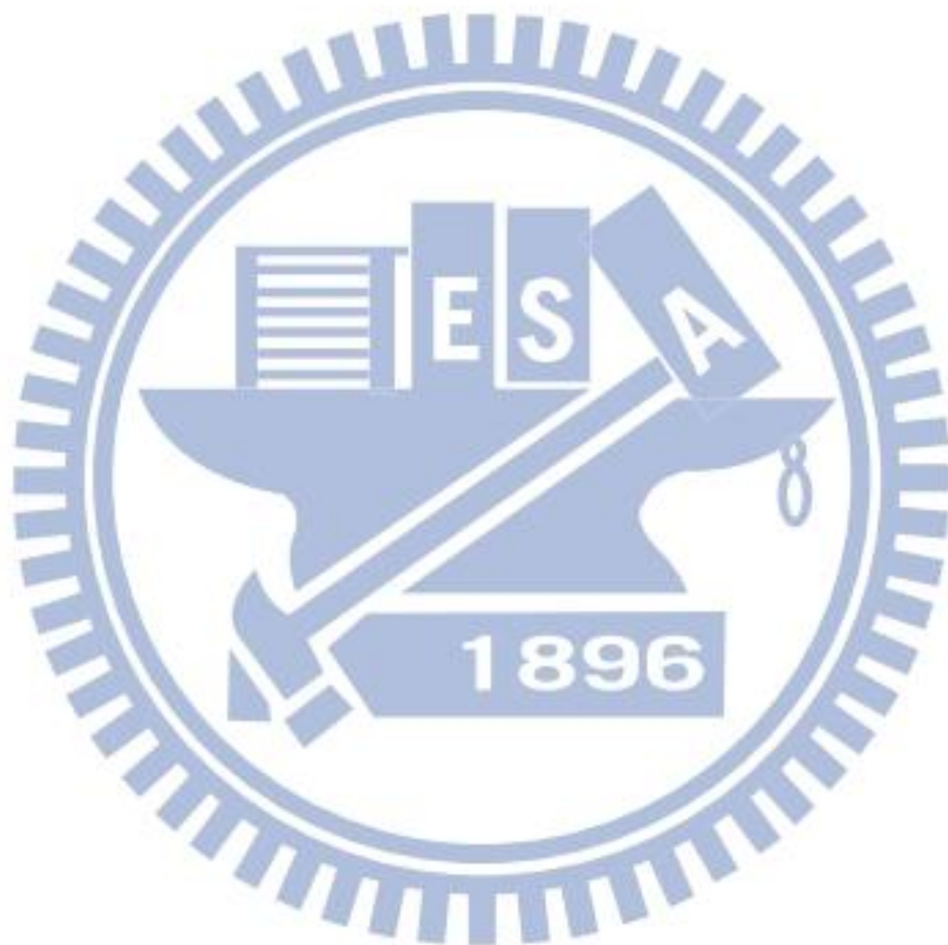
ESA
1896

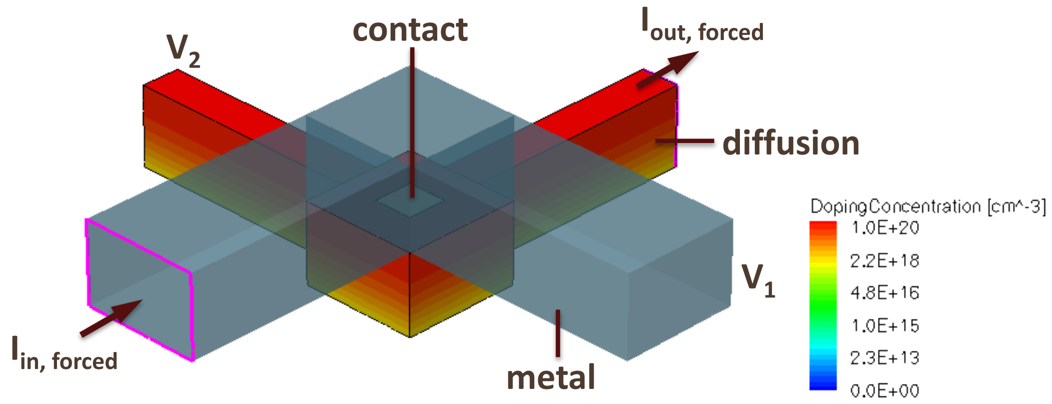

Fig. 2-1 The general 3-D simulated structures of the CBKR method.

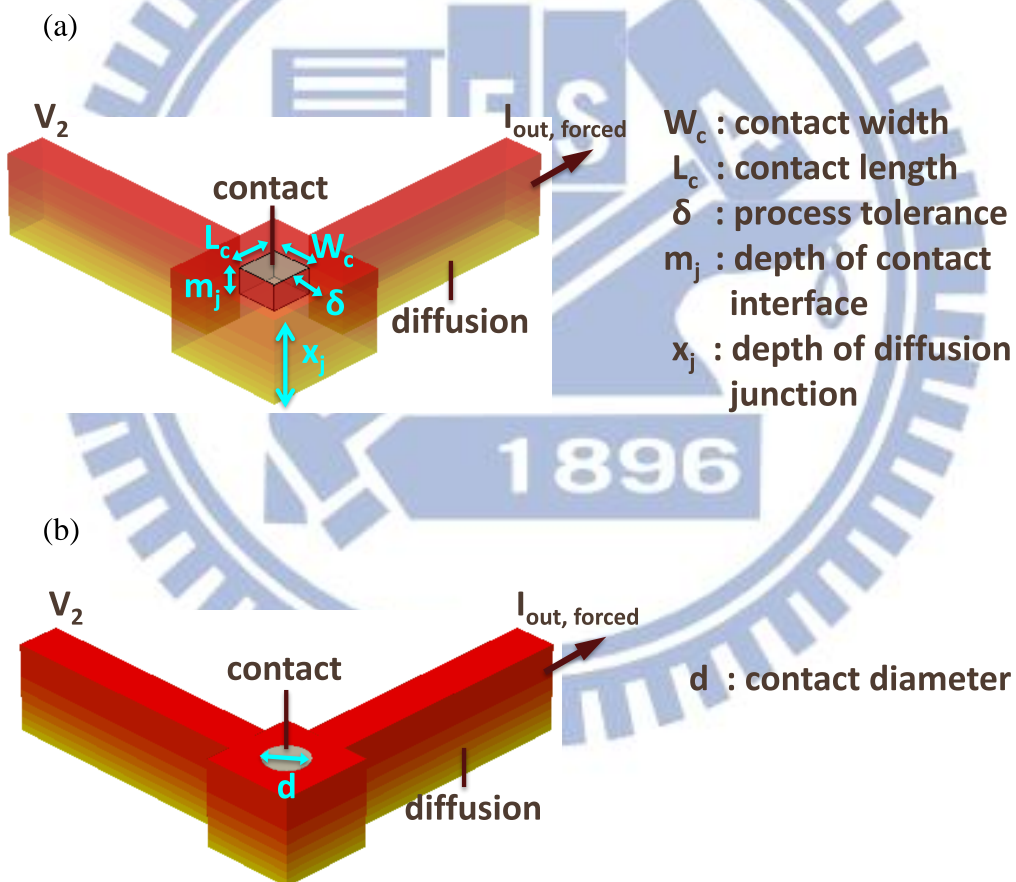

Fig. 2-2 Definition of parameters for CBKR method (a) with a square contact, and (b) with a circular contact. The metal layer is not drawn here.

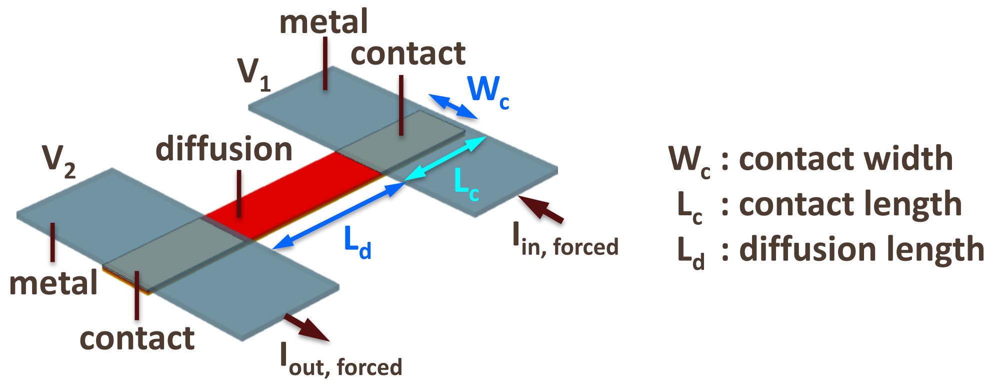

Fig. 2-3 The general 3-D simulated structure and definition of parameters of the mTLM method.

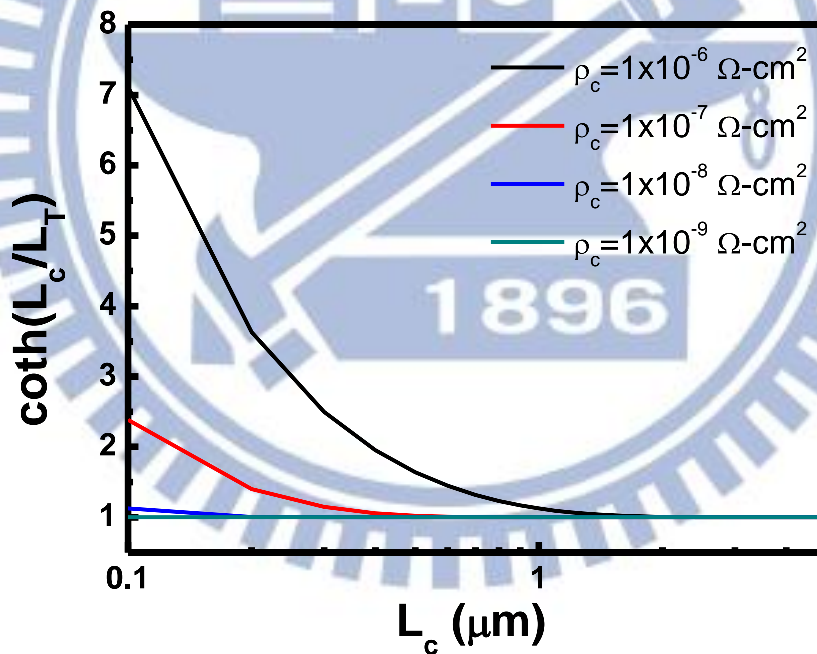

Fig. 2-4 Design guideline of the L_c of the mTLM extraction procedure. The $\coth(L_c/L_T)$ approaches 1 as $L_c >> L_T$.

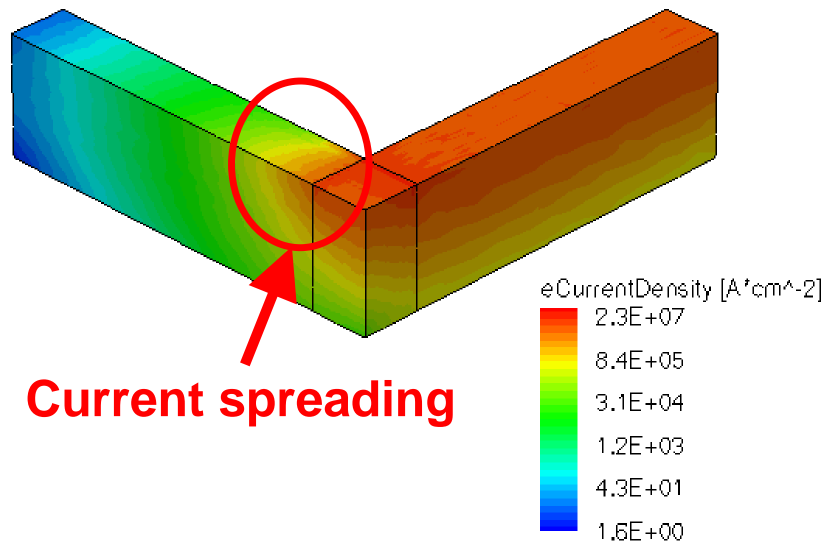

Fig. 2-5 Simulated current distribution of the CBKR structure as δ = 0 using the CBKR structure.

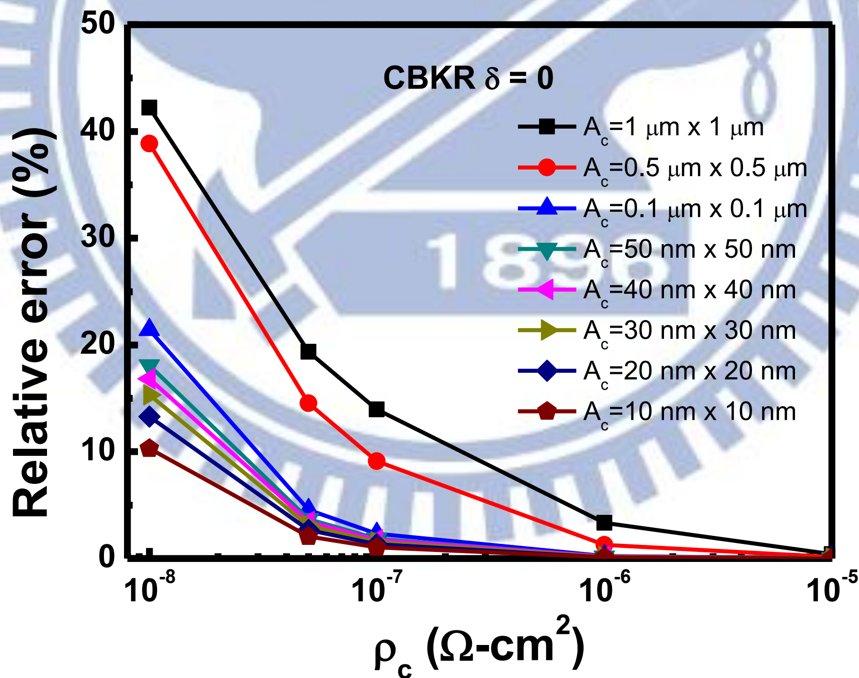

Fig. 2-6(a) Relative error versus the actual ρ_c with various A_c values as $\delta = 0$ using the CBKR structure.

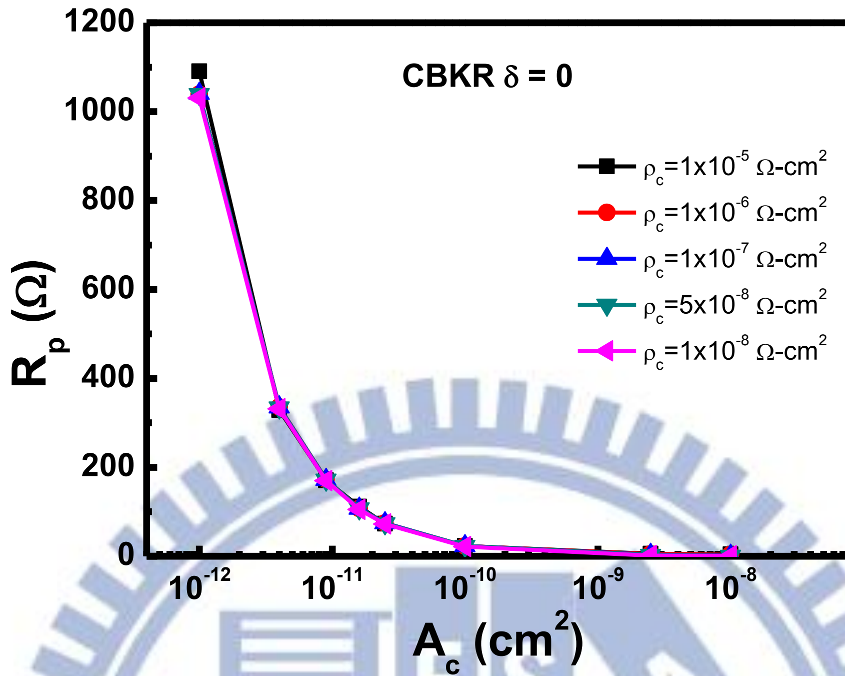

Fig. 2-6(b) Parasitic resistance versus the contact size with various ρ_c values as $\delta = 0$ using the CBKR structure.

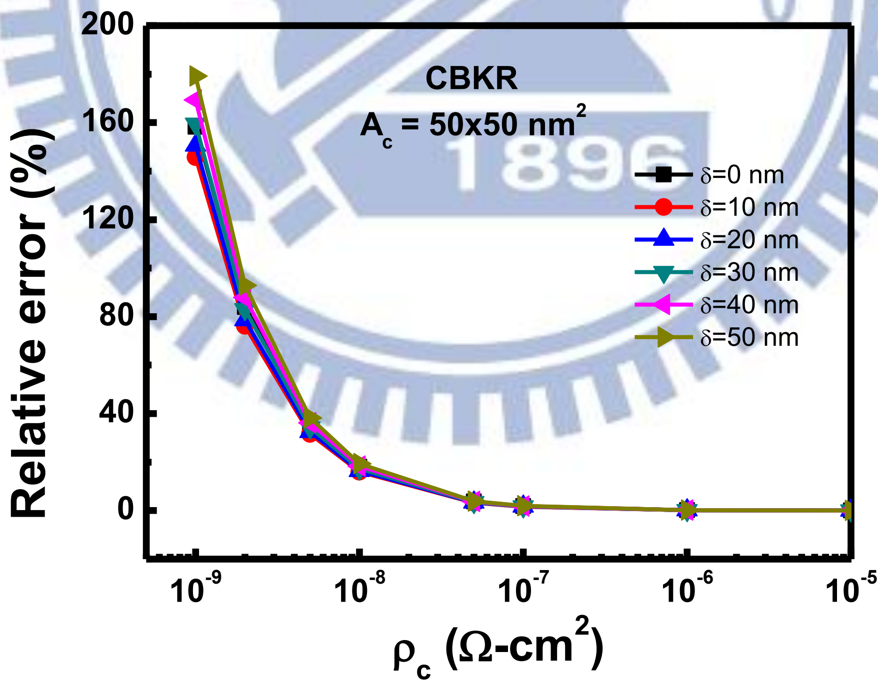

Fig. 2-7(a) Relative error versus the actual ρ_c with various δ values as $A_c = 50\times50$ nm^2 using the CBKR structure.

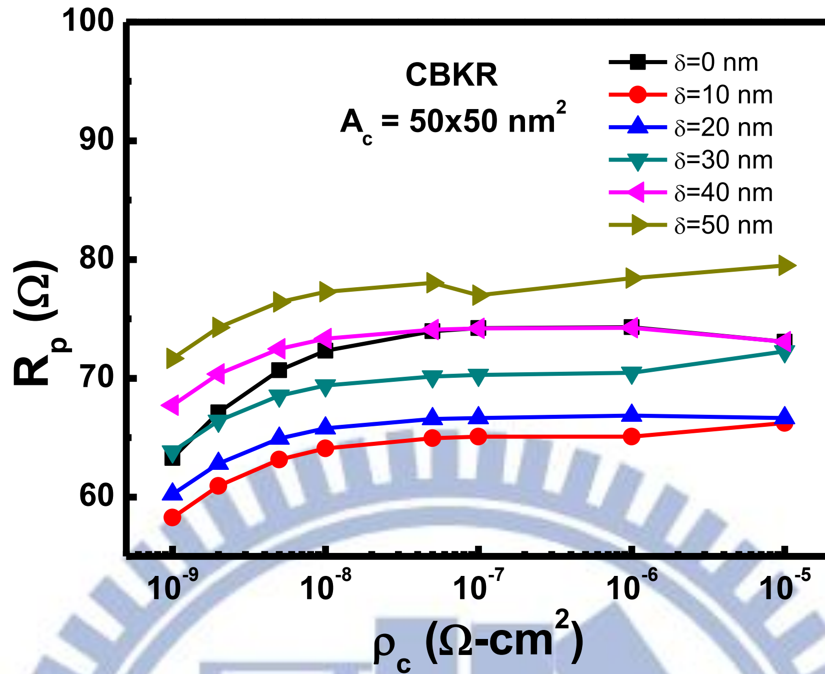

Fig. 2-7(b) Parasitic resistance versus the actual ρ_c with various δ values using the CBKR structure.

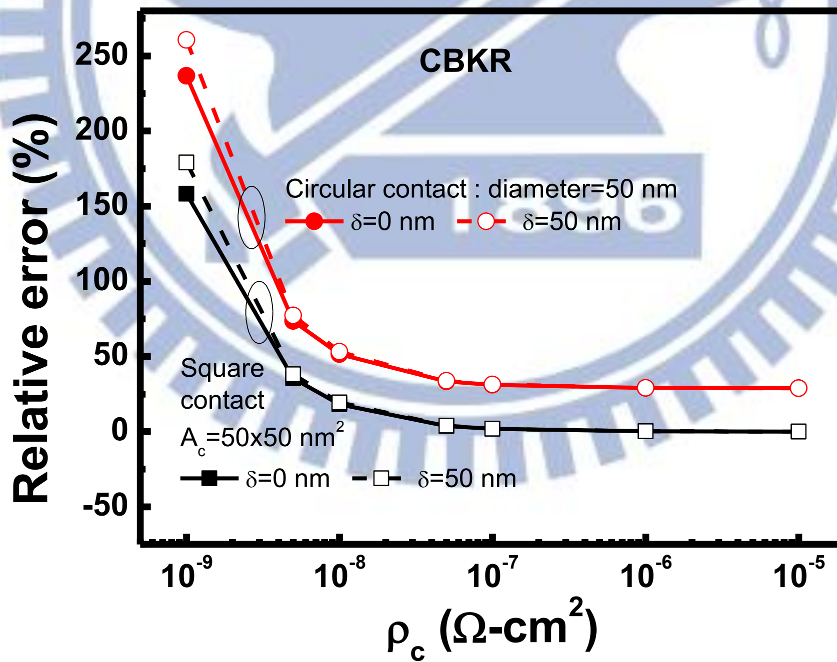

Fig. 2-8(a) Comparison of the relative error between the square contacts and the circular contacts using the CBKR structure. The cases that δ = 0 and δ = 50 nm are both exhibited.

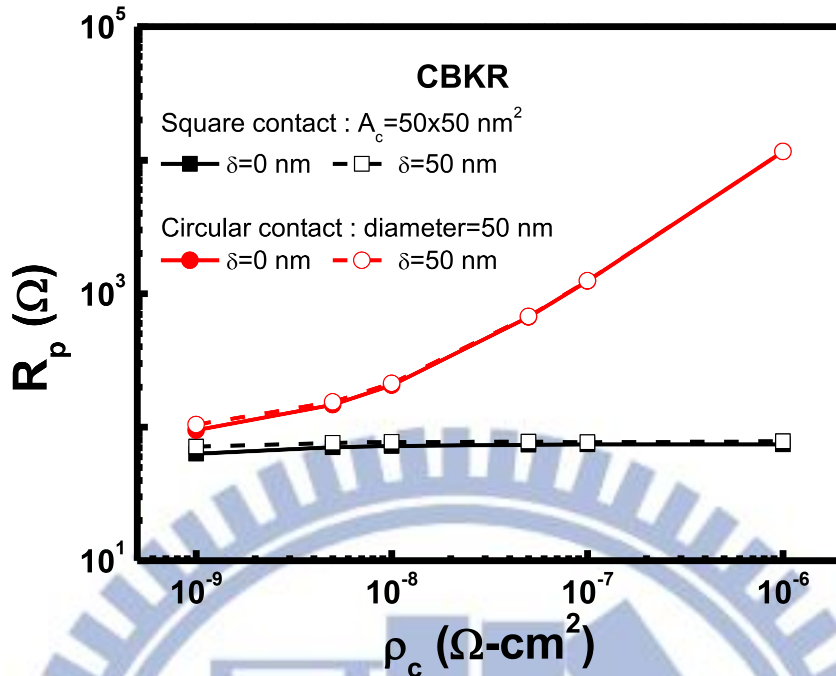

Fig. 2-8(b) Comparison of the parasitic resistance between the square contacts and the circular contacts using the CBKR structure. The cases that δ = 0 and δ = 50 nm are both exhibited.

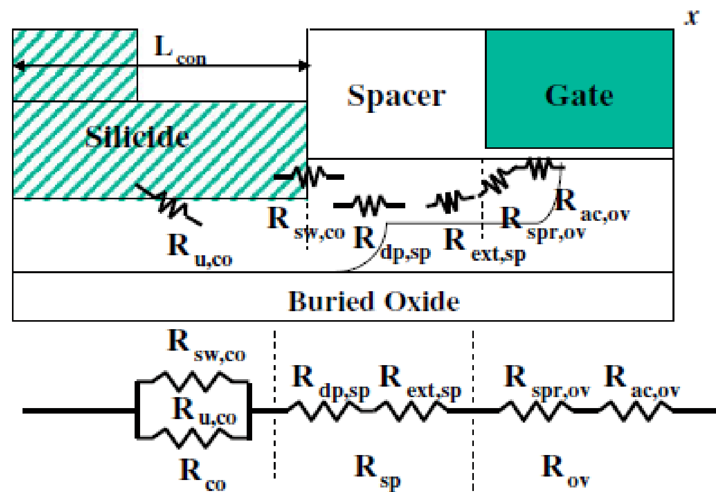

Fig. 2-9 Cross-section diagram of total S/D resistance with the recessed silicide taken in account. The contact resistance includes two parallel components: the resistance underneath the silicide and the resistance at the side of the recessed contact [67].

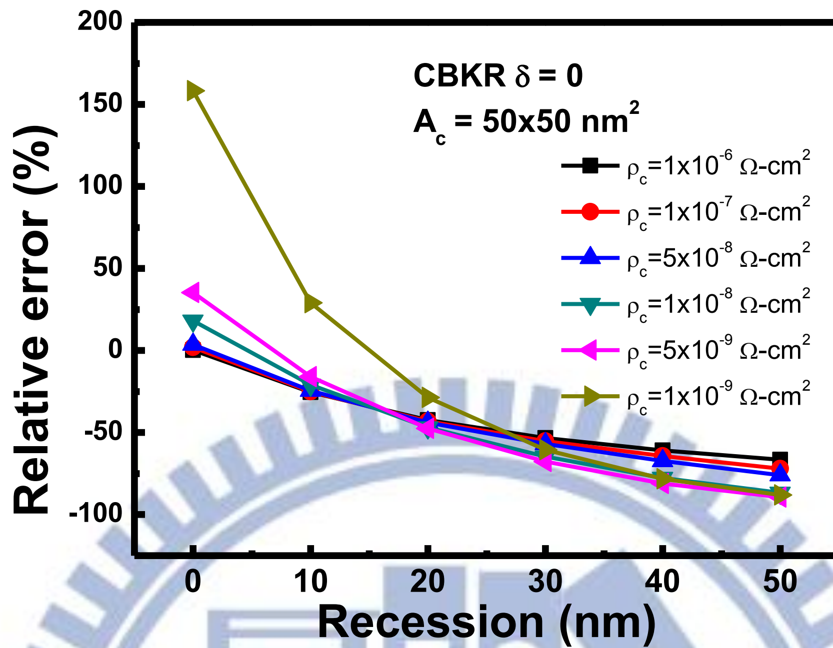

Fig. 2-10 Relative error versus the recession depth with various ρ_c as $A_c = 50\times50\ nm^2$ using the CBKR structure.

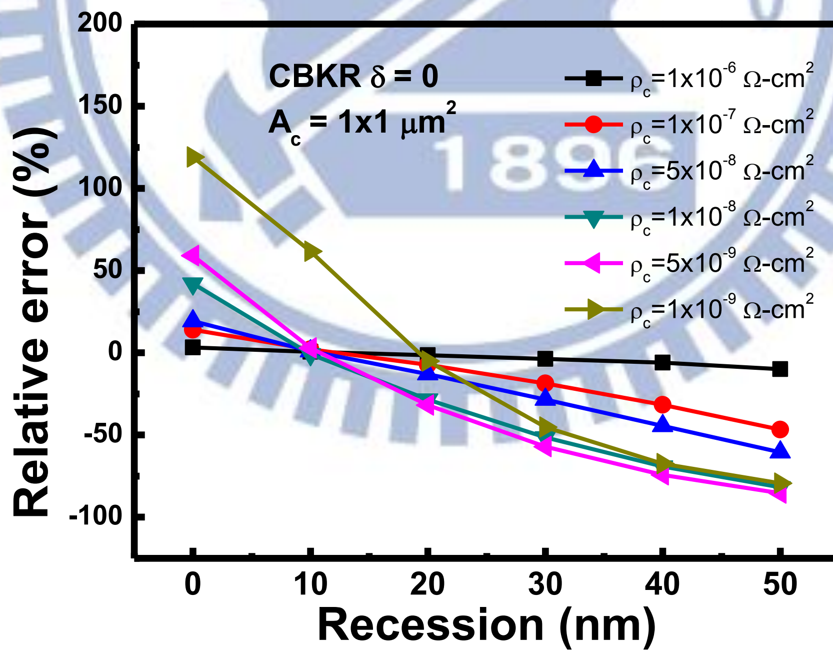

Fig. 2-11 Relative error versus the recession depth with various ρ_c as $A_c = 1\times1\ \mu m^2$ using the CBKR structure.

(a)

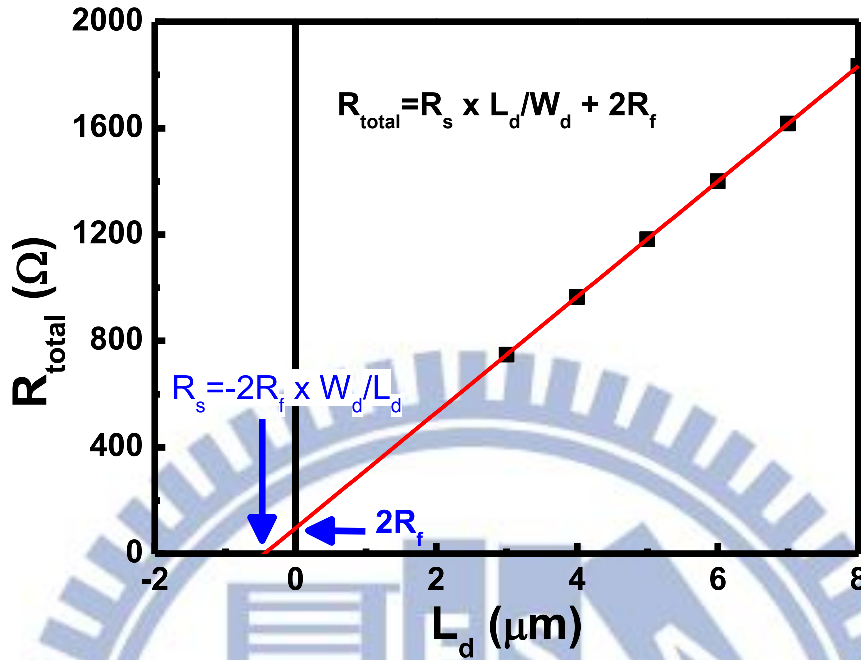

(b)

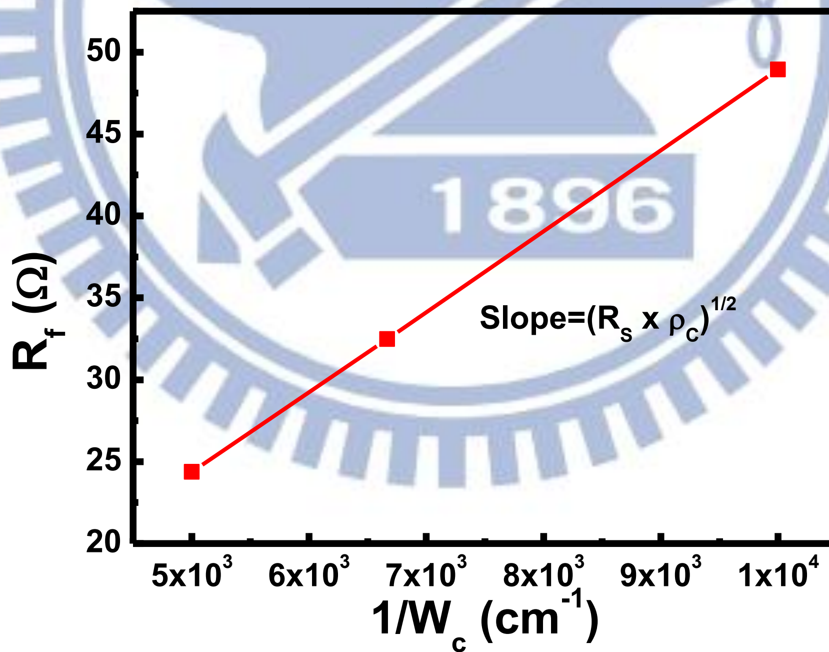

Fig. 2-12 Extraction procedure of the ρ_c using the mTLM structure with W_c = 1 μm and L_c = 2 μm as $\rho_c = 1\times10^{-7}$ Ω-cm^2. (a) The R_f is obtained from the y-intercept of the R_{total}-L_d plot. (b) The ρ_c is extracted from the slope of the R_f-1/W_c plot.

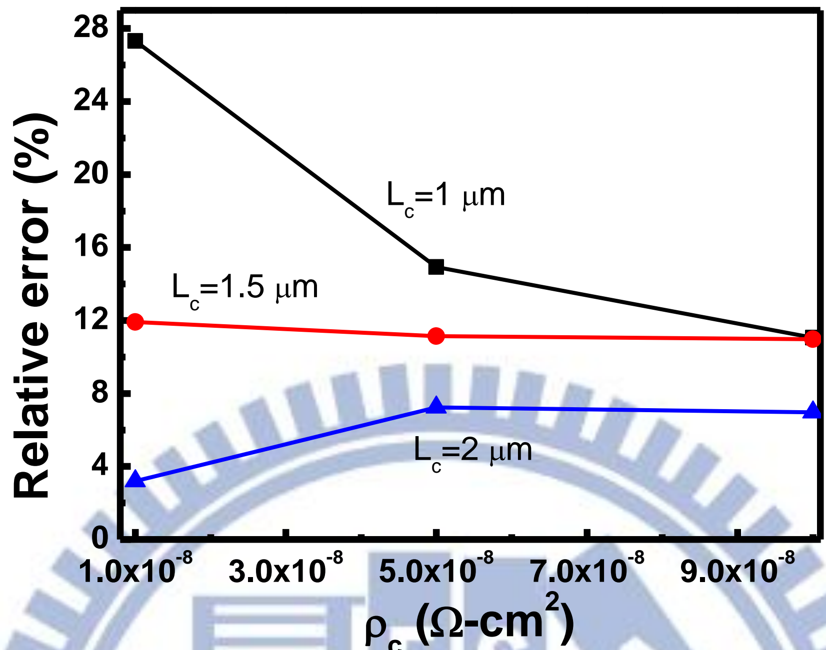

Fig. 2-13 Relative error versus the actual ρ_c with different L_c using the mTLM procedure.

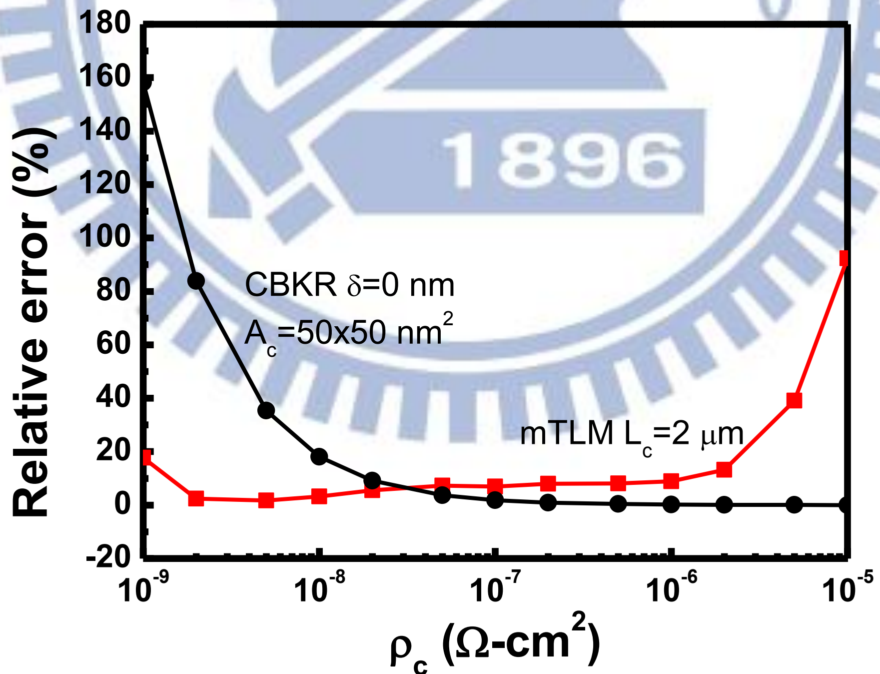

Fig. 2-14(a) Comparison of the relative error between the CBKR and mTLM methods.

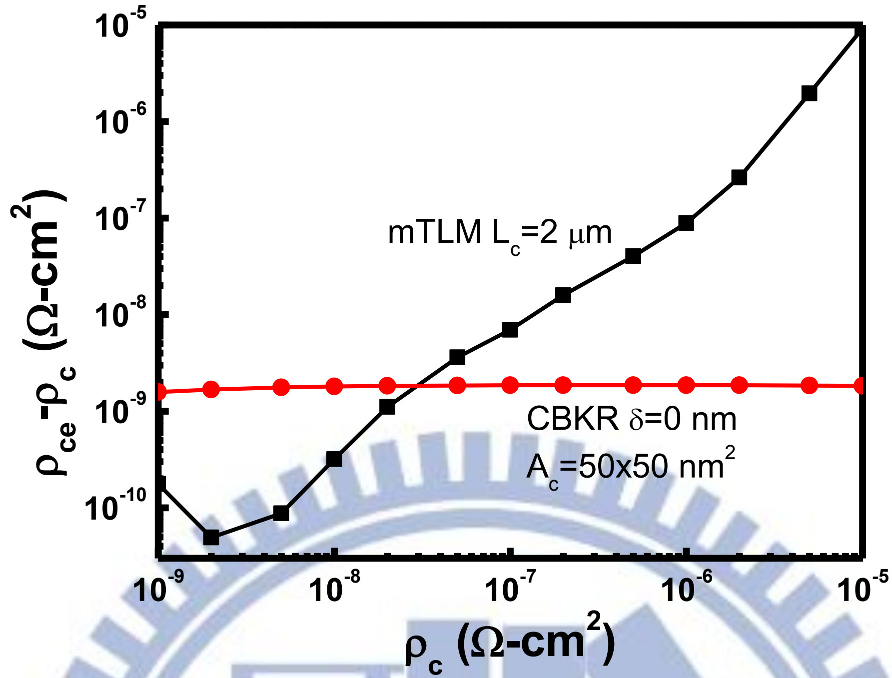

Fig. 2-14(b) Comparison of the accuracy between the CBKR and mTLM methods.

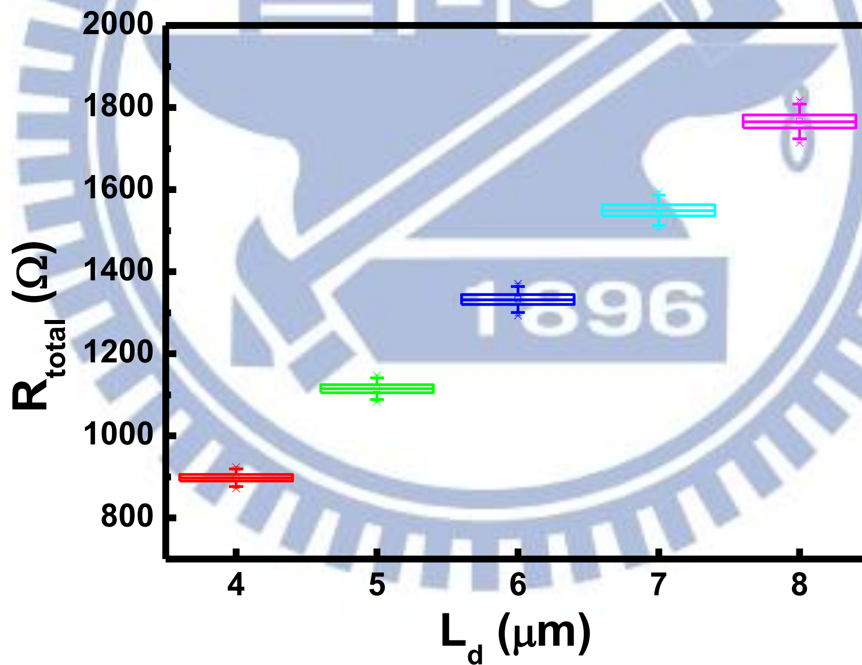

Fig. 2-15 Distribution of the R_{total} values for each diffusion length (L_d) as the variation of doping concentration in semiconductors is considered. For each L_d, 100 test structures are used with the doping concentrations of top surface set 1×10^{20} cm^{-3} ± 5% in Gaussian distribution.

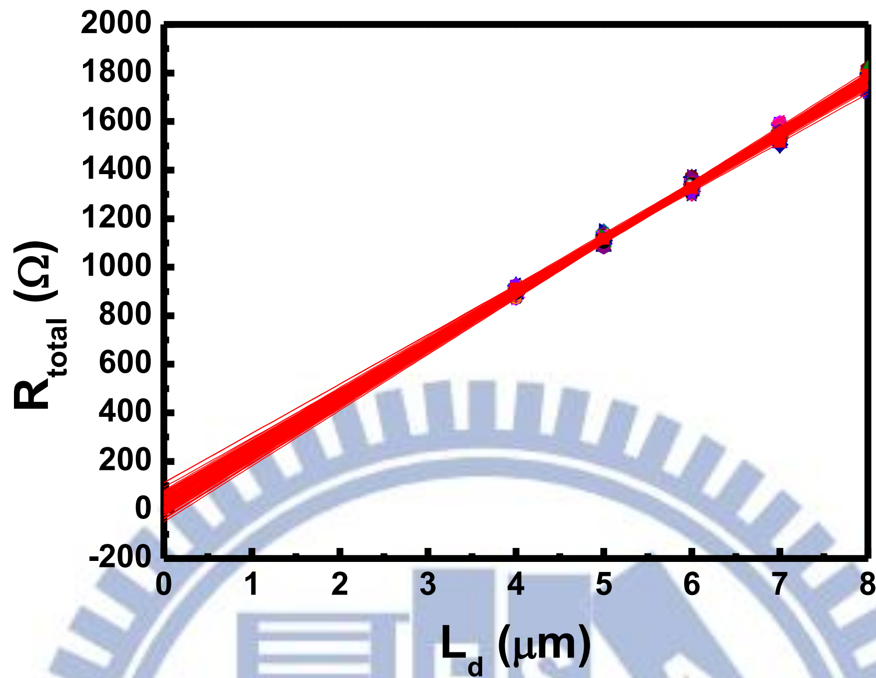

Fig. 2-16(a) R_f extrapolated from the intercept of R_{total}-L_d plot involving 100 extraction results. The R_f varies in a wide range, and $R_f < 0$ may even occur.

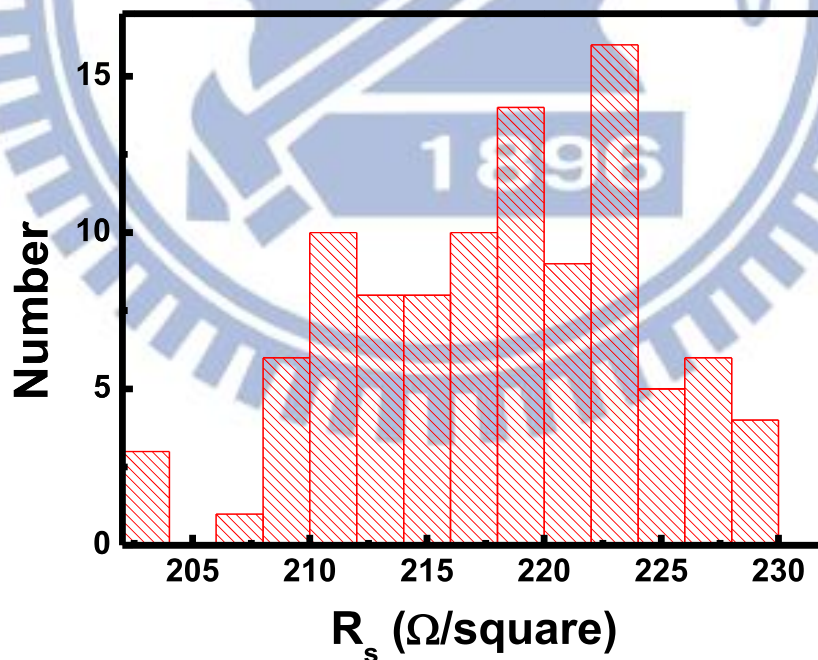

Fig. 2-16(b) Distribution of the R_s involving 100 extraction results from the slope of the R_{total}-L_d plot as the variation of doping concentration is considered.

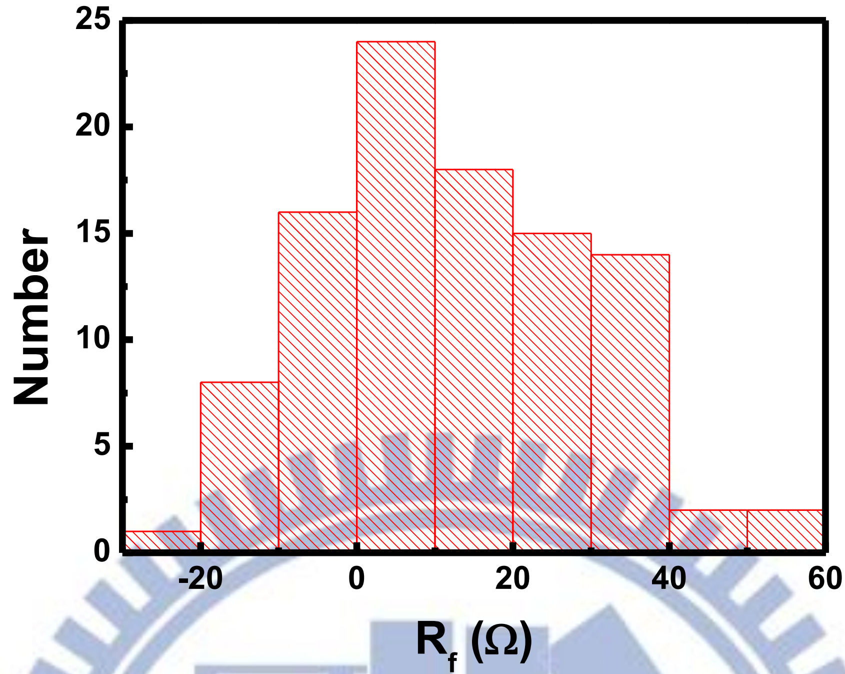

Fig. 2-16(c) Distribution of the R_f involving 100 extraction results from the y-intercept of the R_{total}-L_d plot as the variation of doping concentration is considered. For certain cases, $R_f < 0$ occurs, which is impossible to happen in reality.

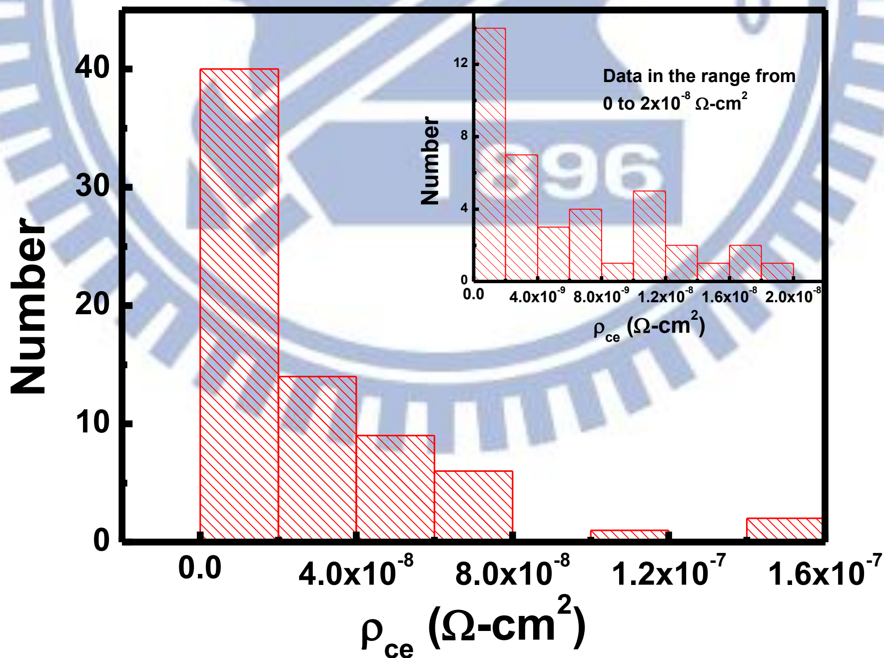

Fig. 2-16(d) Distribution of the ρ_{ce} involving 100 extraction results from the mTLM method as the variation of doping concentration is considered. The inset shows the data in the range from 0 to 2×10^{-8} Ω-cm^2 in detail.

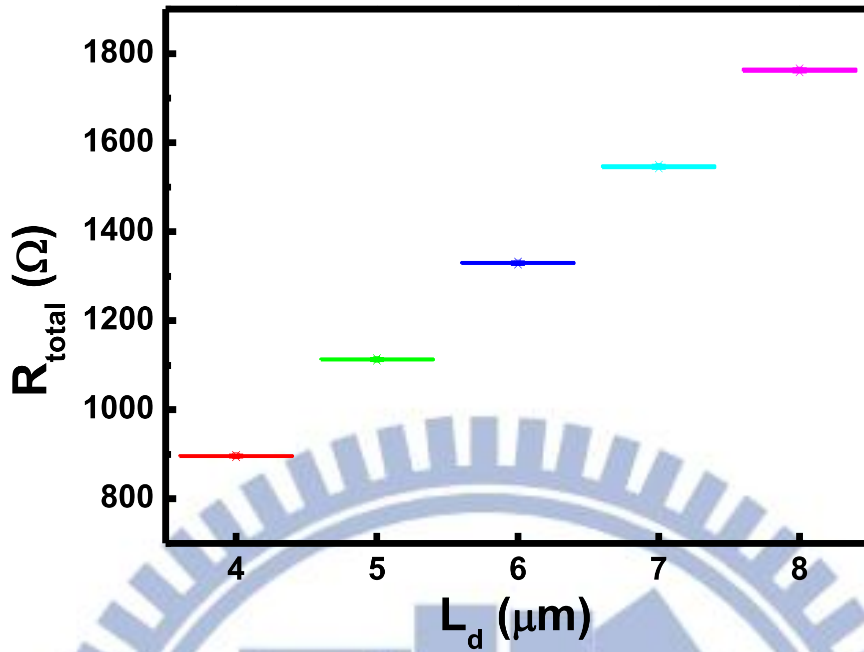

Fig. 2-17 Distribution of the R_{total} values for each diffusion length (L_d) as the variation of tapered sidewall angles of the diffusion region is considered. For each L_d, 100 test structures are used with sidewall angles set 88 ± 2° in Gaussian distribution.

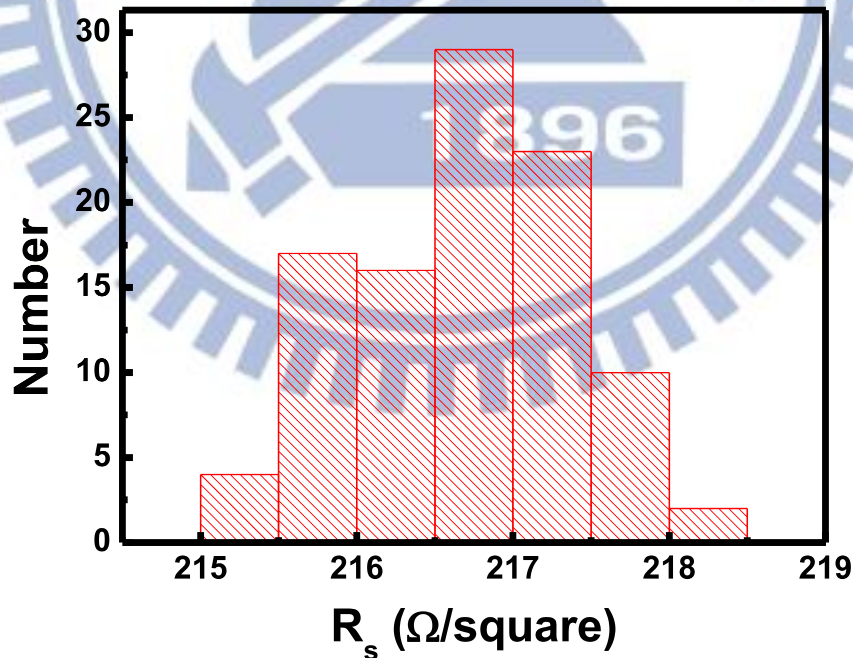

Fig. 2-18(a) Distribution of the R_s involving 100 extraction results from the slope of the R_{total}-L_d plot as the variation of tapered sidewall angles is considered.

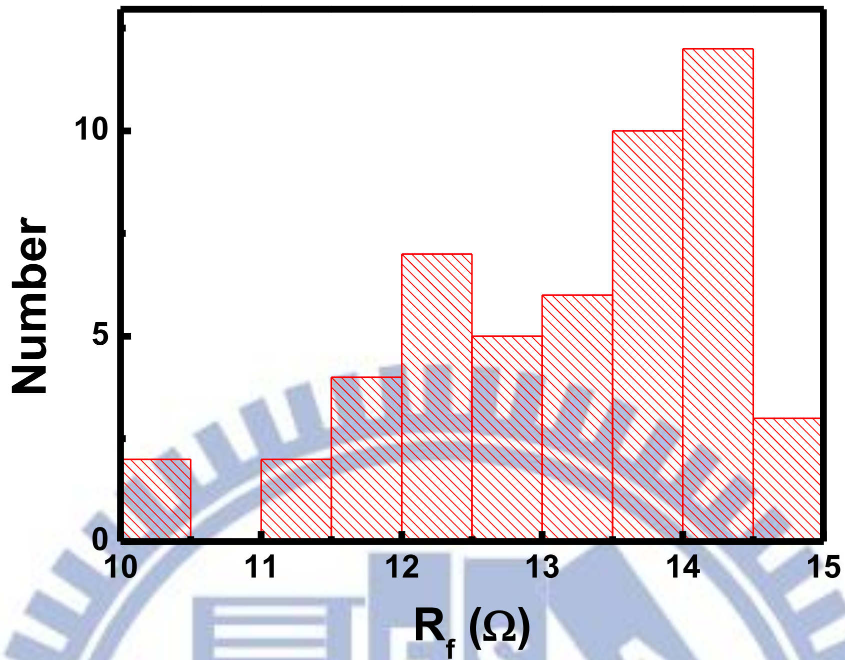

Fig. 2-18(b) Distribution of the R_f involving 100 extraction results from the slope of the R_{total}-L_d plot as the variation of tapered sidewall angles is considered.

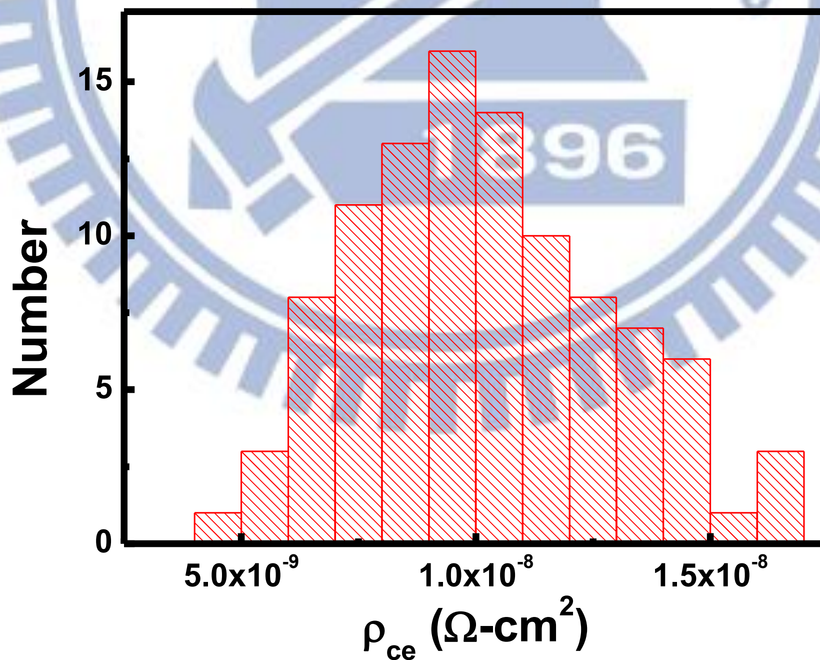

Fig. 2-18(c) Distribution of the ρ_{ce} involving 100 extraction results from the mTLM method as the variation of tapered sidewall angles is considered.

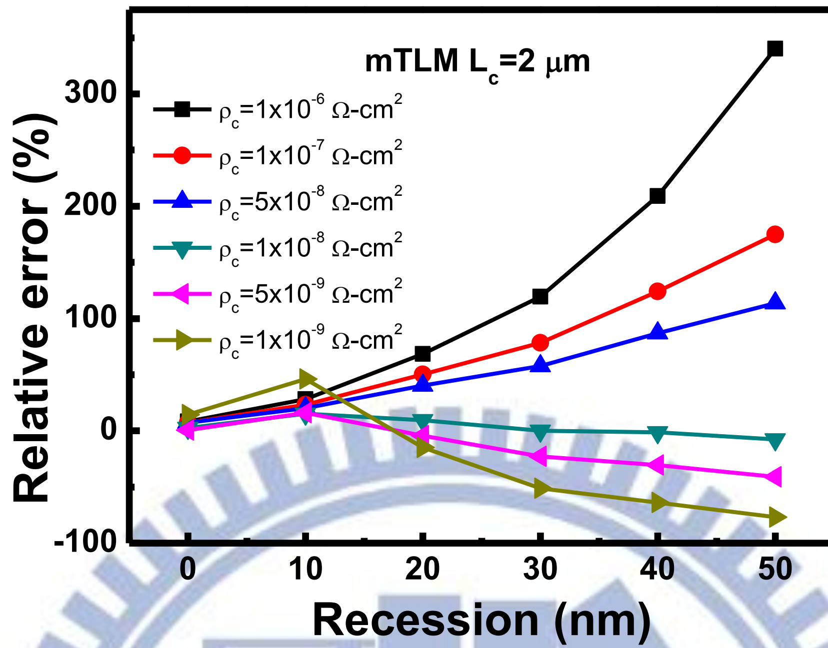

Fig. 2-19(a) Relative error versus the recession depth with different ρ_c values using the mTLM structures.

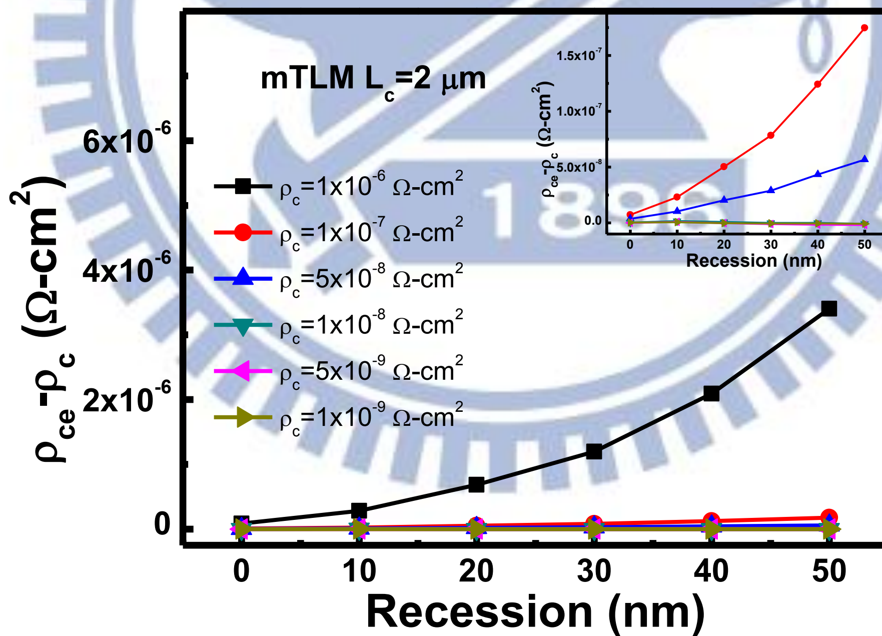

Fig. 2-19(b) The difference between the ρ_{ce} and ρ_c versus the recession depth with different ρ_c values using the mTLM structures. The inset shows the results as ρ_c from 1×10^{-6} to 1×10^{-9} Ω-cm^2 in detail.

Chapter 3
Experiments and Discussion

3-1 Overview

The design guidelines of test structures for both the CBKR and the mTLM methods have been described in the previous chapter. According to the foregoing understanding, considering the feasibility to fabricate test structures successfully, several experimental settings are shown in section 3-2. Then, in section 3-3, process flow is presented in detail. Finally, section 3-4 shows the experimental results and discussion.

3-2 Experimental Settings of the CBKR Method and the mTLM Method

This thesis studies contact resistivity measurements by the CBKR method and the mTLM method. All test structures can be realized by a same process flow, and therefore after the fabrication, results of each method could be compared reasonably. Test structures are described as following:

1. The CBKR structures

The contact area (A_c) values of the CBKR structures used in this thesis are designed in 2×2 μm^2, 3×3 μm^2, 5×5 μm^2, 7×7 μm^2 and 10×10 μm^2. The widths of current arms and voltage arms are designed to be the same values as the contact widths. The process tolerances (δ) are considered with 50 nm, 0.1 μm, and 0.3 μm.

2. The mTLM structures

The contact width (W_c) values of the mTLM structures used in this thesis are

designed in 1 μm, 1.5 μm, and 2 μm. The contact length (L_c) values are designed in 1 μm and 2 μm.

Fig.3-1 shows the schematic top view and cross-sectional view for the CBKR structure and the mTLM structure, respectively. The (100)-oriented n-type silicon wafers were used as a start. The active areas were defined by shallow trench isolation (STI) using I-line lithography. After the STI was fabricated, BF_2^+ ion implantation was performed at 15 keV to a dose of 5×10^{15} cm^{-2}. Next, a 1000 ℃, 5 seconds rapid thermal annealing (RTA) was used to activate the dopant and attain shallow junctions. Then, a SiO_2 isolation layer was deposited. After contacts were patterned by I-line lithography, the nickel (Ni) was deposited as the material for silicide formation with TiN as a capping layer. By lift-off process, the Ni contact was formed, followed by a 500 ℃, 30 seconds RTA to form NiSi. Subsequently the unreacted Ni and TiN were removed by wet etching. After the lithography process using a contact aligner system, aluminum (Al) was deposited and patterned by lift-off process. Finally, a 400 ℃, 30 minutes N_2 annealing was performed to sinter the Al pad. Then the whole process was finished.

The completed process flow would be described in next section.

3-3 Process Flow

The details of process are illustrated in Fig.3-2:

1. Laser marking of 6-inch Si wafer

The 6-inch n-type silicon wafers were commercially obtained from Wafer Works Corp. Then laser marker of model NEC SL473D2 was used to mark the wafers for label. To remove the particles produced by laser marking, a standard clean 1 (SC-1) which is the cleaning process of soaking wafers into the solution containing NH_4OH :

$H_2O_2 : H_2O = 1 : 4 : 20$ for 600 seconds at 75 ℃ was performed after laser marking.

2. Pre-furnace standard (STD) clean and dry oxide 10 nm

Before the dry oxidation, the STD clean was performed. The STD clean contains SC-1 and SC-2. A DI water rinse was performed before and after each clean step. SC-2 is the cleaning process of soaking wafers into the solution containing $HCl : H_2O_2 : H_2O = 1 : 1 : 6$ for 600 seconds at 75 ℃. After the STD clean, the dry oxidation to grow a 10-nm-thick SiO_2 pad layer was performed at 925 ℃ by a horizontal furnace system.

3. Pre-furnace STD clean and LPCVD Nitride 80 nm

If this deposition process was subsequent to previous process, the STD clean could be skipped. Otherwise, after the pre-furnace STD clean, a 80-nm-thick LPCVD nitride layer as a masking layer for STI process was formed by a horizontal furnace system.

4. Trench patterning

The lithography process was performed by TEL CLEAN TRACK MK-8 for photo resist (PR) coating and development and the Canon FPA-3000i5+ stepper for exposure. After the lithography process, the 300 nm trench was patterned by TCP 9400SE etcher. The Mattson AspenII Asher was used to remove the PR residue by O_2 plasma when patterning process was completed. It is noticed that dummy patterns were inserted at this step to prevent the dishing problem from the later chemical mechanical polishing (CMP) process.

5. Pre-furnace standard (STD) clean and dry oxide 10 nm

After the pre-furnace STD clean, a 10-nm-thick SiO_2 liner layer was grown at 925 ℃ by a horizontal furnace system to reduce surface damage and interface charges resulting from the trench etching.

6. Pre-furnace STD clean and LPCVD TEOS oxide 600 nm for trench filling

After the pre-furnace STD clean, a 600-nm-thick LPCVD TEOS oxide layer was formed by a horizontal furnace system for trench filling in STI process.

7. Horizontal furnace annealing for LPCVD TEOS oxide layer

After LPCVD TEOS oxide deposition, a 900 ℃, 30 minutes, N_2 annealing was performed to densify the TEOS oxide layer for the purpose of bearing the damage during the CMP process.

8. CMP planarization

It is anticipated that after CMP planarization the top of TEOS would be slightly higher than that of the nitride on the active region, illustrated in Fig.3-3, in order to prevent excess consumption of TEOS oxide during latter steps. The CMP process was performed by Westech model 372M with PS-2515 diluted with DI water in equal proportion as the polishing slurry. The polish pad is IC1000-A2. The process parameters consist of carrier pressure of 4 psi, plate pressure of 1 psi, carrier speed of 42 rpm, plate speed of 40 rpm, and slurry flow rate of 180 mL/min, and the final polishing rate is about 110 nm/min. Fig.3-3(a) shows the cross-sectional SEM image near the edge of active region after the CMP planarization, and Fig.3-3(b) shows the OM image of the top view.

9. Post-STI process

To remove oxynitride on the silicon nitride, the wafers were dipped in diluted HF consisting of HF : DI water = 1 : 50 for 30 seconds at first. Next, the nitride layer was removed by soaking in a 200 ppm solution of Dihydrogen hexafluorosilicate (H_2SiF_6) diluted in Phosphoric acid (H_3PO_4) at 150 ℃, which achieves a better etching rate selectivity between nitride and TEOS oxide. Then, a diluted HF dipping was performed to remove pad oxide, and finally the STI process was accomplished.

10. Pre-furnace standard (STD) clean and dry oxide 10 nm

After the pre-furnace STD clean, a 10-nm-thick sacrificial SiO_2 layer was grown

at 925 ℃ by a horizontal furnace system to consume the damaged surface layer of silicon to reduce defects and interface charges resulting from the CMP process. Also, for the later implantation and dopant activation process, this oxide layer acts as a capping layer to keep dopant from out-diffusion.

11. BF_2 implantation and dopant activation

After implanted by BF_2^+ at 15 keV to a dose of 5×10^{15} cm^{-2}, wafers were performed a 1000 ℃, 5 seconds rapid thermal annealing (RTA) by KORONA RTP 800.

12. PECVD TEOS oxide 40 nm

A 40-nm-thick PECVD TEOS oxide layer was deposited by Oxford 100 PECVD system to avoid breakdown due to leakage path from probing pad to substrate when device is measured.

13. Contact hole patterning

The lithography process was performed by TEL CLEAN TRACK MK-8 for photo resist (PR) coating and development, and the Canon FPA-3000i5+ stepper for exposure. After the lithography process, a total 50-nm-thick oxide was patterned by soaking in diluted buffered oxide etchant (BOE, NH_4F : HF = 6 : 1) solution containing BOE : DI water = 1 : 100 in volume.

14. NiSi silicidation

After ICP clean by Ar plasma at a flow rate of 200 sccm for 50 seconds, a Ni(15 nm)/TiN(15 nm) stack was sputtered by the FSE cluster PVD system. Then, the residual photoresist and metal were lifted-off by sonicating in acetone for 1 minute. After that, a 500 ℃, 30 seconds RTA was performed in N_2 ambient to form nickel silicide. The unreacted Ni and the TiN were selectively removed by SPM solution containing H_2SO_4 : H_2O_2 = 3 : 1 for 10 minutes at 75 ℃. The OM image of the top view of the mTLM structure after silicidation is shown in Fig.3-3(c).

15. Al pad patterning

The lithography process was performed by a mask contact aligner of model Karl-Suss MJB-3. After the lithography process, a 150-nm-thick Al layer was deposited by a thermal evaporation coater of model ULVAC EBX-6D. The lift-off process was performed, and finally the device fabrication was finished by a 400 ℃, 30 minutes N_2 annealing. Fig.3-3(d) shows the OM image of the top view of the final mTLM structure, and Fig.3-3(e) shows that of the final CBKR structure.

3-4 Results and Discussion

This section shows the experimental results and discussion for both the CBKR method and the mTLM method. Besides, some problems encountered during the extraction are also mentioned. In the following subsections, results of the CBKR method are presented in section 3-4-1 at first; then, those of the mTLM method are presented in section 3-4-2. Lastly, discussion and comparison between the two methods are given in section 3-4-3.

3-4-1 CBKR Method

The ρ_{ce} data as a function of A_c with δ = 50 nm, 0.1 μm, and 0.3 μm are presented in Fig.3-4(a), (b), and (c), respectively, and the lowest extractable ρ_{ce} value is also marked for each test structure with different A_c. Each datum is the average of two extracted results with different forced current directions, illustrated in Fig.3-5. It could be approximately observed that the ρ_{ce} increases with the A_c, which is consistent with the argument mentioned in the previous chapter. As for different δ values, there is no apparent trend for the changes of the ρ_{ce}. It should be reminded that according to the simulation results in previous section 2-5-1, for smaller A_c such as 50×50 nm^2, the

δ has a less influence on the ρ_c extraction using a CBKR structure. However, since the test structures with smaller A_c are hard to be fabricated in this work, the less δ dependence could not be observed. The reason that there is no difference between data with different δ values could be that some other parameters dominate and even limit the extraction accuracy.

Then, issues for the CBKR structure such as the corner-rounded contact hole, and the recessed contact interface mentioned in section 2-5-2 should be also taken into consideration. The corner-rounding would cause a larger ρ_{ce}, but in this work its influence may be slight because of the relatively larger A_c compared to the area lost by the round corner. As for the recessed contact, referring to Fig.2-11 using the CBKR structure with $\delta = 0$, a half loss of the ρ_{ce} could be observed. Considering $\delta \neq 0$ for the real case, the impact of the recession would be intensified since basically the actual contact area increases, indicating that the decrease of the ρ_{ce} would be much larger than the increase of the ρ_{ce} caused by the δ. Briefly, for the CBKR test structures, the ρ_{ce} extraction suffers from parasitic resistances as the ρ_c decreases. Then considering $\delta \neq 0$, the ρ_{ce} would be overestimated. Moreover, because of the recessed contact resulting from the silicidation, the ρ_{ce} would decrease. It could be noticed that the recession is supposed to affect the ρ_{ce} extraction most. However, it would be still challenging to distinguish the explicit contribution to the ρ_{ce} of each factor in real case.

3-4-2 mTLM Method

According to the mTLM extraction procedure, the R_f should be obtained first, and then the ρ_{ce} could be extracted from the R_f-$1/W_c$ plot. To extrapolate the R_f, the R_{total}-L_c plot is necessary and shown in Fig.3-6 and Fig.3-7. In Fig.3-6 with W_c = 1 μm and L_c = 2 μm, the extrapolated R_f value could range from -46 to 106 Ω if

different group of devices is chosen due to process variation. In addition to the uncertainty of the extrapolated R_f value, the unreasonable negative R_f is also likely to be observed. Intrinsically the extrapolation method could be one reason for the inaccurate R_f [34,40,41]; moreover, the condition that the R_s is considerably higher than the R_f would intensify the R_s variation dependence on the R_f and deviate the extrapolated results, i.e., the error of the R_s could play a major role during the extrapolation instead of the R_f if the R_s is relative larger enough than the R_f, which is consistent with the simulation results mentioned in the previous chapter and the literature [34]. Fig.3-7(a) gives the mean value of the R_{total} for each L_d, and the linear relationship between R_{total} and L_d could be seen consequently. Hence, it is noted that basically the mTLM method suffers from both the process variation and the intrinsic error by using the extrapolation method; however, by means of the law of large numbers in probability theory mentioned in previous chapter, average of sufficient experimental data could diminish the inaccuracy and correct the extrapolation, which is a feasible way to realize the mTLM method.

Next, in order to extract the ρ_{ce} from the R_f-$1/W_c$ plot, the R_f values extrapolated with W_c = 1.5 μm and 2 μm are obtained and shown in Fig.3-7(b) and Fig.3-7(c), respectively. The R_f-$1/W_c$ plot is illustrated in Fig.3-8(a), whose slope gives the ρ_{ce}, and the $\rho_{ce} = 2.9\times10^{-7}$ Ω-cm^2 for L_c = 2 μm consequently. Similarly, following the above procedure, the $\rho_{ce} = 9.8\times10^{-7}$ Ω-cm^2 for L_c = 1 μm is also extracted and shown in Fig.3-8(b).

For the mTLM method, issues mentioned in section 2-5-4 are also discussed in this section. First of all, the process dependence on the ρ_{ce} extraction is obvious. It could be observed that the ρ_{ce} of L_c = 1 μm is different from that of L_c = 2 μm by about two times; however, this noticeable difference between L_c = 1 μm or 2 μm for ρ_c in the range of 10^{-7} Ω-cm^2 should not exist according to the simulation results

remarked in Fig.2-13 in section 2-5-3. This implied that the process variation truly exists and makes a little difference to each test structures even though test structures are fabricated in accordance with an identical process flow. The dispersive data shown in Fig.3-6 could confirm the influence of the process variation. Comparing with the simulation results in Fig.2-16(d), the process dependence could vary the ρ_{ce} in a much wider range, 10^{-3} to 20 times for instance, and therefore leads the extraction to be worthless. Fortunately, after averaging R_{total} values for each L_c, the dependence of the process variation could be lessened, and therefore the extraction results of the mTLM method would be more trustworthy. As for the recessed contact, it was expected that the ρ_{ce} would increase with the recession depth in a few times, illustrated in Fig.2-19(a) and explained in section 2-5-4. As the process dependence is significant, the influence of the recession may not be observed in this work; while the process dependence is diminished by averaging the data, the influence of the recession would emerge. It is supposed that the process dependence is reduced since the average R_{total} and the L_c is in a linear relationship shown in Fig.3-7. Hence, the impact of the recessed contact would appear, resulting in an overestimate of the ρ_{ce}. Moreover, since the extraction would be more accurate with larger L_c, it could be inferred that the true ρ_c would be lower than 2.9×10^{-7} Ω-cm^2.

The R_s could be also extracted by the mTLM method, and the extracted R_s is 158.1 Ω/□ with L_c = 1 μm and 157.1 Ω/□ with L_c = 2 μm. Compared with the R_s = 140.6 Ω/□ measured by the four-terminal structure, since both methods are sensitive to the pattern distortion after the lithography, their results seems to be compatible.

To inspect the cross-sectional contact region of test structures, TEM was performed and the micrograph is shown in Fig.3-9. It could be observed that the NiSi layer is smaller than the actual contact size, and some unexpected voids appear between the NiSi layer. Also, there is an additional thin interlayer between NiSi and Pt

layers, which could be attributed to the wet etching process with the SPM solution for the unreacted metal removal [70]. In this process flow, a one-step annealing for silicidation was used, and hence two phases, Ni_2Si and NiSi, would appear at the contact. After the selective etching with the SPM solution was performed, the follow-up DHF dipping may remove the interlayer partially and resulted in some gaps. The last sintering step is supposed to make the Ni_2Si transformed into the NiSi, and the excess Ni would tend to outdiffuse to the Pt layer through the gaps [71,72]. Consequently, the voids were left. Briefly, a smaller actual A_c is caused by the loss of the NiSi layer, and if the contact size could be correct, the ρ_{ce} could be lower for both CBKR and mTLM methods.

3-4-3 Comparison and Discussion

Because the test structures of the CBKR and the mTLM method are fabricated in an identical process flow, it is reasonable to compare the experimental results of the two methods with each other. Since the CBKR method suffers from the parasitic resistance which seems incapable of elimination, the extraction results would include the effects of several factors like the δ and the recession, and therefore would be complicated. By contrast, as for the mTLM method, although the process variation plays an important role in the ρ_{ce} extraction, it could be avoided by averaging sufficient extraction data. Thus, the recession would be the major part to determinate the ρ_{ce} extraction, which is relatively easier to analyze than that of the CBKR method.

According to the argument that the true ρ_c would be lower than 2.9×10^{-7} Ω-cm^2 mentioned in the previous section, the ρ_{ce} extracted by the CBKR method could be discussed. For larger A_c, the influence of the δ is more obvious than that of the recession, while for smaller A_c, the influences of both the δ and the recession could be compatible, but it is still unable to tell which one has a stronger influence.

To sum up, the CBKR method provides an easier way to extract the ρ_c; nevertheless, it could only give a roughly estimation since there are some non-ideal factors, whose contribution to the ρ_{ce} are still not clear, affecting the ρ_{ce}. On the other hand, the mTLM extraction procedure is multi-steps and complicated. One critical problem of the mTLM method is its sensitivity to the process variation. By using sufficient extracted data, the error could be lessened. Therefore the influence of the recessed contact could be distinguished from the ρ_{ce}. Although the recession dependence upon the ρ_{ce} is still complicated, the simulation results may give a reference to determine the true ρ_c.

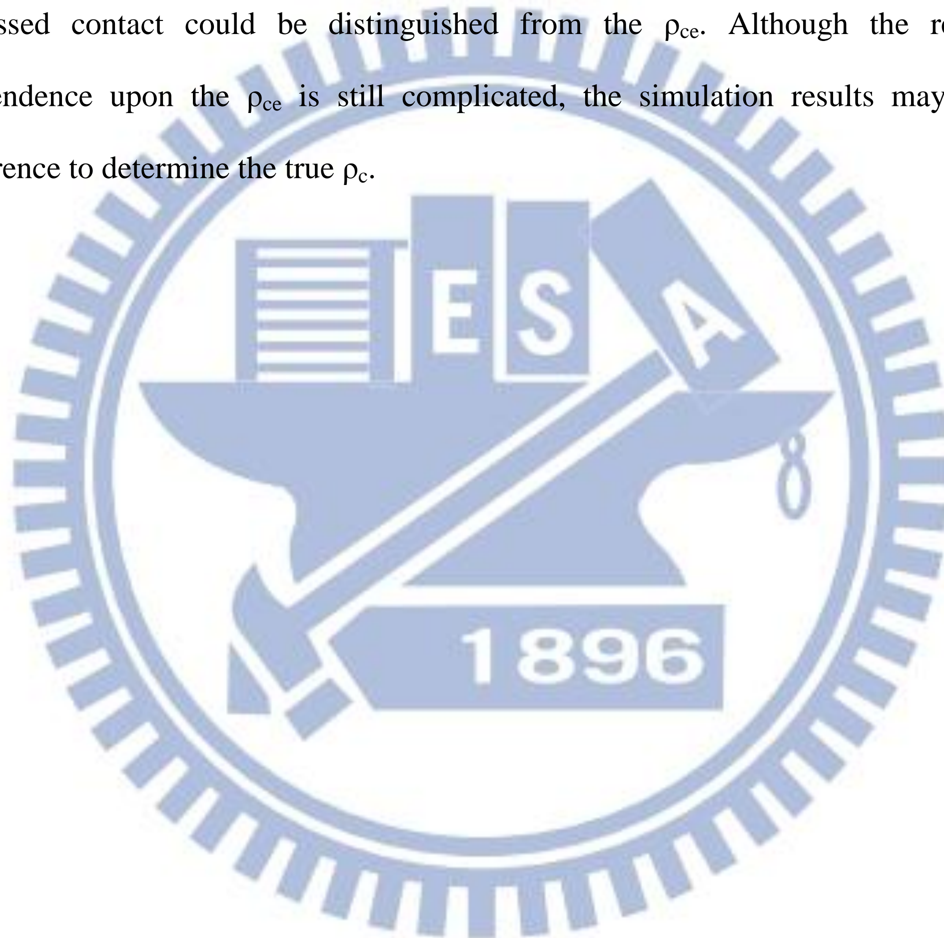

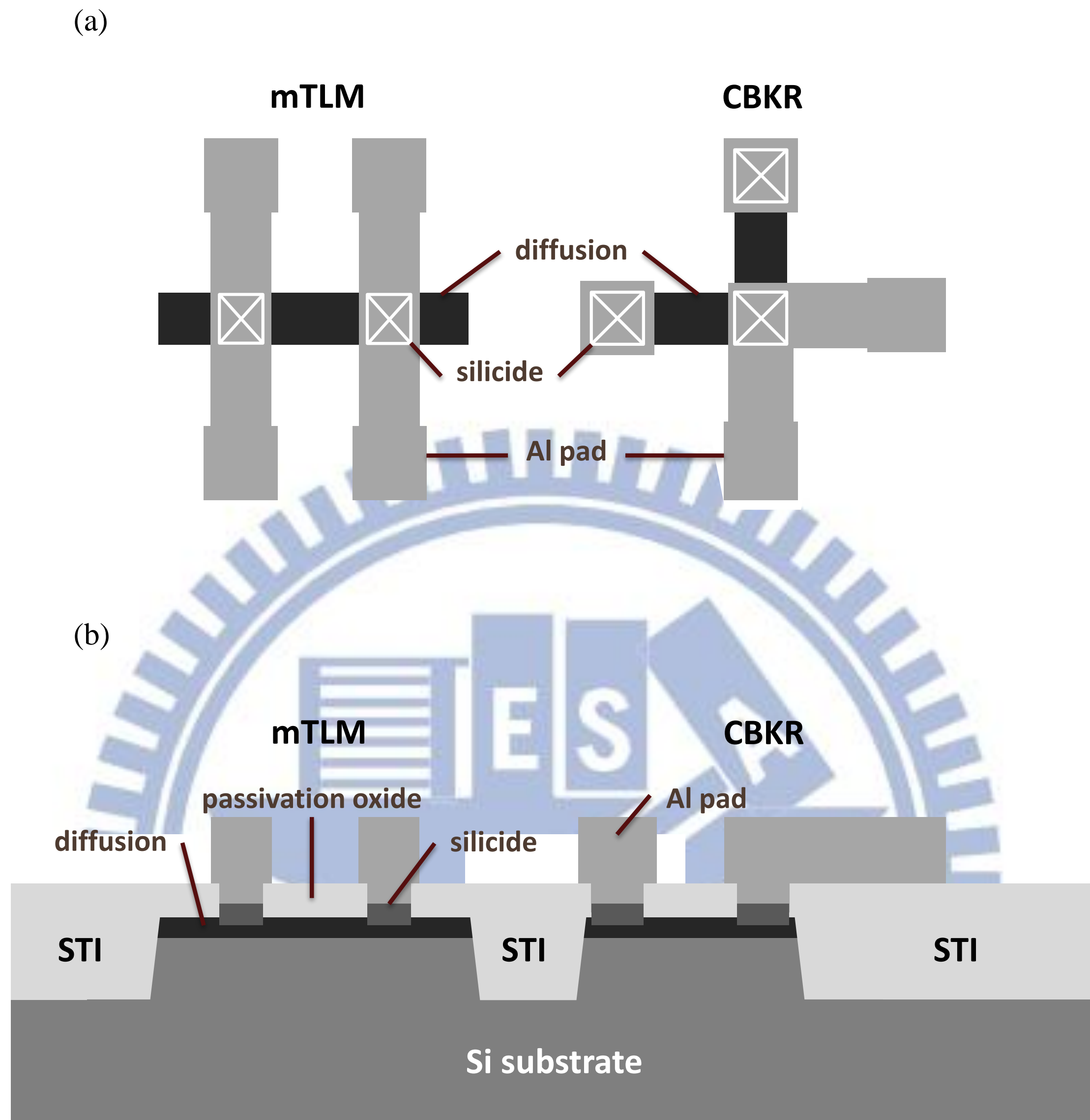

Fig. 3-1(a) Schematic layout of test structures. (b) Schematic cross-section of test structures. Left: the mTLM method. Right: the CBKR method.

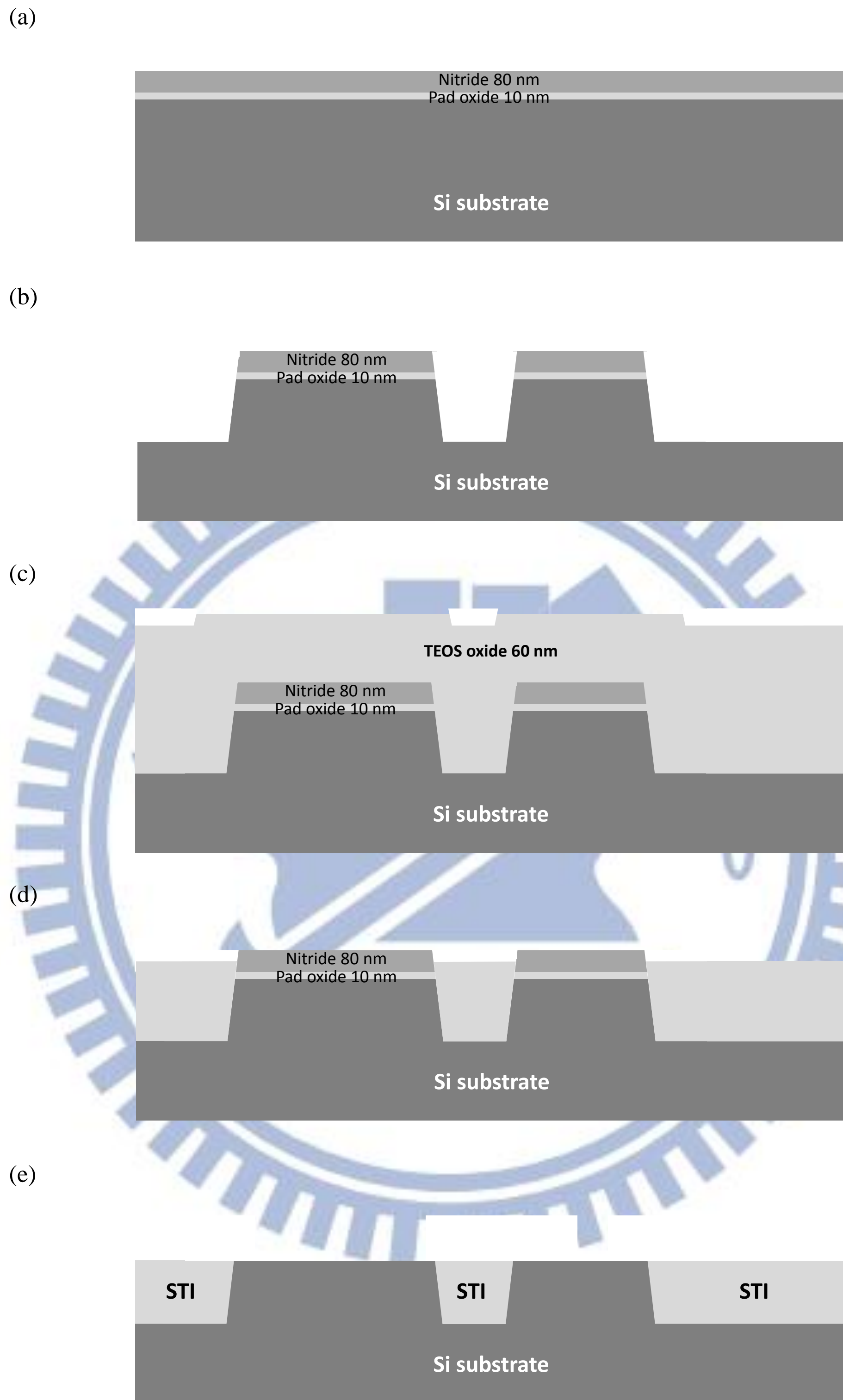

Fig. 3-2 Process flow of test structures. (a) Pad oxide growth and nitride deposition. (b) Trench etching. (c) PECVD TEOS oxide deposition for trench filling. (d) CMP process. (e) Post-field oxidation process to finish STI.

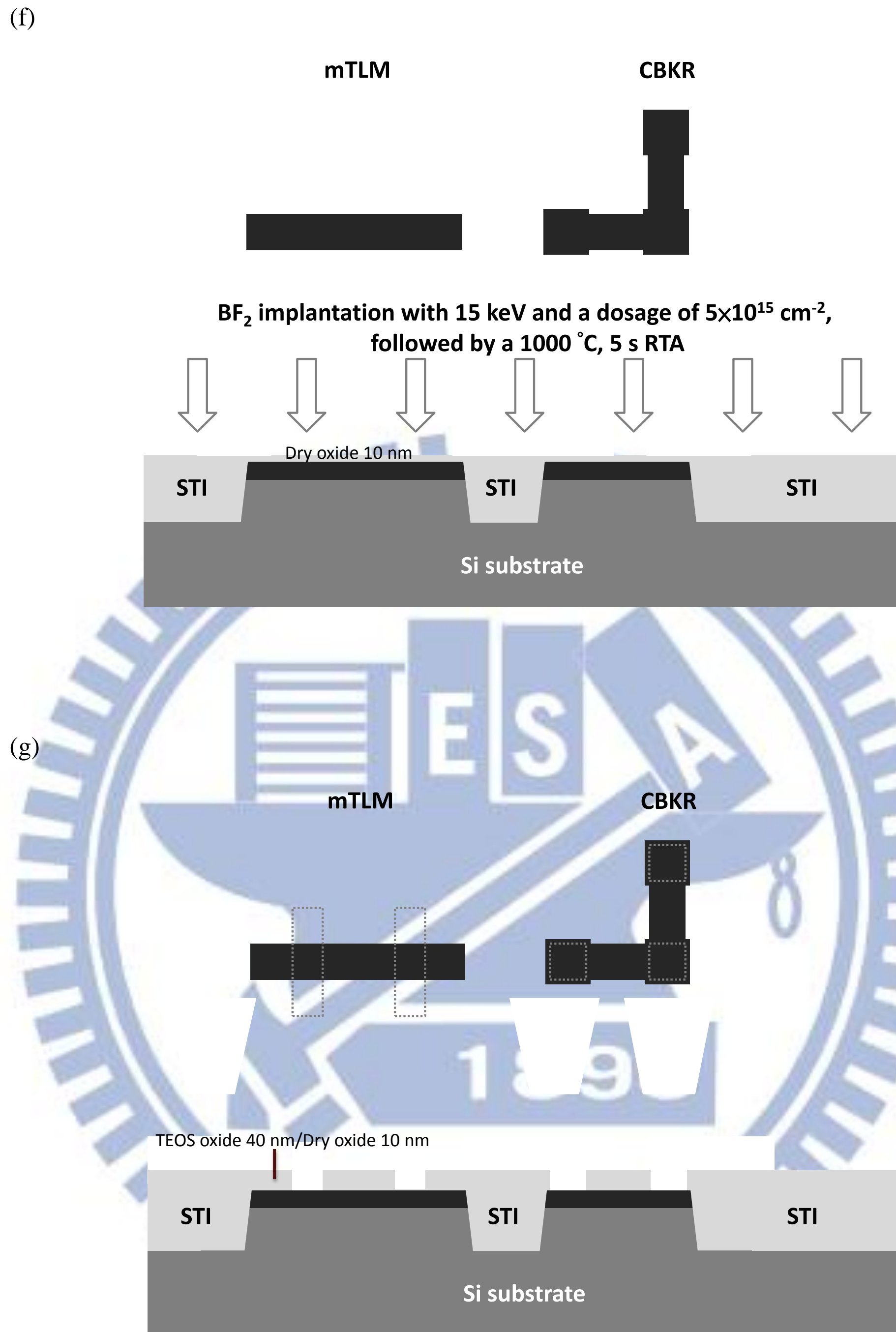

Fig. 3-2 Process flow of test structures. (f) BF_2 implantation and dopant activation. (g) Passivation oxide deposition and contact hole patterning.

(h)

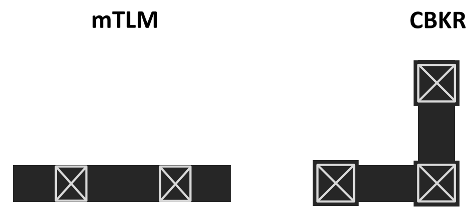

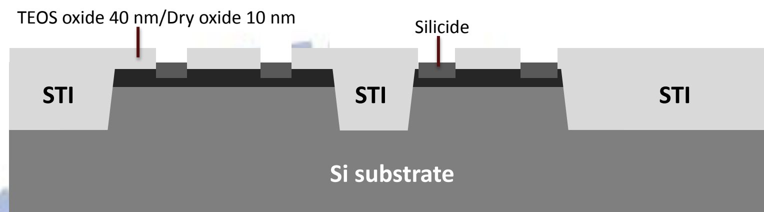

(i)

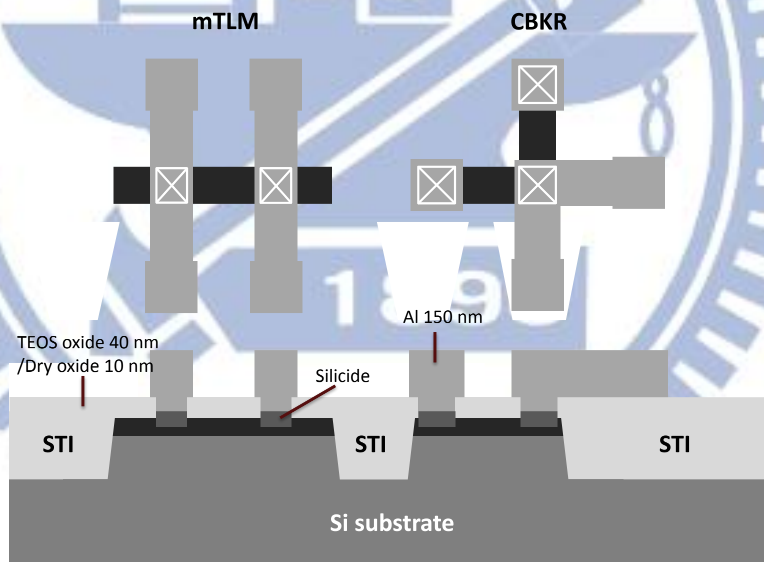

Fig. 3-2 Process flow of test structures. (h) NiSi silicidation. (i) Al pad patterning and Al sintering.

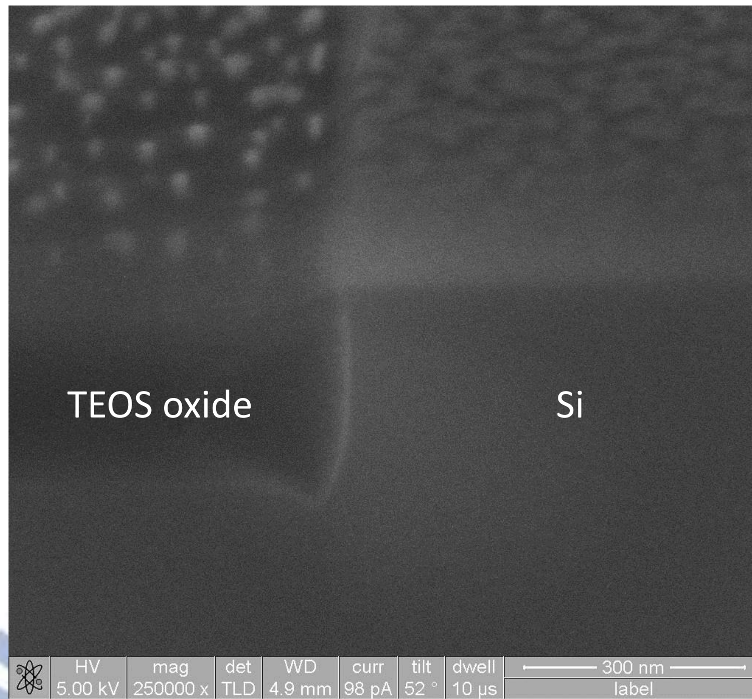

Fig. 3-3(a) SEM image of the edge between STI and active region after CMP process.

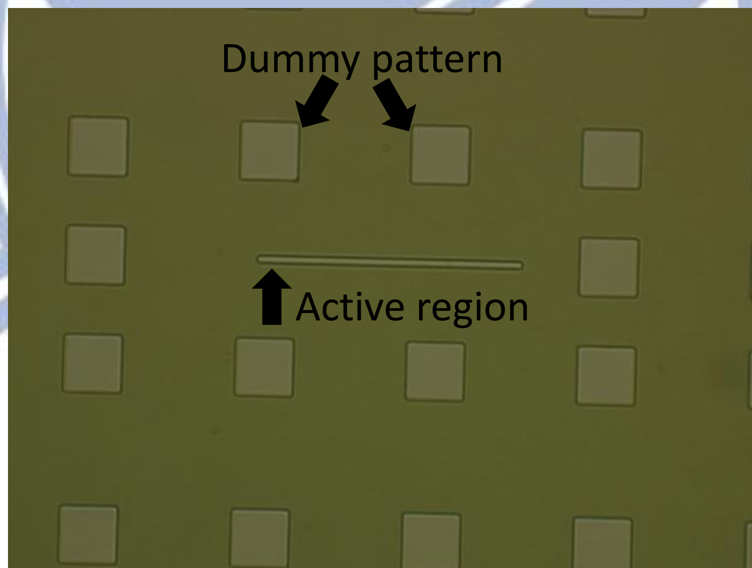

Fig. 3-3(b) OM image of the top view of the active region and dummy patterns after CMP process. The magnification is 1000x.

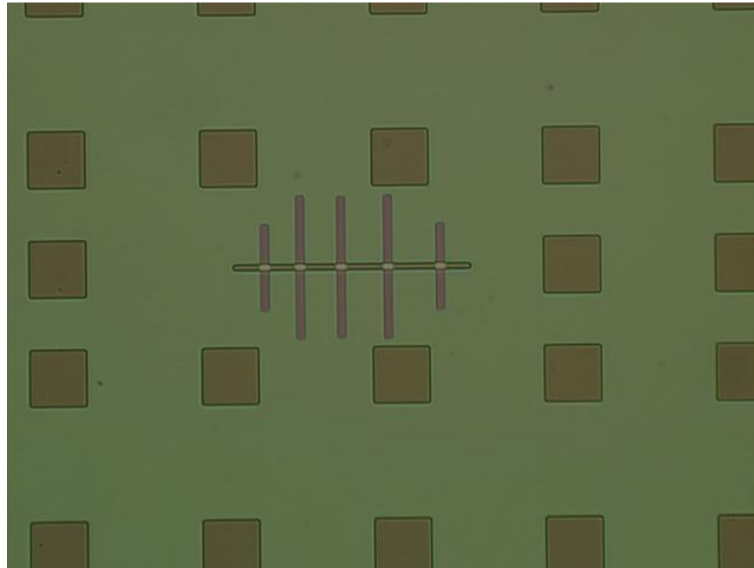

Fig. 3-3(c) OM image of the top view of the mTLM structure after silicidation process. The magnification is 1000x.

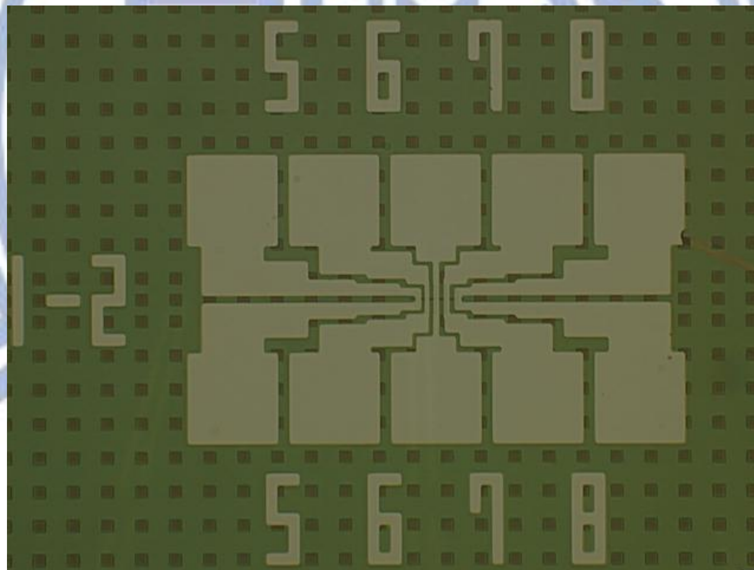

Fig. 3-3(d) OM image of the top view of the final mTLM structure. The magnification is 250x.

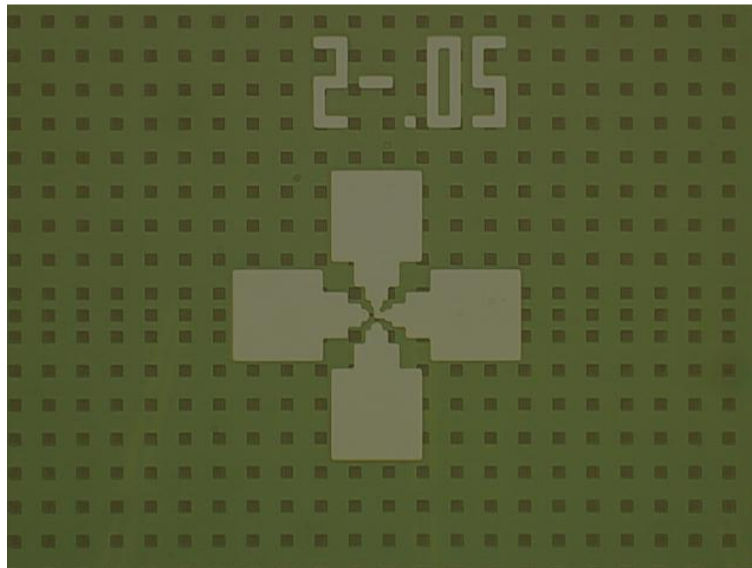

Fig. 3-3(e) OM image of the top view of the final CBKR structure. The magnification is 250x.

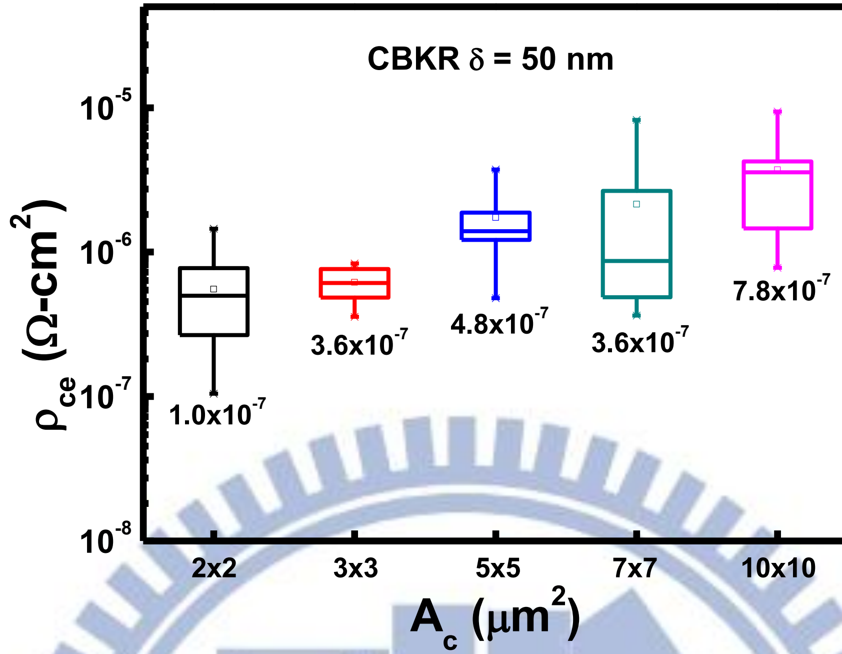

Fig. 3-4(a) The ρ_{ce} versus the A_c using the CBKR method with δ = 50 nm. The lowest extractable ρ_{ce} value is marked for each test structure with different A_c.

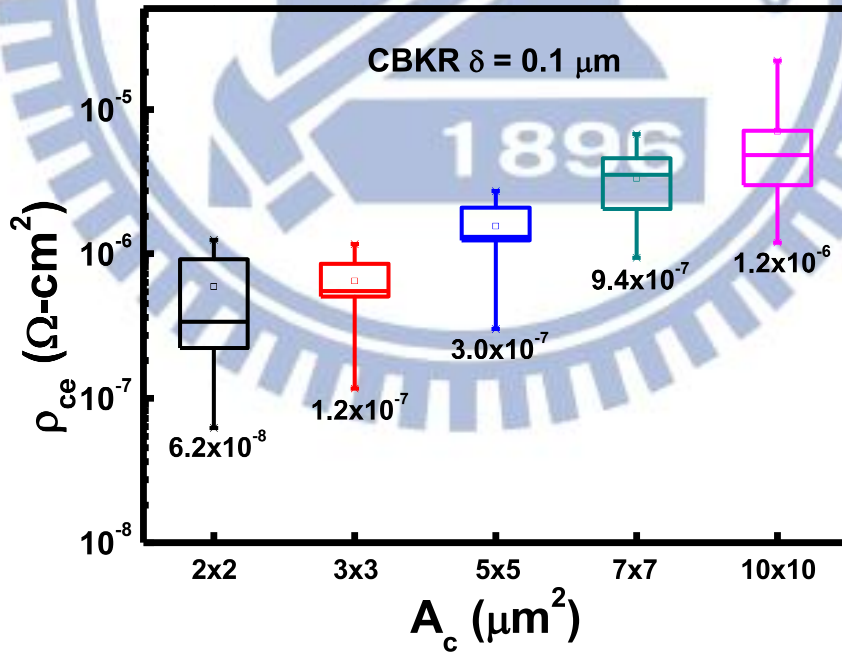

Fig. 3-4(b) The ρ_{ce} versus the A_c using the CBKR method with δ = 0.1 μm. The lowest extractable ρ_{ce} value is marked for each test structure with different A_c.

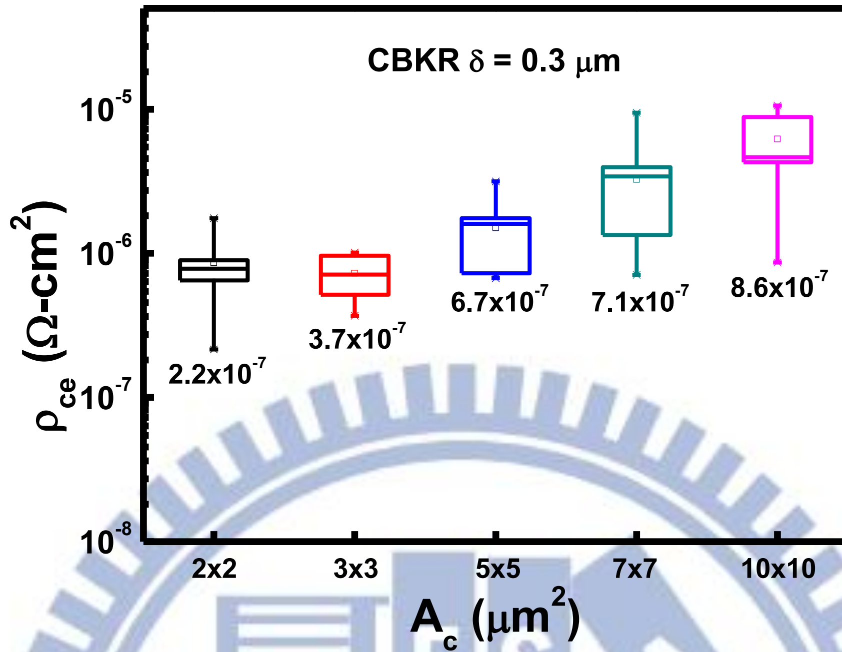

Fig. 3-4(c) The ρ_{ce} versus the A_c using the CBKR method with $\delta = 0.3$ μm. The lowest extractable ρ_{ce} value is marked for each test structure with different A_c.

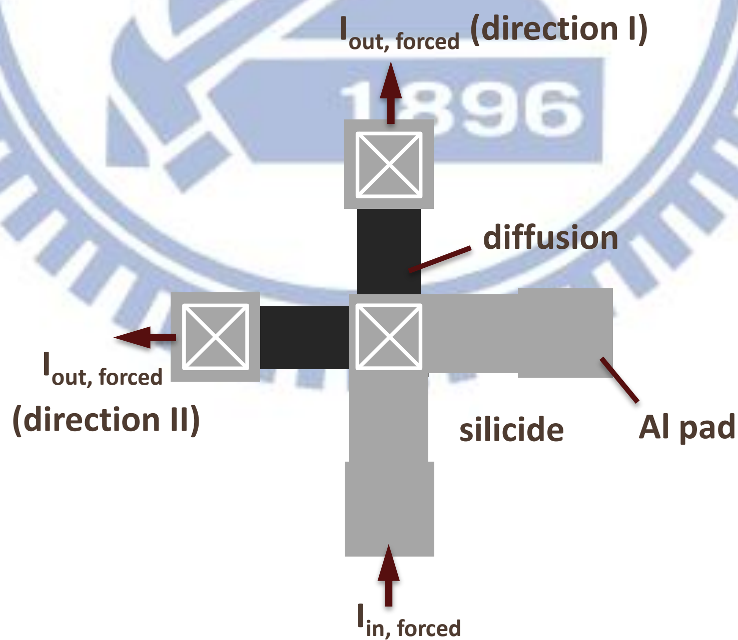

Fig. 3-5 Illustration of two different forced current directions used in the CBKR extraction.

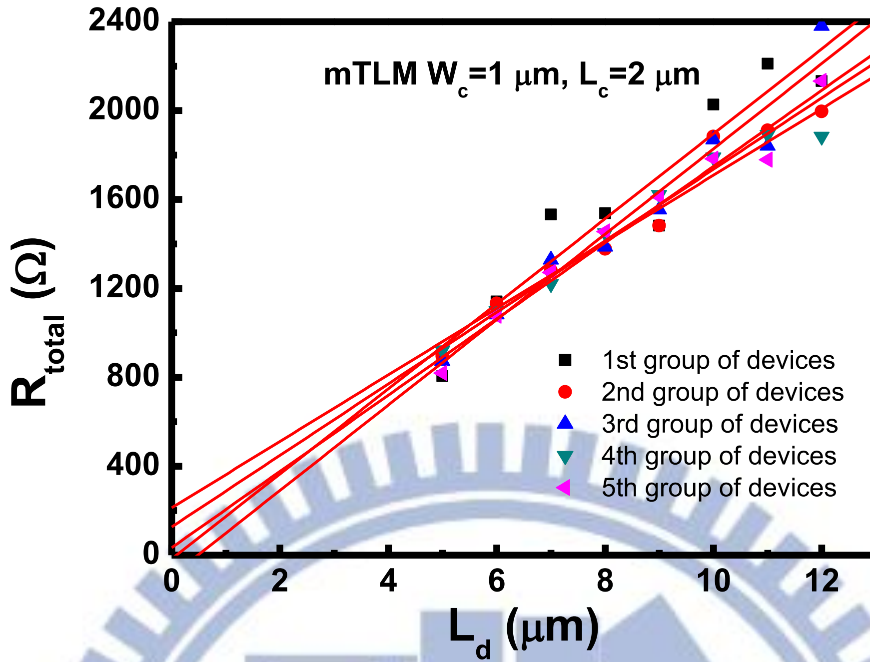

Fig. 3-6 Illustration of the R_f extrapolation from different groups of devices using the mTLM method with W_c = 1 μm and L_c = 2 μm.

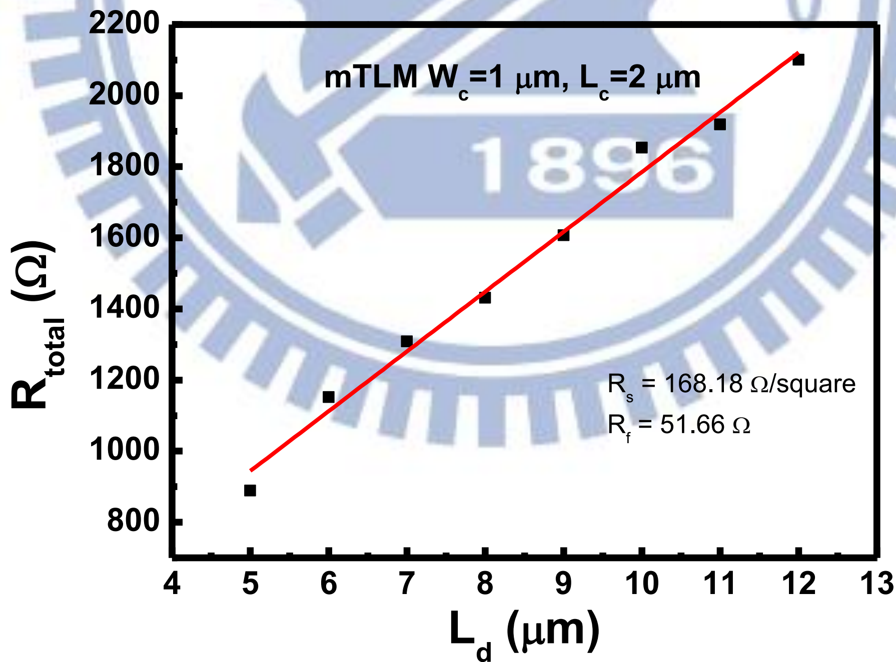

Fig. 3-7(a) R_f extrapolation after averaging R_{total} values for each L_d using the mTLM method with W_c = 1 μm and L_c = 2 μm.

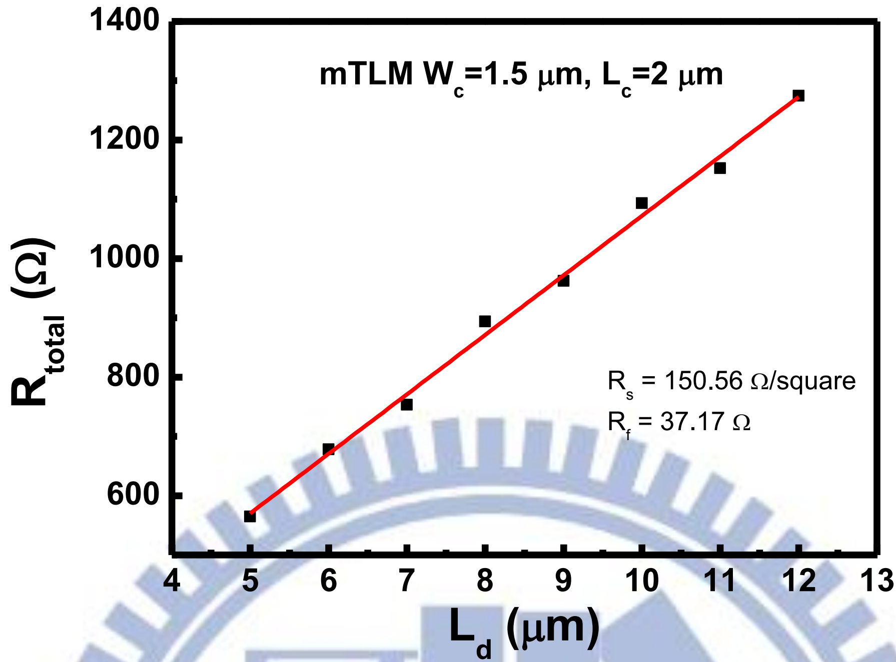

Fig. 3-7(b) R_f extrapolation after averaging R_{total} values for each L_d using the mTLM method with W_c = 1.5 μm and L_c = 2 μm.

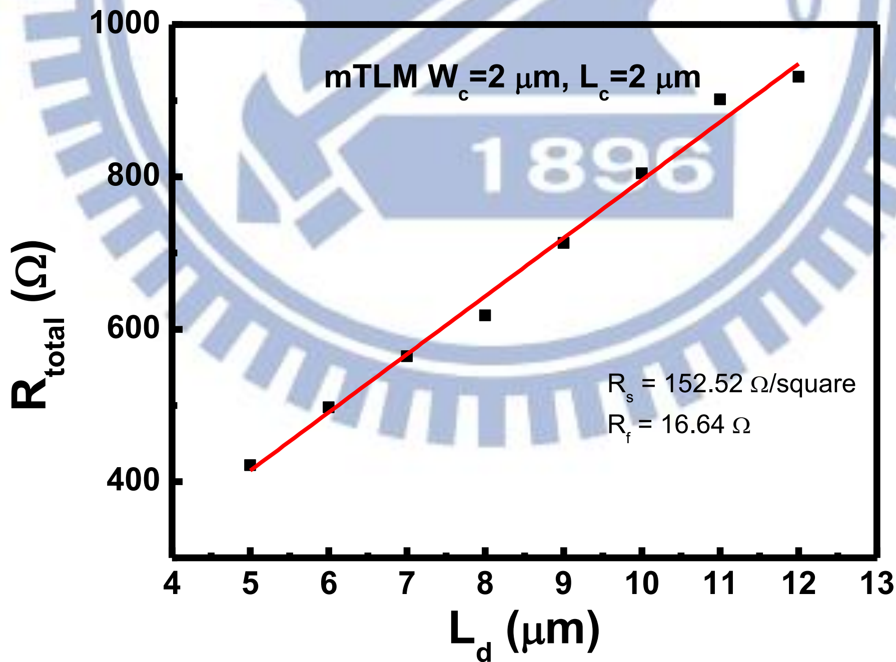

Fig. 3-7(c) R_f extrapolation after averaging R_{total} values for each L_d using the mTLM method with W_c = 2 μm and L_c = 2 μm.

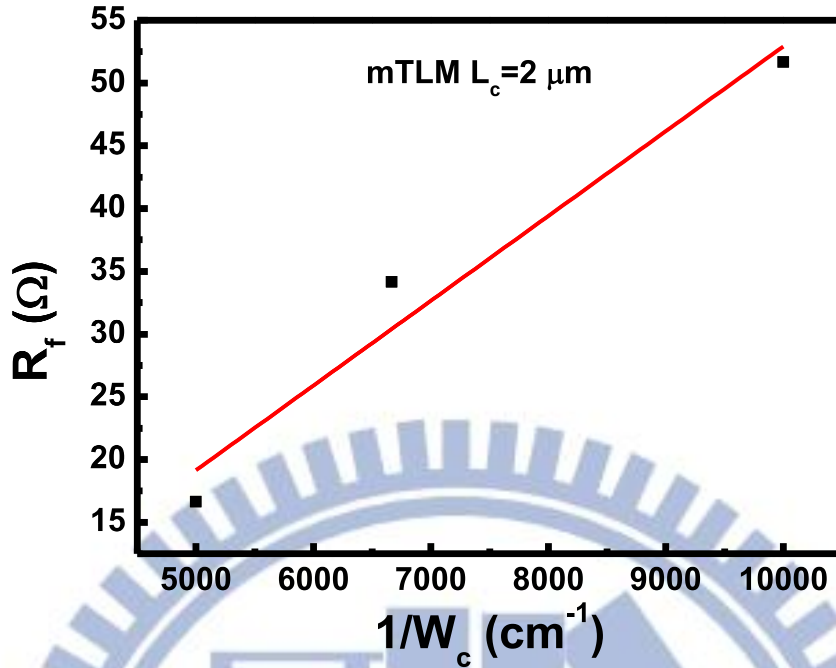

Fig. 3-8(a) The $\rho_{ce} = 2.9\times10^{-7}$ Ω-cm^2 is extracted using the mTLM method with $L_c = 2$ μm.

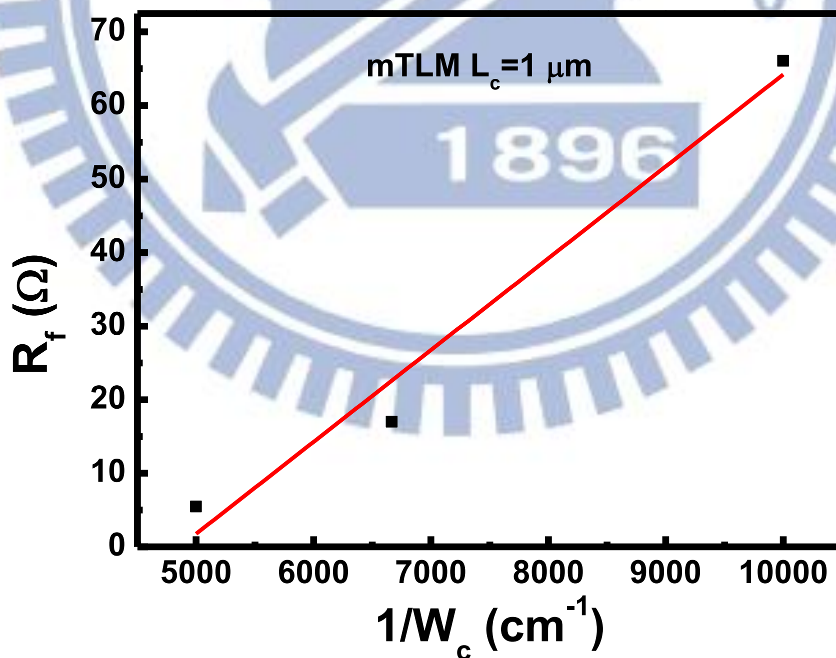

Fig. 3-8(b) The $\rho_{ce} = 9.8\times10^{-7}$ Ω-cm^2 is extracted using the mTLM method with $L_c =$ 1 μm.

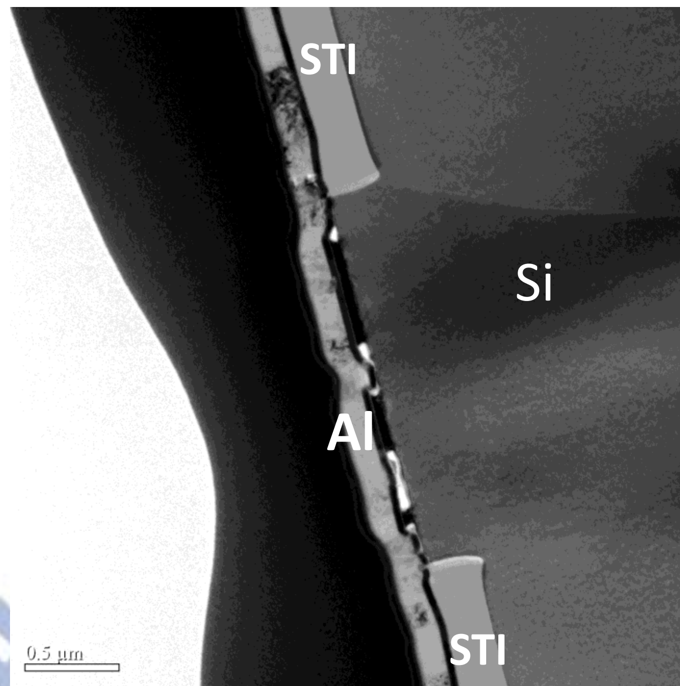

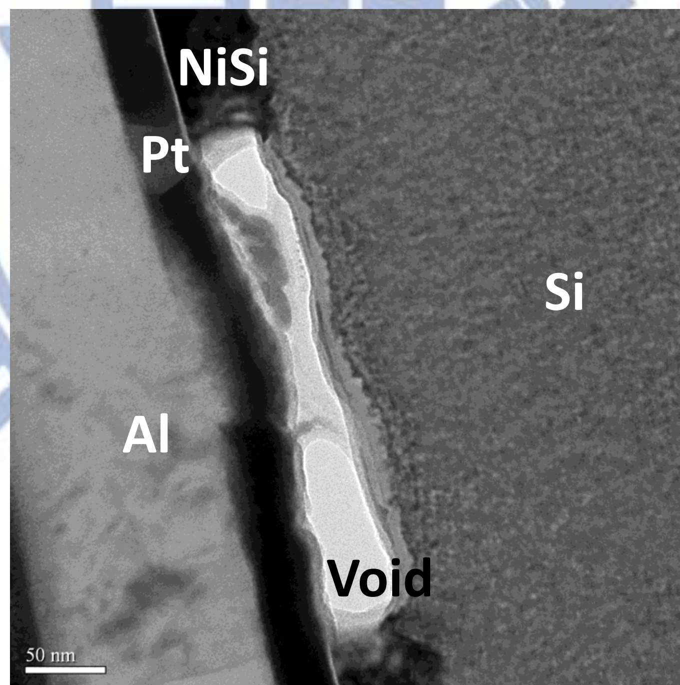

Fig. 3-9 TEM images of NiSi/Si contact. Some unexpected voids between the NiSi layer were observed, and thus the actual A_c should be smaller than the designed size.

Chapter 4
Summary and Future Work

4-1 Summary

This thesis studies the ρ_c extraction of the CBKR and mTLM methods by both simulation and experiment. 3-D simulation of device characteristics was performed to evaluate the extraction accuracy of the ρ_c, and several parameters were discussed. Then, test structures were realized by using the STI process, and the experimental data were shown and compared with the simulation.

First, 3-D simulation is employed. For the CBKR method, the accuracy of the ρ_c extraction could be enhanced by scaling down the dimensions of the test structures, while would be degraded due to the process limitation. Several parameters are investigated: the contact size (A_c), the process tolerance (δ), the corner-rounded contact hole, and the recessed contact interface. As the A_c decreases, the parasitic resistance (R_p) decreases, and hence the extraction accuracy increases. It is noticed that only 10 % error exists as $\rho_c = 1\times10^{-8}$ Ω-cm^2 as the A_c reduces to 10 nm$\times$10 nm. The δ has less influence on the extraction accuracy, which is different from the fact presented in 2-D simulation, since the relative smaller contact area makes the parasitic resistance have no influence on the parasitic term in the ρ_{ce}. Besides, as the A_c is shrunk, it is expected that corner rounding would affect the accuracy of the ρ_c extraction. The influence of corner rounding is investigated by using circular contacts, and it is observed that corner rounding makes a large difference, i.e., increasing 30% error, to the ρ_c extraction, which means that the CBKR method would become erroneous as the contact areas decrease. The recessed contact is another issue. The ρ_{ce}

would decrease with the recession depth for higher ρ_c, while would increase for lower ρ_c. Also, the A_c dependence is observed in the recessed contact cases. As the A_c reduces, the recession has more influence on extracting the ρ_c, which means that the recessed contact would become more critical to the ρ_c extraction as devices scale down.

Next, the mTLM method is also analyzed by simulation. The dimensions of test structures is designed and optimized at first. Then the extraction accuracy of the mTLM method is compared with that of the CBKR method. Moreover, several parameters are discussed. Since the mTLM method is designed for a self-aligned process, it would be immune from the δ and the corner-rounding contact. In addition, due to its sensitivity to the process, the variation of the dopant concentration in semiconductors and the variation of the tapered sidewall angle of the active region were both analyzed by statistic. The recessed contact was also investigated. In this thesis, with a micro-process and L_c = 2 μm the mTLM structures could provide an accurate ρ_c extraction, and the extraction error is only few percent. Compared with the CBKR structure with $A_c = 50\times50$ nm^2, the mTLM method shows a better accuracy at lower ρ_c regime, because the requirement of a larger ratio of L_c and L_T would be reached as lower ρ_c and thus an accurate extraction would be achieved for the mTLM method. Then, this thesis studied the dependence on the variation of the dopant concentration and the variation of tapered sidewall angles of the active region according to the statistic. It is observed that there is a strong dependence on the variation of the dopant concentration, i.e., the ρ_{ce} would vary four orders of magnitude when the surface concentration has only 5 % variation. On the other hand, there is a relative slight dependence on the variation of tapered sidewall angles of the active region, which shows 50 % variation when a 2 % variation exists for the tapered sidewall angle. Finally, as the recessed contact is considered, the ρ_c is overestimated

with higher ρ_c because the current tends to flow into the bottom contact, but underestimated with lower ρ_c because the side contact dominated the current flow and hence the ρ_c extraction.

Then, test structures of the CBKR and the mTLM methods were fabricated in an identical process flow and then their extraction results were discussed with the simulation. In order to define the active region explicitly, shallow trench isolation (STI) is utilized. The CBKR method is easier to extract the ρ_c, but the parasitic resistance is about to result in inevitable extraction error. It could be observed that the noticeable A_c dependence that the ρ_{ce} would increase with the A_c and the less δ dependence is shown in this thesis, which is consistent with the simulation results. The lowest ρ_{ce} obtained by the CBKR method is 6.2×10^{-8} Ω-cm^2. As for the mTLM method, the primitive data were disordered. However, for the mTLM method, its sensitivity to the process variation could be reduced and its extraction accuracy could be enhanced by means of averaging data according to the statistic. The ρ_{ce} obtained by the mTLM method are 2.9×10^{-7} Ω-cm^2 with L_c = 2 μm, and 9.8×10^{-7} Ω-cm^2 with L_c = 1 μm. Unfortunately, for both methods, the recessed contact interface would exist and affect the ρ_{ce}. Thus, it is difficult to quantify its influence since not only its contribution to the ρ_{ce} is complicated contribution but also there are too many parameters affect the extraction as well.

In conclusion, this thesis discussed the CBKR and the mTLM method to extract the ρ_c by simulation and experiment. The CBKR structure with a smaller contact area due to the devices scale down would obtain more accurate results in theory, while the parasitic resistance would still limit the accuracy. On the other hand, the self-aligned mTLM structure proposed in this thesis is realized by using the STI process. Its sensitivity to the process variation could be diminished by averaging data. Therefore, the TLM method could be more accurate and is promising for ρ_c extraction.

Nevertheless, too many parameters would affect the ρ_c extraction, and within those factors, the recessed contact interface would cause a complicated ρ_c extraction for both the CBKR and mTLM methods. It would still be a critical issue to the accuracy of the ρ_c extraction.

4-2 Future Work

In real case, design and process parameters would affect the ρ_c extraction simultaneously, which leads to the ρ_c extraction more complex. In our simulation, parameters are discussed separately to reveal their contribution respectively, while they may be dependent on each other. Therefore, taking parameters into consideration at the same time would complete the analysis of the ρ_c extraction. Besides, among these parameters mentioned in this thesis, the recession shows a more complex influence on the ρ_c extraction. Since the recession is still needed to analyze, a better description of the relationship between the recession and the ρ_c would be expected and necessary. Moreover, for smaller A_c, the thickness of NiSi for each contact hole could be different, resulting in the variation of the recession depth. This situation should be also taken into consideration.

As for the devices fabrication, the mTLM method needs to average large amounts of experimental data to diminish the error from the process variation. Hence, sufficient measurable test structures are necessary and would result in better extraction accuracy. In addition, the fabricated test structures could be improved. In the TEM images shown in Fig.3-9, the silicide area was smaller than the contact hole. Although the ρ_{ce} could still be extracted, the actual A_c for the CBKR method and the actual W_c for the mTLM method were smaller than the design size. Therefore, better extraction accuracy could be obtained by improving the test structures through

fabrication.

Last, by this thesis, it is observed that the accurate low ρ_c extraction encounters great challenge for both CBKR and mTLM methods. Due to the strong requirement of the accuracy of the ρ_c extraction, novel test structure and extraction procedure are still critical issue.

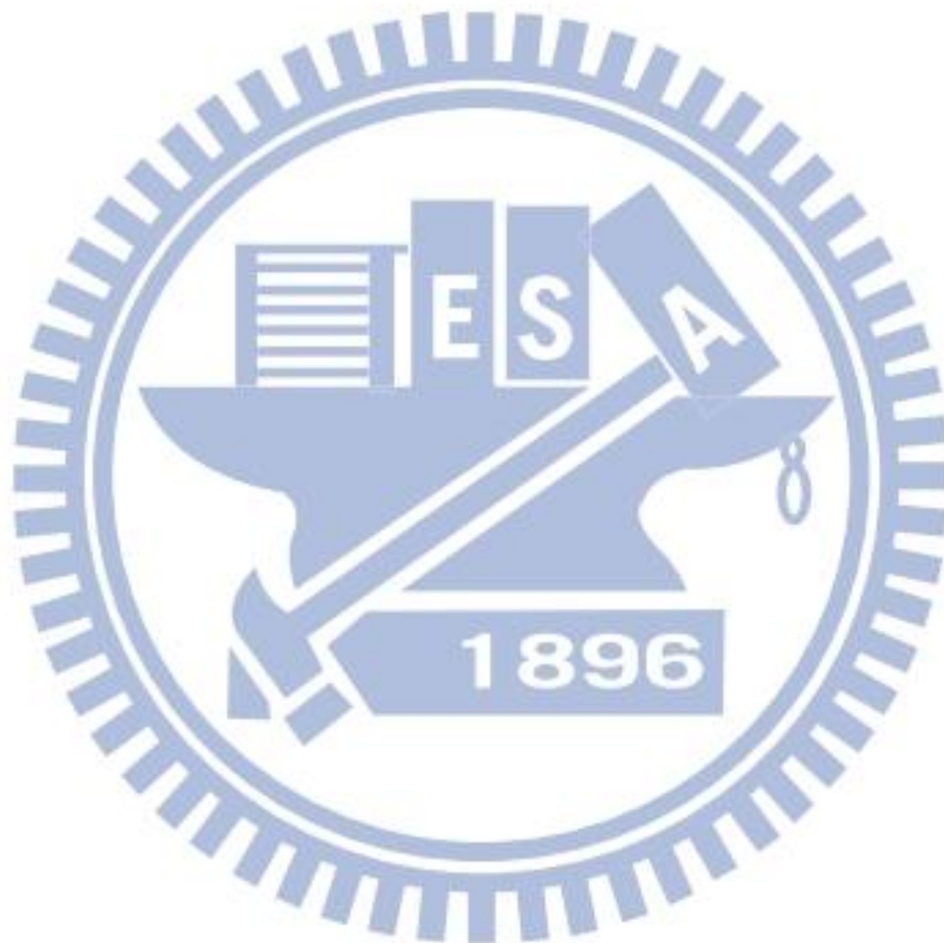

References

[1]. Y. Taur, C. H. Wann, and D. J. Frank, “25 nm CMOS design considerations,” in *IEDM Tech. Dig.*, 1998, pp. 789–792.

[2]. J. D. Plummer and P. B. Griffin, “Material and process limits in silicon VLSI technology,” *Proc. IEEE*, vol. 89, pp. 240–258, 2001.

[3]. S. D. Kim, C.-M. Park, and J. C. S.Woo, “Advanced model and analysis for series resistance in sub-100 nm CMOS including poly depletion and overlap doping gradient effect,” in *IEDM Tech. Dig.*, 2000, pp. 723–726.

[4]. K. J. Kuhn, “Considerations for ultimate CMOS scaling,” *IEEE Trans. Electron Devices*, vol. 59, pp. 1813–1828, 2012.

[5]. T. Ohmi, A. Teramoto, R. Kuroda, and N. Miyamoto, “Revolutional progress of silicon technologies exhibiting very high speed performance over a 50-GHz clock rate,” *IEEE Trans. Electron Devices*, vol. 54, pp. 1471–1477, 2007.

[6]. K. Mistry, C. Allen, C. Auth, B. Beattie, D. Bergstrom, M. Bost, M. Brazier, M. Buehler, A. Cappellani, R. Chau, C.-H. Choi, G. Ding, K. Fischer, T. Ghani, R. Grover, W. Han, D. Hanken, M. Hattendorf, J. He, J. Hicks, R. Huessner, D. Ingerly, P. Jain, R. James, L. Jong, S. Joshi, C. Kenyon, K. Kuhn, K. Lee, H. Liu, J. Maiz, B. Mclntyre, P. Moon, J. Neirynck, S. Pae, C. Parker, D. Parsons, C. Prasad, L. Pipes, M. Prince, P. Ranade, T. Reynolds, J. Sandford, L. Shifren, J. Sebastian, J. Seiple, D. Simon, S. Sivakumar, P. Smith, C. Thomas, T. Troeger, P. Vandervoorn, S. Williams, and K. Zawadzki, “A 45 nm logic technology with high-k + metal gate transistors, strained silicon, 9 Cu interconnect layers, 193 nm dry patterning, and 100% Pb-free packaging,” in *IEDM Tech. Dig.*, 2007, pp. 247–250.

[7]. S. D. Kim, C.-M. Park, and J. C. S. Woo, “Advanced model and analysis of series resistance for CMOS scaling into nanometer regime—Part I: Theoretical derivation,” *IEEE Trans. Electron Devices*, vol. 49, pp. 457–466, 2002.

[8]. C. M. Osburn and K. R. Bellur, "Low parasitic resistance contacts for scaled ULSI devices," *Thin Solid Films*, vol. 332, pp. 428–436, 1998.

[9]. S. D. Kim, C.-M. Park, and J. C. S. Woo, “Advanced model and analysis of series resistance for CMOS scaling into nanometer regime—Part II: Quantitative analysis,” *IEEE Trans. Electron Devices*, vol. 49, pp. 467–472, 2002.

[10]. S. D. Kim, S. Narasimha, K. Rim, “An integrated methodology for accurate extraction of S/D series resistance components in nanoscale MOSFETs,” in *IEDM Tech. Dig.*, 2005, pp. 149–152.

[11]. B. Coss, C. Smith, W. Y. Loh, P. Majhi, R. M. Wallace, J. Kim, and R. Jammy, "Contact resistance reduction to FinFET source/drain using novel dielectric dipole schottky barrier height modulation method," *IEEE Electron Device Lett.*, vol. 32, pp. 862–864, 2011.

[12]. T. Isogai, H. Tanaka, A. Teramoto, T. Goto, S. Sugawa, and T. Ohmi, "Advanced method for measuring ultra-low contact resistivity between silicide and silicon based on cross bridge Kelvin resistor," in *Proc. IEEE ICMTS*, 2009, pp. 109–113.

[13]. D. K. Schroder, Semiconductor material and device characterization, 2nd ed., John Wiley &Sons: New York, 1998.

[14]. A. Dixit, K. G. Anil, N. Collaert, M. Goodwin, M. Jurczak, and K. D. Meyer, "Analysis of the parasitic S/D resistance in multiple-gate FETs," *IEEE Trans. Electron Devices*, vol. 52, pp. 1132–1140, 2005.

[15]. S. Gannavaram, N. Pesovic, and C. Ozturk, "Low temperature (800 degrees C) recessed junction selective silicon-germanium source/drain technology for sub-70-nm CMOS," in *IEDM Tech. Dig.*, 2000, pp. 437–440.

[16]. J. Liu and M. C. Ozturk, "Nickel germanosilicide contacts formed on heavily boron doped $Si_{1-x}Ge_x$ source/drain junctions for nanoscale CMOS," *IEEE Trans. Electron Devices*, vol. 52, pp. 1535–1540, 2005.

[17]. H. S. Wong, F. Y. Liu, K. W. Ang, G. S. Samudra, and Y. C. Yeo, "Novel nickel silicide contact technology using selenium segregation for SOI n-FETs with silicon–carbon source/drain stressors," *IEEE Electron Device Lett.*, vol. 29, pp. 841–844, 2008.

[18]. K. Suzuki, T. Tanaka, Y. Tosaka, T. Sugii, and S. Andoh, "Source/drain contact resistance of silicided thin-film SOI MOSFET's," *IEEE Trans. Electron Devices*, vol. 41, pp. 1007–1012, 1994.

[19]. M. Chan, F. Assaderaghi, S. A. Parke, S. S. Yuen, C. Hu, and P. K. Ko, "Recess channel structure for reducing source/drain series resistance in ultra-thin SOI MOSFETs," in *Proc. IEEE Int. SOI Conf.*, 1993, pp. 172–173.

[20]. J. M. Larson and J. P. Snyder, "Overview and status of metal S/D Schottky barrier MOSFET technology," *IEEE Trans. Electron Devices*, vol. 53, pp. 1048–1058, 2006.

[21]. ITRS 2011 update.

[22]. B. L. Sharma, "*Metal-Semiconductor Schottky Barrier Junctions and Their Applications*," New York: Plenum Press, 1984.

[23]. S. M. Sze, "Physics of Semiconductor Devices," 2nd ed. New York: Wiley-Interscience, 1981.

[24]. W. M. Loh, S. E. Swirhun, T. A. Schreyer, R. M. Swanson, and K. C. Saraswat,

"Modeling and measurement of contact resistances," *IEEE Trans. Electron Devices*, vol. ED-34, pp. 512–523, 1987.

[25]. S. J. Proctor, L. W. Linholm, and J. A. Mazer, "Direct measurement of interfacial contact resistance, end contact resistance, and interfacial contact layer uniformity," *IEEE Trans. Electron Devices,* vol. ED-30, pp. 1535–1542, 1983.

[26]. E. G. Woelk, H. Krautle, and H. Beneking, "Measurement of low resistive ohmic contacts on semiconductors," *IEEE Trans. Electron. Devices*, vol. ED-33, pp.19-21, 1986.

[27]. G. K. Reeves and H. B. Harrison, "Obtaining the specific contact resistance from transmission line model measurements," *IEEE Electron Device Lett.*, vol. EDL-3, pp. 111–113, 1982.

[28]. S. J. Proctor and L. W. Linholm, "A direct measurement of interfacial contact resistance," *IEEE Electron Device Lett.*, vol.EDL-3, pp. 294–296, 1982.

[29]. R. L. Gillenwater, M. J. Hafich, and G. Y. Robinson, "The effect of lateral current spreading on the specific contact resistivity in D-resistor Kelvin devices," *IEEE Trans. Electron Devices*, vol. ED-34, pp. 537–543, 1987.

[30]. T. F. Lei, L. Leu, and C. L. Lee, "A vertical Kelvin test structure for measuring the true specific contact resistivity," *IEEE Electron Device Lett.*, vol. EDL-7, pp. 259–261, 1986.

[31]. H. H. Berger, "Models for contact to planar devices," *Solid-State Electron.*, vol. 15, pp. 145–158, 1972.

[32]. J. M. Pimbley, "Dual-level transmission line model for current flow in metal-semiconductor contacts," *IEEE Trans. Electron Devices,* vol. ED-33, pp. 1795–1800, 1986.

[33]. N. Stavitski, M. J. H. van Dal, A. Lauwers, C. Vrancken, A. Y. Kovalign, and R. A. M. Wolters, "Evaluation of transmission line model structures for silicide-to-silicon specific contact resistance extraction," *IEEE Trans. Electron Devices*, vol. 55, pp. 1170–1176, 2008.

[34]. H.-J. Ueng, D. B. Janes, and K. J. Webb, "Error analysis leading to design criteria for transmission line model characterization of ohmic contacts," *IEEE Trans. Electron Devices*, vol. 48, pp. 758–766, 2001.

[35]. A. Scorzoni and U. Lieneweg, "Comparison between analytical models and finite-difference simulations in transmission-line tap resistors and L-type cross-Kelvin resistors," *IEEE Trans. Electron Devices*, vol. 37, pp. 1099–1103, 1990.

[36]. U. Lieneweg and D. J. Hannaman, "New flange correction formula applied to interfacial resistance measurements of ohmic contacts to GaAs," *IEEE Electron Device Lett.*, vol. EDL-8, pp. 202–204, 1987.

[37]. J.-K. Ho, C.-S. Jong, C. C. Chiu, C.-N. Huang, and K.-K. Shih, “Low-resistance ohmic contacts to p-type GaN achieved by the oxidation of Ni/Au films,” *J. Appl. Phys.*, vol. 86, pp. 4491–4497, 1999.

[38]. Deepak and H. Krishna, “Measurement of Small Specific Contact Resistance of Metals with Resistive Semiconductors,” *J. Electron. Mater.*, vol. 36, pp. 598–605, 2007.

[39]. E. F. Chor and J. Lerdworatawee, “Quasi-twodimensional transmission line model (QTD-TLM) for planar ohmic contact studies,” *IEEE Trans. Electron Devices*, vol. 49, pp. 105-111, 2002.

[40]. L. Gutai, “Statistical modeling of transmission line model test structures—Part I: The effect of inhomogeneities on the extracted contact parameters,” *IEEE Trans. Electron Devices*, vol. 37, pp. 2350–2360, 1990.

[41]. L. Gutai, “Statistical modeling of transmission line model test structures—Part II: TLM test structure with four or more terminals: A novel method to characterize nonideal planar contacts in presence of inhomogeneities,” *IEEE Trans. Electron Devices*, vol. 37, pp. 2361–2380, 1990.

[42]. D. L. Meier and D. K. Schroder, “Contact resistance: Its measurement and relative importance to power loss in a solar cell,” *IEEE Trans. Electron Devices*, vol. ED-31, pp. 647–653, 1984.

[43]. T. A. Schreyer and K. C. Saraswat, "A Two-Dimensional Analytical Model of the Cross-Bridge Kelvin Resistor," *IEEE Electron Device Lett.*, vol. 7, pp. 661–663, 1986.

[44]. M. Finetti, A. Scorzoni, and G: Soncini, “Lateral current crowding effects on contact resistance measurements in four terminal resistor test patterns,” *IEEE Electron Device Lett.,* vol. EDL-5, pp. 524–526, 1984.

[45]. A. Scorzoni, M. Finetti, K. Grahn, I. Suni, and P. Cappelletti, “Current crowding and misalignment effects as sources of error in contact resistivity measurements—Part I: Computer simulation of conventional CER and CKR structures,” *IEEE Trans. Electron Devices*, vol. ED-34, pp. 525–531, 1987.

[46]. W. M. Loh, K. Saraswat, and R. W. Dutton, “Analysis and scaling of Kelvin resistors for extraction of specific contact resistivity,” *IEEE Electron Device Lett.*, vol. EDL-6, pp. 105–108, 1985.

[47]. A. S. Holland, G. K. Reeves, M. Bhaskaran, and S. Sriram, “Analytical and finite-element modeling of a cross Kelvin resistor test structure for low specific contact resistivity,” *IEEE Trans. Electron Devices*, vol. 56, pp. 2250–2254, 2009.

[48]. S.-L. Zhang, M. Ostling, H. Norstrom, and T. Arnborg, “On contact resistance measurement using four-terminal Kelvin structures in advanced

double-polysilicon bipolar transistor processes," *IEEE Trans. Electron Devices*, vol. 41, pp. 1414–1420, 1994.

[49]. A. S. Holland, G. K. Reeves, and P. W. Leech, "Universal error corrections for finite semiconductor resistivity in cross-Kelvin resistor test structures," *IEEE Trans. Electron Devices*, vol. 51, pp. 914–919, 2004.

[50]. V. Gudmundsson, P. E. Hellström, and M. Östling, "Error Propagation in Contact Resistivity Extraction Using Cross-Bridge Kelvin Resistors," *IEEE Trans. Electron Devices*, vol. 59, pp. 1585–1591, 2012.

[51]. J. Santander, M. Lozano, and C. Cane, "Accurate extraction of contact resistivity on Kelvin D-resistor structures using universal curves from simulation," *IEEE Trans. Electron Devices*, vol. 40, pp. 944–950, 1993.

[52]. J. Santander, M. Lozano, A. Gotz, C. Cane, and E. Lora-Tamayo, "Universal surfaces for the accurate contact resistivity extraction on Kelvin structures with upper and lower resistive layers," in *Proc. IEEE ICMTS*, 1996, pp. 67–74.

[53]. J. Santander, M. Lozano, A. Collado, M. Ullan, and E. Cabruja, "Accurate contact resistivity extraction on Kelvin structures with upper and lower resistive layers," *IEEE Trans. Electron Devices*, vol. 47, pp. 1431–1439, 2000.

[54]. A.J. Walton, M. Fallon, J.T.M. Stevenson, A. Ross, and R.J Holwill, "A methodology for evaluating the area of contacts to improve the accuracy of contact resistance measurements," in *Proc. IEEE ICMTS*, 1990, pp. 23–28.

[55]. Alexey Y. Kovalgin, Natalie Tiggelman, and Rob A. M. Wolters, "An area-correction model for accurate extraction of low specific contact resistance," *IEEE Trans. Electron Devices*, vol. 59, pp. 426–432, 2012.

[56]. M. Bhaskaran, S. Sriram, and A. S. Holland, "Accurate estimation of low (< 10−8 Ω · cm2) values of specific contact resistivity," *IEEE Electron Device Lett.*, vol. 29, pp. 259–261, 2008.

[57]. N. Stavitski, J. H. Klootwijk, H. W. van Zeijl, A. Y. Kovalgin, and R. A. M. Wolters, "A study of cross-bridge Kelvin resistor structures for reliable measurements of low contact resistances," in *Proc. IEEE ICMTS*, 2008, pp. 199–204.

[58]. K. Ohuchi, N. Kusunoki, and F. Matsuoka, "Accurate Measurement of Silicide Specific Contact Resistivity by Cross Bridge Kelvin Resistor for 28nm Complementary Metal–Oxide–Semiconductor Technology and Beyond," *Jpn. J. Appl. Phys.*, vol. 50, pp. 04DA03–04DA03-6, 2011.

[59]. K. Ohuchi, C. Lavoie, C. Murray, C. D'Emic, I. Lauer, J. O. Chu, B. Yang, P. Besser, L. Gignac, J. Bruley, G. U. Singco, F. Pagette, A. W. Topol, M. J. Rooks, J. J. Bucchignano, V. Narayanan, M. Khare, M. Takayanagi, K. Ishimaru, D.-G. Park, G. Shahidi, and P. Solomon, "Extendability of NiPt silicide contacts for

CMOS technology demonstrated to the 22-nm node," in *IEDM Tech. Dig.*, 2007, pp. 1029–1031.

[60]. H.-N. Lin, W.-W. Hsu, W.-C. Lee, and C. H. Wann, "Ultimate Contact Resistance Scaling Enabled by an Accurate Contact Resistivity Extraction Methodology for Sub-20 nm Node," in *IEEE Symp. on VLSI Tech.*, 2009, pp. 102–103.

[61]. N. Stavitski, M. J. H. van Dal, R. A. M. Wolters, A. Y. Kovalgin, and J. Schmitz, "Specific contact resistance measurements of metal–semiconductor junctions," in *Proc. IEEE ICMTS*, Austin, TX, 2006, pp. 13–17.

[62]. T. A. Shankoff, T. T. Sheng, S. E. Haszko, R. B. Marcus and T. E. Smith, "Bird's beak configuration and elimination of gate oxide thinning produced during selective oxidation," *J. Electrochem. Soc.*, vol. 127, pp. 2468–2471, 1980.

[63]. C. P. Chang et al., "A highly manufacturable corner rounding solution for 0.18 μm shallow trench isolation" in *IEDM Tech. Dig.*, 1997, pp. 661–664.

[64]. A. Lauwers, M. de Potter, O. Chamirian, R. Lindsay, C. Demeurisse, C. Vrancken, and K. Maex, "Silicides for the 100-nm node and beyond: Co-silicide, Co(Ni)-silicide and Ni-silicide," *Microelectron. Eng.*, vol. 64, pp. 131–142, 2002.

[65]. A. Lauwers, J. A. Kittl, M. J. H. Van Dal, O. Chamirian, M. A. Pawlak, M. de Potter, R. Lindsay, T. Rayrnakers, X. Pages, B. Mebarki, T. Mandrekar, and K. Maex, "Ni based silicides for 45 nm CMOS and beyond," *Mater. Sci. Eng., B, Solid*, vol. 114/115, pp. 29–41, 2004.

[66]. B.-Y. Tsui and M.-C. Chen, "Series resistance of self-aligned silicided source/drain structure," *IEEE Trans. Electron Devices*, vol. 40, pp. 197–206, 1993.

[67]. S.-D. Kim, "Optimum location of silicide/Si interface in ultra-thin body SOI MOSFETs with recessed and elevated silicide source/drain contact structure," *Solid-State Electron.*, vol. 53, pp. 1112-1115, 2009.

[68]. L. T. Su, M. J. Sherony, H. Hu, J. E. Chung, and D. A. Antoniadis, "Optimization of series resistance in sub-0.2 μm SOI MOSFETs," in *IEDM Tech. Dig.*, 1993, pp. 723–726.

[69]. G. R. Grimmett and D. R. Stirzaker, "Probability and Random Processes," 2nd ed. Clarendon Press, Oxford, 1992.

[70]. Y. L. Chang, Y. W. Chen, Y. C. Chen, K. Shieh, C. Huang, and S. F. Tzou "Chemical and plasma oxidation behaviors of NiSi and NiPtSi silicide films in 65 nm node CMOS process," in *Proc. Int. Interconnect Technol. Conf.*, 2007, pp. 99–101.

[71]. D. Mangelinck, K. Hoummada, A. Portavoce, C. Perrin, R. Daineche, M.

Descoins, D. J. Larson, and P. H. Clifton, "Three-dimensional composition mapping of NiSi phase distribution and Pt diffusion via grain boundaries in Ni_2Si," *Scr. Mater.*, vol. 62, pp. 568–571, 2010.

[72]. J. Demeulemeester, D. Smeets, C. M. Comrie, C. Van Bockstael, W. Knaepen, C. Detavernier, K. Temst, and A. Vantomme, "The influence of Pt redistribution on Ni1−xPtxSi growth properties," *J. Appl. Phys.*, vol. 108, pp. 043505–043505-11, 2010.

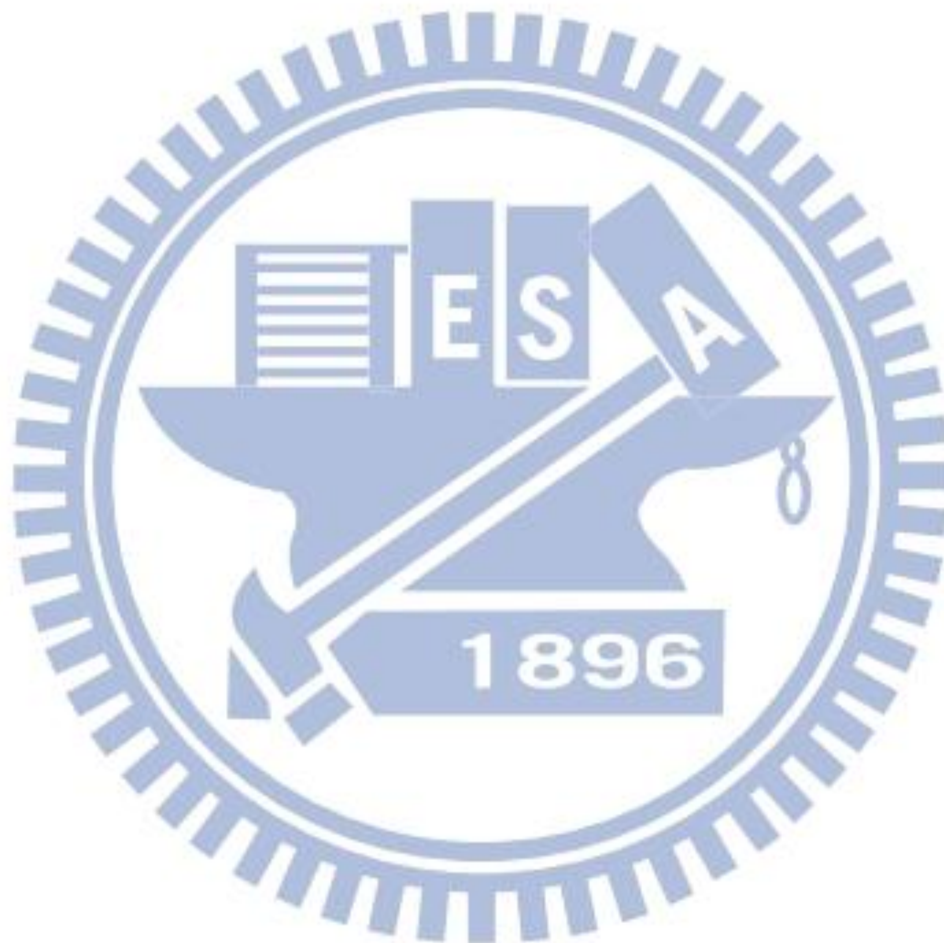

Author's Biography

姓名：曾炫滋

性別：女

生日：民國 77 年 6 月 21 日

學歷：

新竹市立東門國民小學 (83.9-89.6)

新竹市立光華國民中學 (89.9-92.6)

國立新竹女子高級中學 (92.9-95.6)

國立交通大學電子工程學系 (95.9-99.6)

國立交通大學電子研究所碩士 (99.9-101.12)

碩士論文題目：

萃取接觸阻抗係數方法之比較研究——CBKR 結構與改良式 TLM 結構

A Comparison Study of the Specific Contact Resistivity Extraction Methods: CBKR Method and Modified TLM Method